Engineering Materials and Characterization Methods for Mass-produced Plasmonic Devices

A DISSERTATION
SUBMITTED TO THE FACULTY OF THE GRADUATE SCHOOL
OF THE UNIVERSITY OF MINNESOTA
BY

Lauren Mackenzie Otto

IN PARTIAL FULFILLMENT OF THE REQUIREMENTS
FOR THE DEGREE OF
Doctor of Philosophy

Bethanie Joyce Hills Stadler, Adviser

May 2017

Acknowledgements

To say I've had a non-traditional PhD would be an understatement, and many people have helped me get to this moment of completion for which I am forever grateful.

Bethanie Stadler, thank you for coming on board with my work and taking me under your wing. Your support was crucial to the timely completion of my degree. Steve Campbell and Jim Leger, thank you for supporting me when I needed it most, desiring to see me get my PhD in the best way possible, and serving on my committee (thank you also, Vivian Ferry). Doug Ernie, thank you for stepping in last minute for my oral prelim and for helping me figure out the first steps of my transition a couple years ago. And to all my committee members, thank you for your feedback after my two exams.

To David Lilja and Randall Victora, thank you for backing me with the support of the department and beginning my relationship with Beth. Randy, thank you for the conference travel funds from MINT. Both of my trips served to recharge my batteries, reset my clock, and boost my productivity after chaotic seasons as well as gaining vision for the next.

Aeron Hammack, thanks for taking a chance on me and hiring me as your intern three years ago. That summer was a "green pasture" in the middle of a vast desert that extended far beyond graduate school. Thank you for your continued support on the completion of these HGST projects even after our time as "formal colleagues" had ended. Two of these chapters would not have been possible otherwise. Thank you for alerting me to the antenna material problem in HAMR, sharing the plan of using PEALD for titanium nitride, and for connecting me with Adam and Shaul and the Molecular Foundry. Finally, thank you for devoting your personal time and passions to my thesis efforts these last couple years. I agree. I can't believe this actually worked!

O yeah, and thanks again for buying Jack. It was fun to see that car have a second life and actually be a blessing to someone after it was such a curse to me. Long live Samy the Suby!

Adam Schwartzberg and Shaul Aloni, thanks for jumping on board with this crazy plan. I've appreciated your enthusiasm and advisory support and dedication to my user project of non-traditional form. Thank you also for our "what do I want to be when I grow up?" conversation last summer, pointing me to Cyclotron Road, your investment into the process of me getting in, and your entrusting me with Laminera (thanks also, Aeron). I am so grateful, and I am excited to see where this next journey takes me. You each in your own way have mentored me and pushed me to be a better scientist, entrepreneur, and person.

Adam, thank you for your responsiveness at normal and not-so-normal hours when the ALD would surprise me with yet another issue. Troubleshooting that thing taught me a lot that will be pretty useful going forward!

To Aeron, Adam, and Shaul, thanks for coming to Minnesota to celebrate the end of my PhD. It meant a lot to me to have you there. And thanks for the dinners :)

I extend a special thank you to Chris Chen. My PhD would not have been possible without you. Thank you for your support and passing on so much of your knowledge surrounding all the new techniques I was learning and using that the Foundry. You saved me a lot of time and many headaches. Thanks for being the most awesome post doc ever! To Chris and Carissa, thanks for being friends, introducing me to The Butcher's Son and Mr. Dewie's, and letting me crash at your place when my housing fell apart. You made life in Berkeley more livable and fun.

Francesca and Peppe, thanks for being great colleagues, friends, and hosting me at your place when I needed to avoid the really awful commute hours.

Being at a user facility, there are many other Molecular Foundry (and JCAP) staff and researchers who were essential contributors to my work including Frank Ogletree, Tev Kuykendall, Ashley Gaulding, Francesca Toma, Jason Cooper, Anton Zykov, Scott Dhuey, Deirdre Olynick, Paul Ashby, Nick Borys, Jacopo Pedrini, Virginia Altoe, Michael Elowson, Simone Sassolini, Stefano Cabrini, Ed Wong, Ed Barnard, and Nate Hohman. Nick, I love that you actually created the "lunch@lists.lbl.gov" email list for lunchtime. I'm going to miss your laugh at the lunch table.

To my HGST colleagues: Barry Stipe, thank you for bringing me out to HGST for internships not only once but twice, helping us get the papers out, and being one of my references for Cyclotron Road. Randy Simmons, thanks for giving me my negotiated salary :) That made possible my move out to the Bay for finishing my thesis work. Aeron Hammack, Stan Burgos, Shen Ren, Öz Süzer, Matteo Staffaroni, Anika Kinkhabwala, Tom Boone, Seheon Kim, and Andrea Fasoli, thank you for your contributions to my work and your support throughout my internships. To you and all my other colleagues at HGST and WD, working with you was a pleasure and an immensely valuable learning experience.

And I have some friends and colleagues back at UMN to thank as well. Avijit Barik, I am super grateful that we became friends as a result of my COMSOLing for your first DEP project. I would not have made it through year three without you. Thanks for your support. Thank you also to Tim Johnson and Dan Mohr for your friendship and contributions to my earlier works.

Nate Lindquist, thank you for getting me hooked on plasmonics so many years ago, your advising and technical support in my earlier years, and your friendship since. I wish you many more prosperous days in the Bethel Physics Department!

To my house church family, your support and prayers have been vital to my health, healing, and perseverance through my desert. I am so grateful for our community and its impact on my life.

Andrea, Anna, and Kari: you each have been a special and essential part of my journey. Thank you for your continued friendship and mutual discipleship since my move to California. I look forward to more growth and continued conversations. Andrea, thanks for striving to learn about my work and ask meaningful technical questions about what it is I'm up to.

Jes and Nayt, Natalie and Matt: thank you for your friendship and generosity. I have appreciated you hosting me in your homes the five times I've been back to Minnesota for things like my oral prelim, commencement, and defense (as well as other social activities). Natalie, it has been fun to pick up right where we left off this last year :)

Mom and Dad, thank you for supporting me in my education, which has now lasted 23 consecutive school years. I remember a time almost 7 years ago where I contemplated a way to take my bachelor's after three years, go to work, and never think about school

again. Mom, I guess you knew how to push my buttons because you told me not to be a quitter, and I definitely can't be labeled as a quitter. At that time, who would have thought I would stay in school this long?

And I probably owe a thank you to my first grade teacher Mrs. Nordby who likely planted the early seeds of STEM in me and started me off in the advanced math grouping where my mom says I was the only girl. Being outnumbered 10:1 or more is nothing new I guess...

And finally, I thank my Abba Father for his faithfulness to me, the Holy Spirit for being my strength, and Jesus for being the vine for my branches. You dwell at my core and are the absolute center of me. So I will label this dissertation an ebenezer, or my "stone of help" (perhaps more accurately translated as "power" or "strength" rather than "help"). May I never forget your guidance in the desert, the manna you've given me ("what is it?"), and the victories that are possible with you.

Dedication

To everyone I mentioned in the acknowledgements

Abstract

Over the last decade, plasmonic devices have seen considerable attention, and while there has been significant scientific advancement for plasmonic devices in the laboratory, there still are no industrially produced, high-tech devices which incorporate plasmonics on the market. Industry is in need of robust characterization methods for the development of near-field based devices en route to final product manufacturing lines as well as stable plasmonic materials that can easily be integrated into existing complex process flows. In this dissertation, original research that opens up doors for mass-produced plasmonic devices is presented. Engineered characterization methods include the development of a theoretical model for the prediction of scattering scanning near-field optical microscopy behavior of plasmonic devices, the use of this near-field characterization technique together with scanning electron microscopy cathodoluminescence to perform complete and convergent characterization of plasmonic excitation and coupled near-field emission. Engineered materials are centered on plasma-enhanced atomic layer deposited titanium nitride, discovering its chemistry and behavior under a variety of conditions, and demonstrating its fabricability as both two dimensional etched structures and three dimensional coatings of complex shapes.

Contents

Acknowledgements **i**

Dedication **v**

Abstract **vi**

List of Tables **x**

List of Figures **xi**

List of Publications **xiv**

1 Introduction **1**

1.1 Need for Plasmonic Materials and Deposition Techniques 1

1.2 Need for Characterization Techniques 3

1.3 Scope of this Dissertation 4

2 Background Theoretical Considerations **6**

2.1 Maxwell's Equations 6

2.2 The Volume Plasmon 7

2.3 Plasmonic Materials 9

2.3.1 Plasmonic Metals 10

2.3.2 Titanium Nitride 11

2.4 Nanofocusing 12

3 Predicting Scattering Scanning Near-field Optical Microscopy of Mass-produced Plasmonic Devices **15**
3.1 Heat-assisted Magnetic Recording Background 16
3.2 sSNOM Background 17
3.3 Predicting sSNOM behavior of mass-produced plasmonic devices 19
3.3.1 Effects of the AFM Tip's Shape 22
3.3.2 Effects of the AFM Tip's Distance of Closest Approach 24
3.3.3 Final Model Results 26

4 Bidirectional characterization of waveguide-coupled plasmonic antennas by near-field excitation and mapping **29**
4.1 Bidirectional Characterization 30
4.2 Scanning Electron Microscopy Cathodoluminescence 31
4.3 Scattering Scanning Near-field Optical Microscopy 34

5 Plasma-enhanced Atomic Layer Deposition for Plasmonic Titanium Nitride **38**
5.1 Plasma-enhanced Atomic Layer Deposition 39
5.2 *In situ* Spectroscopic Ellipsometry 41
5.3 Auger Electron Spectroscopy 44
5.4 Grating Fabrication and Characterization 47

6 Chemistry of Atomic Layer Deposited Titanium Nitride **49**
6.1 As-deposited Material Properties 50
6.2 Material Properties of Annealed Films 51
6.2.1 Film Thickness and Conductivity 52
6.2.2 Film Plasmonic FOM 53
6.2.3 Film Composition 57

7 Towards Plasmonic and Conductive Photonics in Three Dimensions **60**
7.1 Titanium Nitride Properties 61
7.2 Inverse Opal Fabrication 63
7.3 Photonic Crystal Reflected Intensity 65

7.4 Annealing Effects on Flat Films 66
7.5 Annealing Effects on Photonic Crystals 72

8 Conclusion **77**

References **79**

Appendix A. Experimental Methods **94**
A.1 Predicting sSNOM Methods 94
A.2 Bidirectional Characterization Methods 95
A.3 Plasma-enhanced Atomic Layer Deposition Recipes 95
A.4 Stable Plasma-enhanced Atomic Layer Deposition of Nitrides 97
A.5 Annealing Experimentation 99
A.6 Opal Synthesis 99

Appendix B. Supporting Information **101**
B.1 Predicting sSNOM 101
B.1.1 Additional Mappings for the Parameters Chosen in the Main Text (15 nm radius, 8 nm DCA) 101
B.1.2 Figures for Observing Trends in the Maximums of Each Mapping as a Function of DCA Height, Tip Radius, and Harmonic 105
B.1.3 Near-field Mappings for Other Modeled Tip Radii 106
B.1.4 Near-field Mappings for Other Modeled Distances of Closest Approach 111
B.1.5 Simulated Electric Field Intensity 113
B.2 Bidirectional Characterization 115
B.2.1 SEM-CL 117
B.2.2 sSNOM 121

Appendix C. Common Acronyms **132**
C.1 Acronyms 132

List of Tables

2.1 Material plasmonic properties 12
5.1 Plasma-enhanced atomic layer deposition recipes 41
5.2 Ellipsometry material parameters 42
5.3 Material parameters under different chamber conditions 46
A.1 Plasma-enhanced atomic layer deposition recipes 96
C.1 Acronyms 132

List of Figures

1.1 Synthetic metals 2
2.1 Dielectric function of plasmonic metals 11
2.2 Nanofocusing 14
3.1 Schematic for sSNOM measurements for HAMR 17
3.2 sSNOM experimental output 19
3.3 sSNOM model theory 20
3.4 TEM images of AFM tips 22
3.5 Tip radius effects 23
3.6 Distance of closest approach effects 24
3.7 Maximum Intensity vs. DCA and Harmonic 25
3.8 Result of sSNOM model compared to measurements 27
4.1 Schematics for bidirectional near-field characterization 31
4.2 CL analysis as performed inside a scanning electron microscope 33
4.3 sSNOM images of HAMR heads as a function of wavelength and polarization 36
5.1 Plasma-enhanced atomic layer deposition 40
5.2 Fitting methods for spectroscopic ellipsometry 43
5.3 Thickness dependence of optical properties 44
5.4 Effects of deposition chamber condition 45
5.5 Fabrication of titanium nitride gratings 48
6.1 Thickness and grain size of as-deposited titanium nitride 50
6.2 Dielectric function for as-deposited titanium nitride 51
6.3 Thickness and conductivity of annealed titanium nitride 52
6.4 Carrier concentration of annealed titanium nitride 53

6.5 Figure of merit after anneals 54
6.6 Oscillator fit parameters vs. anneal temperature 55
6.7 Figure of merit and plasmonic transition wavelength of annealed titanium nitride 56
6.8 Figure of merit after anneals 57
6.9 Auger electron spectroscopy of annealed titanium nitride 58
7.1 Dielectric function and conductivity of titanium nitride films for inverse opals 62
7.2 Inverse opal fabrication 64
7.3 Inverse opal reflected intensity 66
7.4 Thickness change vs. anneal temperature 67
7.5 Figures of merit vs. anneal temperature 68
7.6 Oscillator fit parameters vs. anneal temperature 69
7.7 Plasmonic properties vs. anneal temperature 70
7.8 Carrier concentration and ellipsometry fit 72
7.9 Photonic crystal resonance shifts 74
7.10 Photonic crystal resonance position vs. anneal temperature 75
7.11 Photonic crystal resonance position vs. angle 76
A.1 Inside the PEALD chamber 98
B.1 Complete harmonics for Figure 3.6 101
B.2 Maximum intensity decay with DCA and harmonic 105
B.3 Maximum intensities vs. tip radius 106
B.4 Harmonics for a 20 nm tip radius 106
B.5 Harmonics for a 10 nm tip radius 108
B.6 Harmonics for a 10 nm tip radius and 16 nm DCA 109
B.7 Harmonics for a 10 nm tip radius 110
B.8 Harmonics for a 4 nm DCA 111
B.9 Harmonics for a 12 nm DCA 112
B.10 Simulated electric field intensity of a HAMR head 113
B.11 Maximum electric field intensities 114
B.12 Maximum electric field intensities 115
B.13 Schematics comparing hard disk drive write head profiles 116

B.14 HAMR head on a fiber for SEM-CL 117
B.15 Mounting schematic for SEM-CL experiments 118
B.16 Detection schematic of the SEM-CL signal 119
B.17 Complete set of recorded SEM-CL mappings 120
B.18 Schematic of HAMR heads as imaged by sSNOM 121
B.19 Complete harmonics for 830 nm illumination 121
B.20 Maximum intensities of all 830 nm near-field maps 125
B.21 Maximum intensities vs. harmonic for 830 nm 126
B.22 Complete harmonics for 633 nm illumination 126
B.23 Maximum intensities of all 633 nm near-field maps 130
B.24 Maximum intensities vs. harmonic for 633 nm 131

List of Publications

The original research presented in this dissertation was selected from Lauren's following in preparation and published works:

1. **L. M. Otto**, E. A. Gaulding, T. Kuykendall, C. T. Chen, A. Zykov, A. T. Hammack, F. M. Toma, D. F. Ogletree, S. Aloni, B. J. H. Stadler, and A. M. Schwartzberg. Towards three-dimensional titanium nitride plasmonics, In preparation.

2. **L. M. Otto**, C. T. Chen, T. Kuykendall, A. T. Hammack, D. F. Ogletree, S. Aloni, B. J. H. Stadler, and A. M. Schwartzberg. Materials chemistry of atomic layer deposited titanium nitride, In preparation.

3. A. T. Hammack, D. Nowak, **L. M. Otto**, W. Morrison, B. C. Stipe, and S. Park. Simultaneous multimethod near-field characterization of magnetoplasmonic systems, In preparation.

4. **L. M. Otto**, D. F. Ogletree, S. Aloni, M. Staffaroni, B. C. Stipe, and A. T. Hammack. Bidirectional characterization of waveguide-coupled plasmonic antennas by near-field excitation and mapping, In preparation.

5. **L. M. Otto**, S. P. Burgos, M. Staffaroni, S. Ren, Ö. Süzer, B. C. Stipe, P. D. Ashby, and A. T. Hammack. Predicting scattering scanning near-field optics microscopy of mass-produced plasmonic devices, Under review.

6. **L. M. Otto**, A. T. Hammack, S. Aloni, D. F. Ogletree, D. L. Olynick, S. Dhuey, B. J. H. Stadler, and A. M. Schwartzberg. Plasma-enhanced atomic layer deposition for plasmonic TiN, *Proceedings of the SPIE* **9919**, 99190N-1 (2016).

7. S. Kumar, T. W. Johnson, C. K. Wood, T. Qu, N. J. Whittenberg, **L. M. Otto**, J. Shaver, N. J. Long, R. H. Victora, J. B. Edel, and S.-H. Oh. Template-stripped multifunctional wedge and pyramid arrays for magnetic nanofocusing and optical sensing, *ACS Applied Materials and Interfaces* **8**, 9319-9326 (2016).

8. K. J. Freedman, **L. M. Otto**, A. P. Ivanov, A. Barik, S.-H. Oh, and J. B. Edel. Nanopore sensing at ultra-low concentrations using single molecule dielectrophoretic sensing, *Nature Communications* **7**, 10217 (2016).

9. **L. M. Otto**, D. A. Mohr, T. W. Johnson, S.-H. Oh, and N. C. Lindquist. Polarization interferometry for real-time spectroscopic plasmonic sensing, *Nanoscale* **7**, 4226-4233 (2015).

10. J. Jose, S. Kress, A. Barik, **L. M. Otto**, J. Shaver, T. W. Johnson, Z. J. Lapin, P. Bharadwaj, L. Novotny, and S.-H. Oh. Individual template-stripped conductive gold pyramids for tip-enhanced dielectrophoresis, *ACS Photonics* **1**, 464-470 (2014).

11. A. Barik, **L. M. Otto**, D. Yoo, J. Jose, T. W. Johnson, and S.-H. Oh. Dielectrophoresis-enhanced plasmonic sensing with gold nanohole arrays, *Nano Letters* **14**, 2006-2012 (2014).

12. T. Noda, **L. M. Otto**, M. Elborg, M. Jo, T. Mano, T. Kawazu, L. Han, and H. Sakaki. GaAs/AlGaAs quantum wells with indirect-gap AlGaAs barriers for solar cell applications, *Applied Physics Letters* **104**, 122102 (2014).

13. N. C. Lindquist, T. W. Johnson, J. Jose, **L. M. Otto**, and S.-H. Oh. Ultrasmooth metallic films with buried nanostructures for backside reflection-mode plasmonic biosensing, *Annalen der Physik (Berlin)* **524**:11, 687-696 (2012).

Chapter 1

Introduction

The term "Plasmonics" was coined as a term analogous to electronics and photonics after the realization of early researchers that surface plasmons were capable of enabling a new realm of devices, similar to electrons and photons previously.[1,2] Surface plasmons are electron density waves bound to the interface of a metal (or metal-like material) and a dielectric, and they are induced by incoming resonant photons. Surface plasmons are responsible for strong high-gradient electric fields that are particularly sensitive to their surroundings. As a result, plasmonic devices have been engineered as circuits and inter-device communications,[3,4] precision light sources,[5,6] biological and chemical sensing and imaging,[7–9] photovoltaics,[10,11] and high density data storage.[12,13] To date, much of what plasmonics researchers have achieved has remained in scientific laboratories rather fulfilling the early expectations of the commercial devices with roadblocks primarily relating to materials and also to scalable deposition and characterization techniques.[3,14] One pregnancy test remains the only mass-produced plasmonic device available on the market today,[15] with the hard disk drive industry still hoping to soon release its much anticipated heat-assisted magnetic recording (HAMR) technology.

1.1 Need for Plasmonic Materials and Deposition Techniques

Today's frontier device technologies are dependent on high conductivity materials (usually elemental or alloyed metals), which suffer from thermal, chemical, or structural

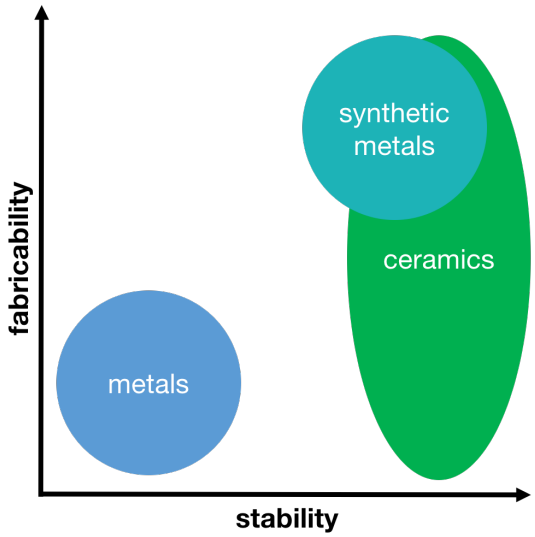

Figure 1.1: **Materials concept.** Synthetic metals offer the stability and fabricability of ceramics that elemental or alloyed metals cannot offer.

instabilities and are difficult to pattern or deposit uniformly at technologically relevant thicknesses and morphologies (below ∼10-20 nm and on three-dimensional shapes). These limitations are especially relevant for plasmonic devices, which are dependent on metals such as silver or gold.[9,14] Synthetic metals are ceramic materials having conductivity comparable to metals with increased stability and improved fabricability (Figure 1.1), where fabricability is a qualitative term describing the degree to which a material can be deposited and patterned as desired with suitable techniques. Titanium nitride has shown the most promise and seen the most attention as a possible replacement material in plasmonic devices designed for the visible and near infrared optical frequencies.

HAMR is widely seen as a solution to significantly increase storage density. However, thermal instability of a nanoscale gold plasmonic antenna is hampering the development of this technology.[16] The high temperatures required for HAMR cause diffusion in the nanostructured gold antenna, which results in morphological changes rendering the structure incapable of performing its function. Synthetic metals are an alternative providing the necessary structural stability while still preserving plasmonic material

properties. While titanium nitride has been suggested as a suitable solution, well-established deposition techniques still pose many problems.

Industry is familiar with synthetic metals such as titanium nitride, which has long been used as an adhesion layer and diffusion barrier in the complementary metal-oxide-semiconductor (CMOS) industry.[17] Titanium nitride is fabricated with chemical vapor deposition (CVD) based techniques in which reactants are present concurrently and therefore do not allow for precise thickness control, film conformality, or low surface roughness.[18] Recent development of synthetic metals has largely occurred within the plasmonics research community where high quality films have been deposited with sputtering.[19] Both of these techniques often require temperatures in excess of 700°C, and sputtering requires crystalline lattice-matched substrates due to directional, epitaxial material growth.[17,19] While the results are compelling, such requirements are unattainable for large scale applications in which complicated lithography processes are performed on inhomogeneous substrates. New CMOS and HAMR technologies require fabrication below 400°C and 200°C, respectively, due to thermal limitations of previously deposited materials.[20] Plasma enhanced atomic layer deposition (PEALD) is the only technique capable of depositing ultrathin conformal synthetic metals at low temperatures with relatively substrate independent properties.[21] In addition, the thermal conductivity of titanium nitride and other synthetic metals is too low to serve as a complete replacement for gold in a HAMR hard drive. Instead, utilizing PEALD synthetic metals allows the conformal coating of single (or few) nanometer "candy-coatings" of the plasmonic metal in order to offer both the desired stability and the necessary thermal conductivity of a scaled-up plasmonic nanoantenna.

1.2 Need for Characterization Techniques

In the recent decade, near-field characterization techniques have seen significant progress and are capable of probing plasmonic antenna resonant fields with nanometer scale resolution.[22–24] These near-field measurement techniques are advantageous to the development of HAMR heads and can realize their full potential in combination with one another. Bidirectional characterization of a prototype plasmonic antenna integrated

into a heat assisted magnetic recording write head can be performed by both local excitation (cathodoluminescence) using the focused electron beam of a scanning electron microscope with far-field collection as well as by local mapping of the optical near-field using scattering scanning near-field optical microscopy. Heat assisted magnetic recording technology is the current best candidate for increasing magnetic information storage density,[12,13] and the presented bidirectional characterization of the performance of fully integrated waveguide coupled plasmonic devices enables crucial metrological comparisons of as-fabricated device performance to as-modeled device expectations.

Scattering scanning near-field optical microscopy (sSNOM) enables optical imaging and characterization of plasmonic devices with nanometer-scale resolution well below the diffraction limit.[24,25] This technique enables developers to probe and understand the waveguide-coupled plasmonic antenna in as-fabricated HAMR heads. In order validate and predict results and to extract information from experimental measurements that is physically comparable to simulations, a model was developed to translate the simulated electric field into expected near-field measurements using physical parameters specific to sSNOM physics. The methods used prove that sSNOM can be used to determine critical sub-diffraction-limited dimensions of optical field confinement, which is a crucial metrology requirement for the future of nano-optics, semiconductor photonic devices, and biological sensing where the near-field character of light is fundamental to device operation.

1.3 Scope of this Dissertation

This dissertation covers original research aimed at bridging the gap between the scientific advancement of plasmonics and plasmonic devices with the needs of industry in order to successfully manufacture scaled-up and durable plasmonic devices. Through the engineering of new synthetic metal-based plasmonic materials as well as the development of characterization techniques, the possibility of developing mass-produced plasmonic devices can be realized.

While this section introduces the general topic of this dissertation, each chapter has its own self-contained and more specific introduction.

- Chapter 2 presents the electromagnetic theory behind plasmonics, plasmonic materials, and the diffraction limit.
- Chapter 3 describes a technique for predicting scattering scanning near-field optical microscopy behavior of mass-produced plasmonic devices.
- Chapter 4 demonstrates the value in bidirectional near-field characterization of waveguide-coupled plasmonic devices.
- Chapter 5 explains plasma-enhanced atomic layer deposition and basic characterization of plasmonic titanium nitride.
- Chapter 6 describes the materials chemistry of atomic layer deposited titanium nitride as revealed by experimental annealing.
- Chapter 7 demonstrates three dimensional conductive, photonic, and plasmonic inverse opals made with atomic layer deposited titanium nitride.
- Chapter 8 shares a final discussion of the presented work in the dissertation with direction for the future.

Chapter 2

Background Theoretical Considerations

As background for the understanding of plasmonics (materials, antennas, HAMR), spectroscopic ellipsometry, and near-field characterization techniques, the relevant electromagnetic physics is outlined as well as a discussion on the diffraction limit of light in optical imaging.

2.1 Maxwell's Equations

Electromagnetic theory can be outline with a set of four equations commonly known as Maxwell's Equations. When no free charges or free currents are present, these equations can be written:[26–28]

$$\begin{aligned} \nabla \cdot \mathbf{D} &= 0 \\ \nabla \cdot \mathbf{B} &= 0 \\ \nabla \times \mathbf{E} &= -\frac{\partial \mathbf{B}}{\partial t} \\ \nabla \times \mathbf{H} &= \frac{\partial \mathbf{D}}{\partial t} \end{aligned} \tag{2.1}$$

where $\mathbf{D}$ is the dielectric displacement, $\mathbf{B}$ is the magnetic flux density or magnetic induction, $\mathbf{E}$ is the electric field, and $\mathbf{H}$ is the magnetic field. Furthermore, when considering the properties of materials interacting with electric fields $\mathbf{E}$ and limiting

ourselves to linear and isotropic media, we can define a polarization $\mathbf{P}$ such that:

$$\mathbf{P} = \epsilon_0 \chi_e \mathbf{E} \tag{2.2}$$

where ϵ_0 is the permittivity of vacuum ($\epsilon_0 = 8,85 \times 10^{-12}$ F/m), and in this case, χ_e is the electric susceptibility. The polarization $\mathbf{P}$ is the per unit volume electric dipole moment inside the material and can be related to the dielectric displacement through:

$$\mathbf{D} = \epsilon_0 \mathbf{E} + \mathbf{P} = \epsilon_0 \epsilon_r \mathbf{E} = \epsilon_0 (1 + \chi_e) \mathbf{E} \tag{2.3}$$

where ϵ_r is the relative permittivity or dielectric constant of the material. In reality, materials are dispersive and so the dielectric constant becomes a frequency ω dependent function: $\epsilon_r(\omega)$.

2.2 The Volume Plasmon

Simply stated, plasmons are light-induced electron oscillations. Describing the nature of these oscillating electrons, like a free electron gas, can be done using mechanical equations for a harmonic oscillator that is both driven and damped. The force $\mathbf{F}$ due to the oscillating electron can be stated as:

$$\mathbf{F} = -e\mathbf{E} = m\ddot{\mathbf{x}} + m\gamma\dot{\mathbf{x}} \tag{2.4}$$

where m is the electron mass, e is the electron charge, and γ is the oscillation damping coefficient caused by the material (on the order of 100 THz). Since light is an electromagnetic wave and assuming harmonic time dependence, we can describe the driving electric field $\mathbf{E}$ through the equation:

$$\mathbf{E}(t) = \mathbf{E}_0 e^{-i\omega t} \tag{2.5}$$

Therefore, a particular solution to this differential equation for the position vector $\mathbf{x}$ describing the electron motion would be: $\mathbf{x}(t) = \mathbf{x}_0 e^{-i\omega t}$. Solving for $\mathbf{x}_0$ leads to:

$$\mathbf{x}_0 = \frac{e}{m(\omega^2 + i\gamma\omega)} \mathbf{E}_0 \tag{2.6}$$

and $\mathbf{x}(t)$ can be directly substituted into the macroscopic polarization $\mathbf{P} = -n_e e\mathbf{x}$ (n_e is the number of electrons) to yield:

$$\mathbf{P} = -\frac{n_e e^2}{m(\omega^2 + i\gamma\omega)}\mathbf{E} \tag{2.7}$$

Substitution of Equation 2.7 into Equation 2.3 yields:

$$\mathbf{D} = \epsilon_0(1 - \frac{\omega_p^2}{\omega^2 + i\gamma\omega})\mathbf{E} \tag{2.8}$$

where $\omega_p = \sqrt{\frac{n_e e^2}{\epsilon_0 m}}$ is the plasma frequency of the free electron gas, which usually occurs in the ultraviolet frequency range for materials relevant to this dissertation. The resulting complex dielectric function is described by:

$$\epsilon_r(\omega) = 1 - \frac{\omega_p^2}{\omega^2 + i\gamma\omega} \tag{2.9}$$

Description of a dielectric function by Equation 2.9 is known as the Drude Model;[28–30] however, the Drude Model cannot adequately describe plasmonic materials such as gold, silver, or titanium nitride for optical frequencies due to nearby (in frequency) interband transitions. Therefore, a more complex oscillator model capable of accounting for a given material resonant frequency (ω_0) must be used:

$$\mathbf{F} = -e\mathbf{E} = m\ddot{\mathbf{x}} + m\gamma\dot{\mathbf{x}} + m\omega_0^2\mathbf{x} \tag{2.10}$$

which yields a complex dielectric function of:

$$\epsilon_r(\omega) = 1 - \frac{\omega_p^2}{\omega^2 + i\gamma\omega - \omega_0^2} \tag{2.11}$$

and is known as the Drude-Lorentz model.

For the high frequency limit ($\omega \gg \omega_p$) in the free electron Drude model, $\epsilon \to 1$, which does not accurately account for the high-frequency behavior of common plasmonic materials due to high residual polarization effects. Therefore, the "1" in Equations 2.9 and 2.11 should be replaced with the term ϵ_∞, which is the high-frequency dielectric constant of the material and is usually ($1 \leq \epsilon_\infty \leq 10$).[28] The Drude-Lorentz model

modified to include ϵ_∞ (Equation 5.1) was used to describe the spectroscopic ellipsometry data from the atomic layer deposited titanium nitride material in this dissertation Chapter 5.2.[31–39]

2.3 Plasmonic Materials

Surface plasmons exist at the interface of a conductive material and a dielectric. The following theory has been included for the purpose of better understanding their nature and the required properties of the conductive material in order to generate and sustain propagating surface plasmons. Beginning again with the driving force as an electromagnetic wave, we redefine Equation 2.5 to include propagation in space:

$$\mathbf{E}(\mathbf{x}, t) = \mathbf{E}_0 e^{i\mathbf{k}\cdot\mathbf{x}} e^{-i\omega t} \tag{2.12}$$

where $\mathbf{k}$ is the propagation constant in three dimensions and can be defined as $\mathbf{k} = k_x\hat{\mathbf{x}} + k_y\hat{\mathbf{y}} + k_z\hat{\mathbf{z}}$. In the case of an xy interface-bound surface plasmon wave generated by a transverse magnetic wave (magnetic field along y direction) traveling in the x direction, k_x is the plasmon propagation constant, $k_y = 0$, and k_z is imaginary as the electric field evanescently decays away from the interface (moving in the positive and negative z direction). For this case and under appropriate boundary conditions, it can be seen that:[28]

$$\begin{aligned} \frac{k_{d,z}}{k_{m,z}} &= -\frac{\epsilon_d}{\epsilon_m} \\ k_{d,x} &= k_{m,x} \end{aligned} \tag{2.13}$$

where d and m are for the dielectric and metal (or conductive metal-like) materials, respectively. For the described condition, general statements about the two dielectric functions can be stated: $\epsilon_d > 0$ and is real, $\epsilon_m = \epsilon_m' + i\epsilon_m''$, and $|\epsilon_m'| > 0$. Therefore, a material exhibiting plasmonic properties can be defined by its dielectric function, which should be complex, and the real part should be negative. A material capable of strongly generating electron oscillations (ϵ_m' is negative and large) without these oscillations being strongly damped or material losses being too severe (ϵ_m'' is small). The quality or strength of the plasmonic properties of a material can be described by a

figure of merit (FOM):

$$FOM = -\frac{\epsilon'_m}{\epsilon''_m} \tag{2.14}$$

which will be discussed further in this section as well as Chapters 5.2, 6, and 7. Another important parameter for plasmonic properties is the wavelength at which the material becomes plasmonic (ϵ'_m becomes negative). This parameter is referred to as the plasmon wavelength λ_p. It is worth noting that λ_p is not directly related to the bulk plasmon frequency ω_p.

2.3.1 Plasmonic Metals

Common plasmonic metals include gold, silver, copper, and aluminum (Figure 2.1).[9] While the real part of aluminum's dielectric function is negative and very large, its imaginary part is also rather large and prevents it from supporting plasmons well for visible frequencies and applications; however, aluminum is an advantageous plasmonic material for applications in the ultraviolet, which includes direct enhancement of biological fluorescence signatures.[40,41] Of all the plasmonic materials, silver has the highest FOM for the visible and near infrared frequencies; however, silver is also well known for oxidizing (an issue for aluminum and copper, too) and sulfidizing, rendering it incapable sustaining plasmonic performance over the long term for applications involving open air, chemical, or biological environments.[9] For this reason, gold has been the standard for plasmonic devices operating in the visible. In addition, nanostructured metal materials are known to be thermally and mechanically unstable and are creating significant challenges for the HDD industry, which is using a plasmonic antenna as a heater.[16,42] These problems have triggered academics and industry personel alike to research alternative plasmonic materials, which include metal alloys, transparent conducting oxides, and transition metal nitrides (synthetic metals).[9,14,16,43–46] For applications in the visible and near infrared, synthetic metals such as titanium nitride have been recognized to have the most promise for the realization of stable plasmonic devices.[46]

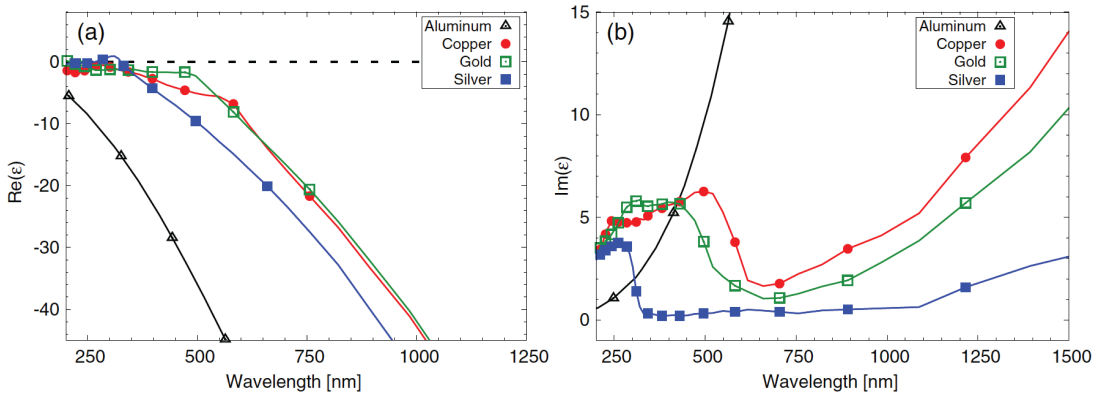

Figure 2.1: **Dielectric function of plasmonic metals.**[9] Aluminum is advantageous for applications in the ultraviolet, but cannot strongly support plasmons in the visible and near infrared. In contrast, gold and silver have strong plasmonic properties in the visible and near infrared, with gold used more often for applications due to its chemical stability.

2.3.2 Titanium Nitride

Of the possible plasmonic synthetic metals, titanium nitride has seen the most attention, although most work has relied on deposition techniques that are industry incompatible[19,47–53] or employ the plasmonic synthetic metal as a bulk material.[54] Unfortunately, for many plasmonic applications (or desired wavelengths), including the scale-up of technologies like HAMR, the bulk plasmonic synthetic metals do not exhibit high enough FOMs (or thermal conductivities) to provide the necessary resonant enhancements or coupling efficiencies.[54,55] For instance, plasmonic metals such as gold and silver (λ_p <300 nm and 350 nm, respectively) have FOMs at 830 nm (the HAMR operation wavelength) ∼13 and ≥50, respectively.[9,56] In contrast, the highest FOM titanium nitride film (of unknown but presumably large thickness, i.e. optically thick at ≳100 nm) reported exhibited λ_p ∼460-470 nm and FOM at 830 nm ∼4.6.[47] This information is also presented in Table 2.1.

Material	λ_p **(nm)**	**FOM @ 830 nm**
gold	<300	∼13
silver	<350	≥50
titanium nitride	460-470	4.6

Table 2.1: **Material plasmonic properties.** Gold and silver are strong plasmonic materials in the visible and near-infrared[9,56] whereas the best titanium exhibits significantly lower, although still useful plasmonic properties.[47]

Instead, applying an ultrathin (<10 nm, but more like 2-5 nm) coating of titanium nitride or other synthetic metal as a conformal coating around a metallic plasmonic structure offers the desired thermal,[57] chemical, and mechanical[58–60] protection without giving up the necessary plasmonic and thermal properties. In general, because plasmonic devices operate using evanescent waves that decay exponentially away from their surfaces, maintaining the plasmonic surface properties is essential. For instance, applications such as HAMR and surface enhanced Raman spectroscopy both require operation at distances ∼3 nm from the surface.[61] While coating plasmonic materials in traditional oxides (i.e. silica, alumina, titania, etc.) may provide additional stability, significant advantages to device operation are gained when the coating material also exhibits plasmonic properties.

2.4 Nanofocusing

The diffraction limit:[62]

$$d = \frac{\lambda}{2nsin(\theta)} \tag{2.15}$$

was first defined by Abbe as the maximum resolution possible for a microscope using light of wavelength λ propagating through a medium with refractive index n and collected by an objective with an opening angle θ. Effectively, using traditional optics or imaging methods, it is not possible to confine light or gather an image with resolution better than $\sim \lambda/2$. However, using evanescent waves and surface plasmons, it becomes possible to confine an electromagnetic field in a region smaller than what is traditionally

allowed by the diffraction limit. Both metal-insulator-metal (MIM) and insulator-metal-insulator (IMI) waveguides have been shown to demonstrate surface plasmons confined at the surface.[28,63]

The condition that is the most intriguing and relevant to this dissertation is the case of a plasmonic antenna designed as a tapered IMI waveguide. In this case, generated surface plasmons propagate toward the tip or pointed end of the tapered waveguide. Depending on the polarization of the driving electromagnetic wave, both asymmetric and symmetric waveguide modes are possible (Figure 2.2). For light polarized perpendicular to the waveguide propagation direction, an asymmetric mode (where the free electron density oscillations are asymmetric) is created, which propagates down the tapered waveguide, and as the metal thickness $\rightarrow 0$, the propagating plasmon converts back into free space propagating light. In contrast, when the driving electromagnetic wave is polarized along the waveguide propagation direction, the free electron density oscillations are symmetric and their propagation towards the waveguide end results in a high field concentration that is evanescent in nature (and therefore unable to propagate into the far-field). In fact, for an infinitesimally small tip point, the propagating plasmons approach the end logarithmically and the field diverges to infinity.[64] This effect is known as "nanofocusing" or the "lightning rod effect."[64,65]

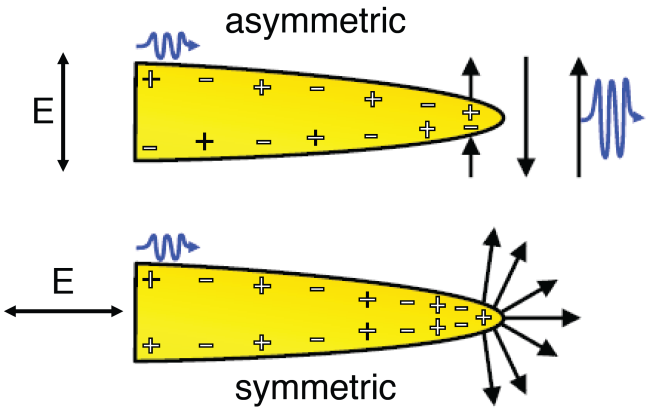

Figure 2.2: **Nanofocusing.** An electric field polarized perpendicular to the antenna shaft exhibits charge asymmetry in the metallic region and a propagating plane wave is reemitted. In contrast, for an electric field polarized along the shaft of the antenna, there is charge symmetry. As the antenna narrows to a point, the charge density becomes large, and the field is "nanofocused" resulting in a high field gradient at the point, which radiates in the forward direction as an evanescent wave.

Using nanofocusing, visible or near infrared wavelength light can be confined to a spot size of 10s of nanometers. The gold plasmonic antenna used in HAMR utilizes this phenomenon in order to confine 830 nm laser light into a ∼30-50 nm high intensity and high gradient evanescent field that is responsible for heating the magnetic media and enabling the (magnetic) polarization change required for data storage.

Chapter 3

Predicting Scattering Scanning Near-field Optical Microscopy of Mass-produced Plasmonic Devices

Todays optic, photonic, and plasmonic devices incorporate light into nanoscale devices that enable diverse new functionality for chemical or biological sensing and imaging,[7] precision light sources,[6,66,67] silicon photonics-based communications and signal processing,[68] and data storage.[12,13] These devices are often critically dependent on the behavior of light well below the diffraction limit, and therefore require robust near-field characterization techniques, linked with numerical predictions and validations, to design and fabricate functioning devices. This requirement becomes even more essential when such devices are to be manufactured in massive quantities that require process quality control. In fact, future hard disk drives (HDDs) will rely on near-field optical heaters for data storage, and the successful development and production of novel HDD magneto-optical write heads is largely contingent on the ability to reliably predict and validate the near-field behavior of as fabricated devices by direct experimental characterization. The technical improvements to scattering scanning near-field optical microscopy that we have developed for HDD write head optical antenna characterization are potentially

extensible and beneficial to any field of study involving the direct optical measurement of photonic modes arising in proximity to nanoscale features.

3.1 Heat-assisted Magnetic Recording Background

Despite alternative technology developments, most of the world's increasing data storage demands are still satisfied by HDDs. To improve efficiency, the HDD industry has encountered and worked to overcome fundamental limitations preventing the further areal density growth on a disk of magnetic material.[12,13,42,69,70] Currently used magnetic media cannot support smaller bit sizes (known as the superparamagnetic limit, smaller bits are less stable), but magnetically harder media has proven too difficult to write (alter magnetization) using traditional magnetic write head strengths/capabilities. In order for data to be recorded into this media, a local spot on the disk with dimensions of the desired bit size (10s of nanometers) must be heated close to its Curie temperature resulting in a significant drop of its magnetic coercivity, thus allowing the magnetic polarization to be switched under the applied field. The chosen method for locally heating the magnetic media in under-development devices is a plasmonic antenna, which focuses far-field optical light into high-intensity and rapidly decaying near-field optical energy, which is directed onto the recording medium (Figure 3.1a). The high-intensity near-field energy is capable of heating the magnetic media (only a few nanometers away) to the desired temperature while the rapid decay of the evanescent field ensures that the thermal gradient in the media is large so the resulting bit size is comparable to the size of the antenna and its near-field "spot." During drive operation the media is a fast-rotating disk, and as the disk rotates, the magnetic grains in the heated spot experience an applied magnetic field from the write pole, thereby switching their magnetization. Upon further disk rotation, the recorded bit is removed from the near-field hot spot, cools, and the magnetization is therefore "frozen" into the media. This technology is known as heat-assisted magnetic recording (HAMR), and it is capable of achieving the desired smaller bit sizes and higher areal densities.[12,13]

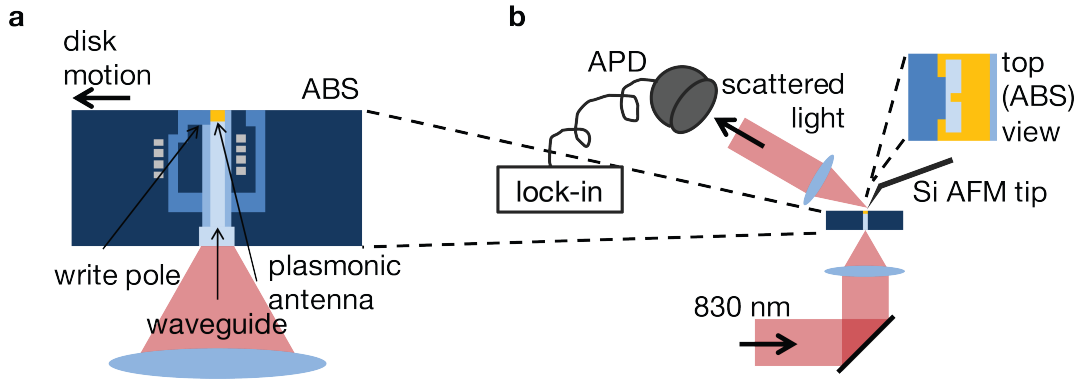

Figure 3.1: **Experimental layout.** (a) A side profile schematic of a HAMR head including the waveguide-coupled laser source which illuminates a plasmonic antenna located on the air-bearing surface (ABS). During operation, the ABS and plasmonic antenna are positioned only a few nanometers from the media surface. (b) Side profile schematic of the scattering scanning near-field optical microscopy (sSNOM) system showing the methods of illumination with an 830 nm laser and detection of silicon atomic force microscopy (AFM) tip-scattered near-field light with an avalanche photodiode (APD) and lock-in amplifier.

Designing, developing, and fabricating the HAMR technology has numerous challenges associated with the newly integrated laser, photonic, and plasmonic elements in addition to the magnetic elements already present. While electromagnetic simulations are immensely powerful and able to guide design and predict results, experimental characterization techniques are necessary to verify modeling results when compared to empirical observations of as-fabricated devices, which can be subjected to many variations, and to determine failure mechanisms. In HAMR, the introduction of a plasmonic antenna generating a deep subwavelength near-field spot calls for a characterization technique capable of investigating the properties and consistency of this crucial feature of the HAMR heads performance. Former work has demonstrated scattering scanning near-field optical microscopy (sSNOM) to be a top candidate for this task.[24,25,42,71–76]

3.2 sSNOM Background

SNOM was originally developed as a probe system with an aperture in a diaphragm,[77,78] which later was traded for a tapered optical fiber coated with metal such as gold, silver,

or aluminum.[79–81] Propagating far-field light inside the fiber is converted to near-field radiation by the angled metal coating and then illuminates the sample. This probe also serves to convert the sample-interacted near-field back into propagating far-field light, which would be observed back through the optical fiber. However, the resolution limit of apertured SNOM is determined by the dimensions of the aperture and the excitation wavelength so that as the aperture shrinks, the amount of electromagnetic energy coupled through the aperture and transmitted to the far-field falls off precipitously according to the Bethe limit ($\propto a^6/\lambda^2$).[82] (Bethes analytical near-the-hole solutions were later corrected by Bouwkamp,[83] and a modern discussion is provided by Novotny *et al.*[84]) As a result, for small aperture sizes, the near-field signal accessible using an aperture probe falls below the background and noise thresholds for the technique, thus limiting resolution of apertured SNOM to 50 nm for visible or near-infrared light. Because the HAMR plasmonic antennas are generally smaller than this size, a technique offering better resolution is necessary.

In sSNOM, the resolution of the SNOM technique is increased by incorporating an atomic force microscopy (AFM) scan probe tip that scatters, rather than transmits, the near-field light into the far-field, thus causing the sharpness of the AFM probe to determine the resolution rather than the size of the aperture and the wavelength.[85–88] For sub-ten-nanometer tip radii, the scattering cross-section of light is still more than sufficient to beat the signal-to-noise and signal-to-background limits when using a lock-in amplifier to detect the light scattered from the tip.[25] In the case of metallic or metal-coated tips, the tip both generates the probing near-field (through the "lightning rod" or "nanofocusing" effect)[64,65] and performs the function of a dipole scatterer by converting the sample-interacted near-field radiation back into far-field light that can be collected by an objective.[86–88] However, for HAMR plasmonic antennas (as well as for other general plasmonic structures), the near-field is generated by the sample (excited by an external source), and so tips with minimal signal disruption while still maintaining high scattering cross-sections are desired.[24] In this work, uncoated silicon tips with a typical radius of 5-15 nm and optically accessible tip apexes were used (see methods in Appendix A.1).

Given the large amount of background scattered light that is generally present in sSNOM measurements, the signal specific to the tip apex can be extracted through the

use of a lock-in amplifier tuned to the fundamental and higher harmonics of the AFM tip cantilevers resonant oscillation frequency.[25,89] Prior work has demonstrated that the lower order harmonics include both the propagating and evanescent components of the scattered light, while the higher order harmonics have a stronger dependence on the near-field strength and hence contain higher contrast near-field information.[25] The sSNOM system used to measure the HAMR plasmonic antennas (Figure 3.1b) in this work uses this lock-in driven technique and is capable of capturing up to three harmonics simultaneously during AFM measurements (Figure 3.2).

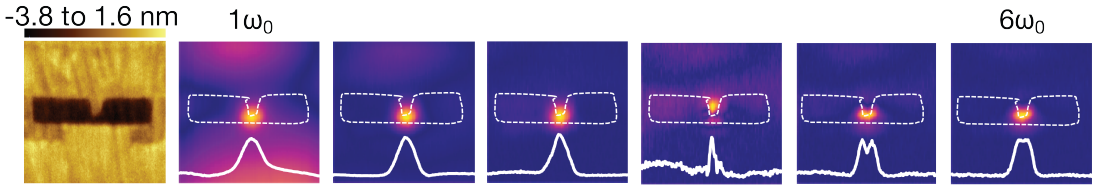

Figure 3.2: **sSNOM experimental output.** Plasmonic antenna AFM image together with near-field harmonic mappings collected from the first six harmonics of the AFM tip cantilever resonant frequency. The AFM image as well as the first three harmonics were collected simultaneously while the next three were collected in a second set of scans. Maps are 400 nm × 400 nm.

3.3 Predicting sSNOM behavior of mass-produced plasmonic devices

In order to use sSNOM to guide the design and development of HAMR devices, we developed a model to map the electric field data from electromagnetic simulations into the expected harmonic mappings generated by the sSNOM system. The first stage began with a few general approximations. It was assumed that the position of the AFM tip varied sinusoidally in time with the resonant frequency of the cantilever ($z \propto sin(\omega_0 t)$), that the evanescent electric field followed an exponential decay with increasing distance from sample surface z ($E \propto e^{-z}$), and that the scattering was proportional to intensity ($\sigma \propto E^2$). As expected, the model yields maximum scattering intensity when the tip is closest to the surface (Figure 3.3a, here $\omega_0 = 300$ kHz), and a fast Fourier transform (FFT) of the scattered field yields harmonics that decay exponentially in

intensity with increasing order. Using the sSNOM system and oscilloscope capabilities of the lock-in amplifier software, a scattering signal similar in shape to that of the simple evanescent approximation was observed when the tip was hovered (oscillating) over the center feature of the plasmonic antenna containing the most intense near-field signal (Figure 3.3c). Despite the noise present in this data, a numerical FFT still reveals several harmonics (Figure 3.3d). It is worth noting that this FFT is performed through numerical analysis of the captured time-domain oscilloscope trace, not by the lock-in amplifier hardware. The lock-in harmonic acquisition during imaging was performed with sufficiently long time constants in order to improve the signal-to-noise ratio in the higher harmonics significantly above the threshold apparent in this post-processed FFT trace.

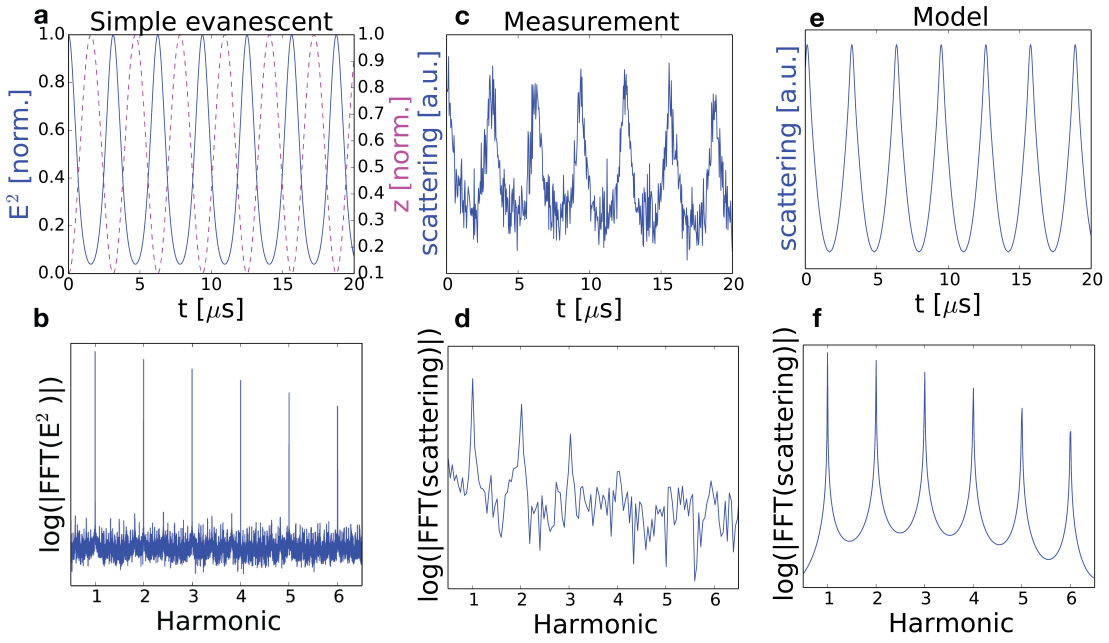

Figure 3.3: **Examining approximations for the measured harmonics.** Comparison of (a,c,e) scattering signal and (b,d,f) harmonics derived from the fast Fourier transform of the corresponding scattering signal for three situations: (a,b) general approximation where the tip height (z) above the ABS varies sinsoidally in time with frequency ω_0 and the electric field (E) decays exponentially with z, (c,d) measurements from the sSNOM system with the tip positioned over the plasmonic antenna, and (e,f) modeled scenarios as calculated using simulated electric field data and accounting for the tips effects.

Because the sSNOM system and HAMR devices are considerably more complex than the simple evanescent model, further improvements to the model were made to better match experimental conditions. To substitute for the simple evanescent electric field assumption ($E \propto e^{-z}$), data from electromagnetic simulations were introduced to account for the actual field expected for the as-designed dimensions of the HAMR plasmonic antenna. The tip-sample interaction was then accounted for in two stages. The first stage weights each 1 nm $\times$ 1 nm z-column (where the column is aligned normal to the surface of the sample) of simulated electric field data by a scattering parameter σ:[75,88,90,91]

$$E_{sSNOM} = \sigma E_{model} \tag{3.1}$$

which yields the scattering parameter adjusted electric field. The scattering parameter σ is derived from a spherical probe and image dipole interaction and is defined by the following set of equations:[77,86,88]

$$\begin{aligned} \sigma &= \alpha_{eff} \frac{\pi \sqrt{\frac{8\pi}{3}}}{\lambda^2} \\ \alpha_{eff} &= \frac{\alpha(1+\beta)}{1 - \frac{\alpha\beta}{16\pi(a+z)^2}} \\ \alpha &= 4\pi a^3 \frac{\epsilon_t - 1}{\epsilon_t + 2} \\ \beta &= \frac{\epsilon_s - 1}{\epsilon_s + 1} \end{aligned} \tag{3.2}$$

where α_{eff} is the effective polarizability of the tip-sample combination, α is the polarizability of the silicon tip (approximated here as a sphere), λ is the free space wavelength of the incident light, and ϵ_t and ϵ_s are the complex dielectric functions of the tip and sample, respectively. ϵ_s was allowed to vary based on the material (either gold, oxide, or magnetic material) located directly below the z-column being computed.

After applying the scattering transformation to the electric field, the second stage accounted for the shape of the tip. Planar slices of the resulting weighted electric field parallel to the air-bearing surface (ABS), which is the surface facing the rotating magnetic media containing the plasmonic antenna (in the xy plane), were serially convolved with two matrices with each representing different components of the shape of the AFM

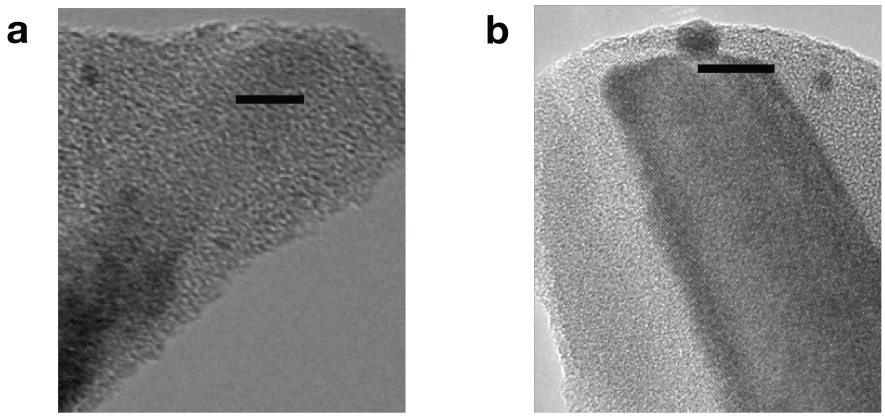

Figure 3.4: **TEM images of AFM tips.** A transmission electron microscopy (TEM) image of (a) a better-than-average 5 nm radius tip and (b) an average 10 nm tip, both coated with material (likely from the head) after scanning. Scale bars 5 nm and 10 nm, respectively.

tip. One matrix was designed as a cone to represent the shape of the tips shaft, and the other matrix was designed as a top-hat to represent the shape of the end of the tip. After these convolutions, for a 1 nm $\times$ 1 nm z-column positioned directly above the plasmonic antenna, it can be seen that the modeled time-dependent scattered field (Figure 3.3e) more closely matches the shape of the measured scattered field of the sSNOM signal (Figure 3.3c) than does the scattered field resulting from the simple evanescent model (Figure 3.3a). Similarly, a FFT of this modeled sSNOM signal (Figure 3.3f) mimics the behavior of the measured signal from the lock-in amplifier (Figure 3.3d) yielding smooth harmonic spikes, and when performed over the entire xy plane, yields the desired modeled near-field harmonic mappings.

3.3.1 Effects of the AFM Tip's Shape

Development of the sSNOM model required further investigation of the AFM tips local shape interacting with the high-intensity near-field. Based on manufacturer specifications, our experience, and previous transmission electron microscopy (TEM) images, it was assumed that most tips used in these experiments contained a 5-15 nm radius, where the sharper tips (5 nm radius, Figure 3.4a) gave a sSNOM signal with better resolution than average (10 nm radius, Figure 3.4b) or blunter (>15 nm radius) tips.

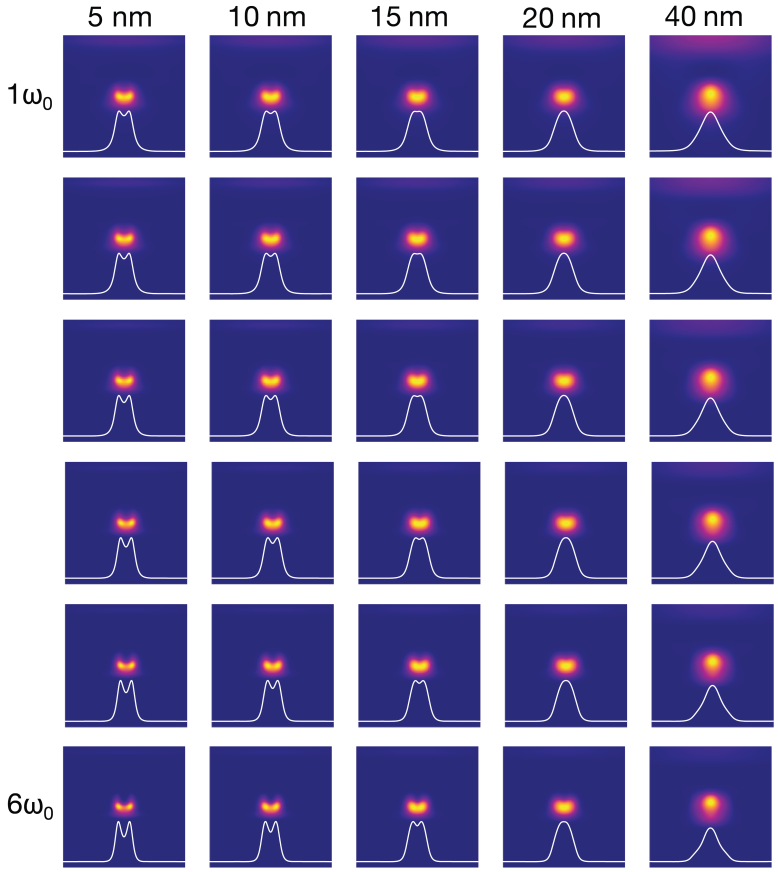

Figure 3.5: **Tip radius effects.** Near-field maps of the modeled system as a function of tip radius and harmonic assuming the silicon portion of the tip has a distance of closest approach (DCA) to the sample of 8 nm. Near-field maps are 400 nm × 400 nm.

Furthermore, TEMs of tips imaged post-scanning revealed several nanometers of material built up on the tip, including in the region separating the silicon tip from the sample. Therefore, the corresponding change in tip-sample separation was accounted for in the sSNOM model in addition to the tips radius. The TEM images also revealed the angled nature of the used tips shaft as well as the flat top-hat nature of its end.

Both the shape of the tips shaft as well as its end were incorporated into the sSNOM model through the two convolution matrices described above. The shaft was approximated as a cone with a half-angle of 9°, and the tip end was approximated as a top-hat (step function in cylindrical coordinates) with variable radius. Radii of 5, 10, and 15 nm

represented the range of usual tips while radii of 20 and 40 nm represented more extreme cases of blunt tips (Figure 3.5c). Based on the developed sSNOM model and previous experience with these tips, a radius of 15 nm was used in the model for correlation with the experimental data. Further improvement of the model is possible through the use of a three-dimensional volumetric convolution, rather than two-dimensional planar convolution used in this work, of the conical tip shaft matrix (including the tips angled rather than vertical approach) with the scattered field, which is expected to more accurately model the physical configuration and may increase the far-field contribution to the ω_0.

3.3.2 Effects of the AFM Tip's Distance of Closest Approach

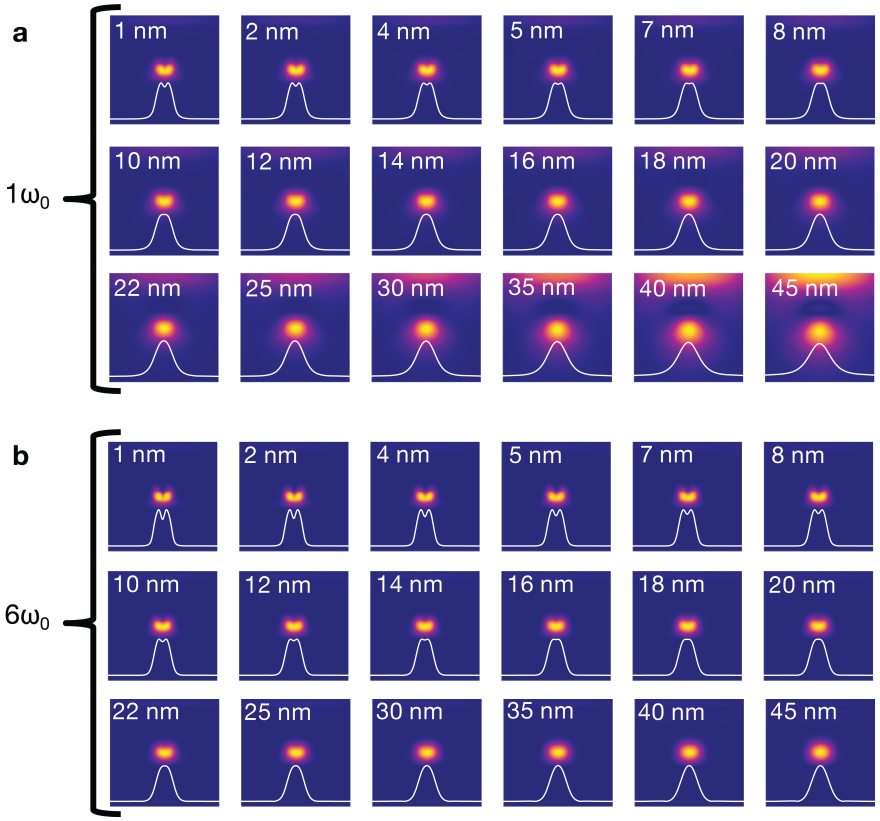

Figure 3.6: **Modeled near-field data as a function of distance of closest approach (DCA) and harmonic assuming a 15 nm tip radius.** (a) At the tip cantilevers resonant frequency ω_0. (b) At $6\omega_0$. Near-field maps are 400 nm × 400 nm. See Figure B.1 for all harmonics.

Further investigation of the mechanical AFM behavior of the sSNOM system was performed in order to determine the tips distance of closest approach (DCA) to the sample. In the sSNOM model, the DCA value was set as the minimum z height (and cutoff) for the FFTs of the scattered signal. It was found that the chosen DCA had a significant effect on the sSNOM models results (Figure 3.6). A smaller DCA (tip approaches much closer to the ABS) incorporates much more of the dominant near-field signal (as opposed to the weaker far-field signal) into the FFT, which becomes evident in the harmonic maps for the fundamental frequency (ω_0, Figure 3.6a) when compared with the higher $6\omega_0$ frequency (Figure 3.6b). Maximum intensity plots are also included for all investigated harmonics and DCA values in Figure 3.7 and B.2. A complete set of harmonics can be found in Appendix B.1.1.

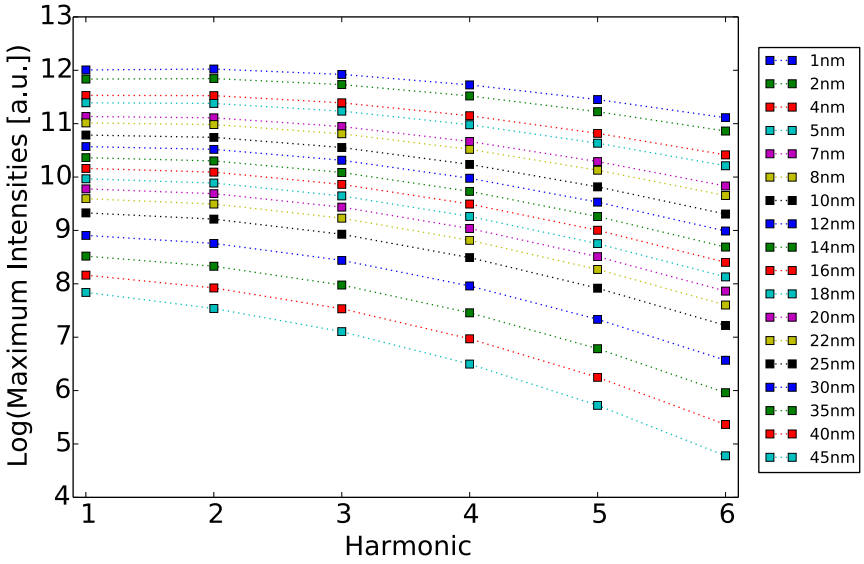

Figure 3.7: **Maximum intensity vs. DCA and harmonic.** The decay relationship of the maximum intensity of each mapping as a function of both DCA height and harmonic. Faster decay is observed for higher DCAs as well as for higher harmonics.

Estimation of tip DCA was also performed with a mechanical model of tapping mode AFM, which solves the equation of motion for the cantilever numerically as it encounters tip-sample forces modeled to include van der Waals attraction, capillary adhesion due to a water layer, and Pauli hard sphere repulsion.[92] When inputting the tip radius, free amplitude, and amplitude setpoint, and using the measured phase signal as a check for

accuracy, the model shows that the cantilever was oscillating in the repulsive regime indicating that the tip approaches the surface very closely and experiences repulsive contact with the sample at the bottom of most oscillations.

3.3.3 Final Model Results

Accounting for the thickness of material collected by the tips during scans (∼5 nm in Figure 3.4) as well as other complex effects due to the water meniscus between the tip and the sample surface,[92,93] and comparing the experimentally measured data with the sSNOM models results, a DCA of 8 nm was chosen together with a tip radius of 15 nm to represent the best fit of the sSNOM model to the experimental measurements and expectations. A "good fit" between the harmonic maps generated by the sSNOM model and the experimental data was established when a bifurcated near-field signal was observed in the higher order harmonics ($5\omega_0$, $6\omega_0$) but not in the lower order harmonics ($1-3\omega_0$). The visible near-field bifurcation requirement for the higher harmonics ruled out the possibility of the experimental tip having a radius of 20 nm or larger since no bifurcation was evident, even in the $6\omega_0$ (Figure B.4), when the chosen distance of closest approach was 1 nm (the closest possible in the present model). In addition, good qualitative agreement between the experimental and modeled near-field maps using smaller tip radii (<15 nm) required DCA values exceeding expectations and so were ruled out by the AFM mechanical model (Figures B.6-B.9). Since the sSNOM models results show significant dependence on the DCA, incorporating simulated electric field data with topographic sensitivity (the presented simulations assumed a planar surface) would more closely match the experimental conditions revealed by the recessed nature of the waveguide relative to the antenna seen in the AFM image and could improve the model.

Slices of the simulated electric field intensity at different heights of interest (Figure 3.8a, with further details included in Appendix B.1.5) are compared to the corresponding harmonics from the sSNOM model results using a tip radius of 15 nm and a DCA of 8 nm (Figure 3.8b) and the experimentally measured harmonic maps (Figure 3.8c). From this comparison, it can be seen that higher harmonics, such as $5\omega_0$ and $6\omega_0$, are more representative of the near-field in the region that would be occupied by the magnetic media during drive operation than their lower order harmonic counterparts.

The nature of the higher order harmonics in which this relationship was found signified the prescribed rapid change in near-field intensity closer to the plasmonic antenna.

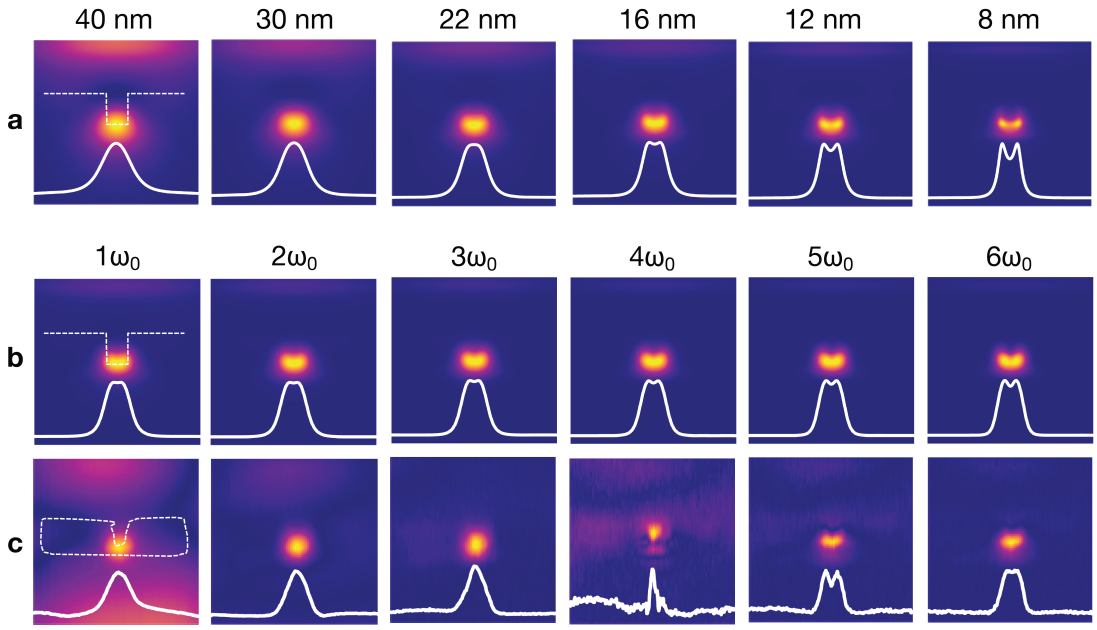

Figure 3.8: **Final result of model derived from simulated data and compared to measured data.** Comparison of a. simulated electric field intensity, b. modeled near-field images, and c. sSNOM measured near-field images. All maps are 400 nm × 400 nm.

The strange behavior exhibited by the measured $4\omega_0$ was likely caused by a non-sinusoidal feature at the bottom of the tips oscillation due the tips possible contact with and/or repulsion by the sample surface during its motion. The non-sinusoidal motion of the tip was not accounted for in the present sSNOM model, but it could be introduced upon further mechanical characterization of the sSNOM-tip system and its interaction with the sample. An introduction of a sharp change in the peak scattering would surely become evident in one or more of the higher order harmonics in the presence of non-sinusoidal tip oscillation. In the case of this experiment, this feature was found in the $4\omega_0$, and it is also expected to have been present in the $8\omega_0$, etc. This observation as well as the AFM mechanical model results and the flat nature of the post-scanning tips suggests that the scan parameters cause significant tip interaction with the sample likely leading to the tips top-hat shape. Scan parameters for typical non-contact tip

operation involve small oscillation amplitudes that fail to sweep sufficient evanescent field variation and are not capable of performing the desired full characterization of the plasmonic antennas near-field. For this reason, large oscillation amplitudes were used that resulted in greater tip-sample interactions.

In conclusion, sSNOM is a useful technique capable of characterizing HAMR heads for next-generation hard disk drives. The development of a sSNOM model to translate from simulated electric field data was necessary in order to derive meaning from the measured near-field harmonics. Furthermore, the same model approach can be applied to other plasmonic structures across many disciplines and applications.

Chapter 4

Bidirectional characterization of waveguide-coupled plasmonic antennas by near-field excitation and mapping

Frontier devices are incorporating light at nanoscale dimensions and require new methods of characterization for device development and optimization. For example, coupling behavior between laser diodes, photonic waveguides, and plasmonic structures needs further rigorous academic study. Nevertheless, this behavior is critical to the functioning of next-generation hard disk drives (HDDs), which remain the primary storage mechanism for the worlds increasing data storage needs (*i.e.* "the cloud"). Performing complementary and bidirectional optical characterization is a powerful strategy to more fully understand the mechanisms and behavior of photonic waveguides coupled with plasmonic antennas. When illuminated with resonant far-field laser light, plasmonic antennas can generate intense and deeply sub-wavelength evanescent near-fields. These plasmonic devices can also be characterized in reverse by exciting plasmonic antennas with focused electron beams, which generate local sub-wavelength optical excitations through cathodoluminescence (CL) that are coupled out to the far-field. Bidirectional observation of waveguide-couple plasmonic antennas can offer unique insight into device

function and performance.

4.1 Bidirectional Characterization

As discussed in Chapter 3.1, heat assisted magnetic recording (HAMR, Figure 4.1a, B.13b) has been identified as the best solution to overcome the superparamagnetic limit, which dictates the magnetic media coercivity necessary to record thermally stable data "bits" of a given size. The available write field strength limits storage density.[12,13,42,69,70] Smaller bits require magnetically "stiff" media whose polarization cannot be flipped with the magnet in a traditional perpendicular magnetic recording head (Figure B.13a) without assistance. HAMR incorporates a plasmonic antenna that acts as a local heater of the magnetic media by coupling energy from far-field laser light into near-field radiation.[12,13,42] This high-gradient optical field heats a tight spot on the magnetic media close to its Curie temperature significantly reducing its coercivity and enabling its polarization to be written by the recording head. Since the drive's performance and the size of the recorded bit is now determined by the plasmonic antenna (Figure 4.1b), the success of the technology requires a good understanding of the antenna and waveguide coupling mechanism. Appropriate characterization techniques must be employed to investigate as-fabricated recording heads containing plasmonic antennas as well as their waveguide couplers. Scanning electron microscopy cathodoluminescence (SEM-CL, Figure 4.1c) and scattering scanning near-field optical microscopy (sSNOM, Figure 4.1d) were used to perform this bidirectional near-field characterization of waveguide-coupled plasmonic antennas in HAMR heads.

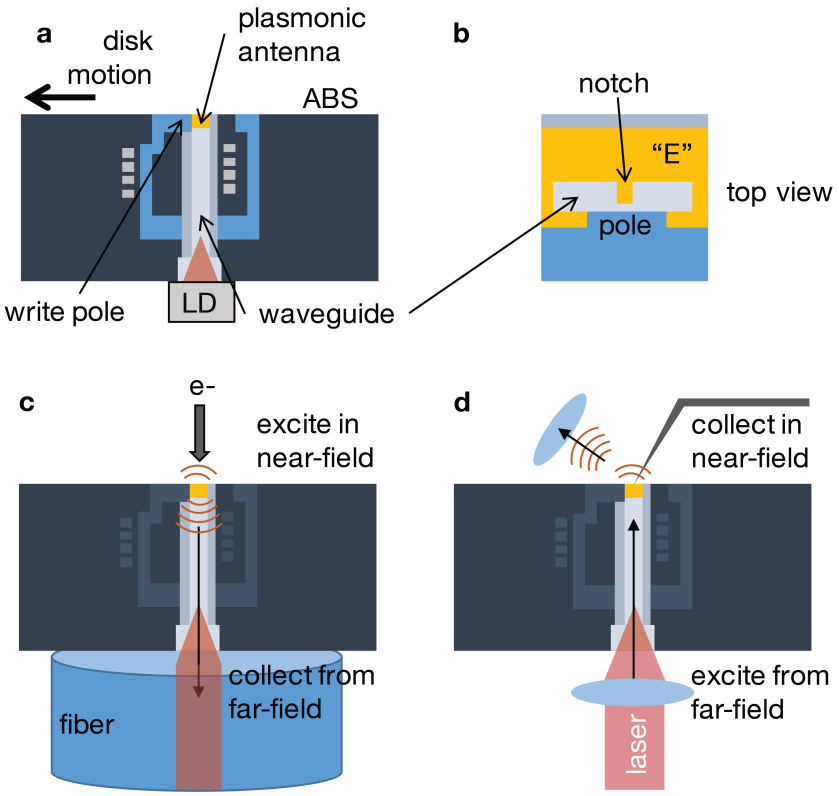

Figure 4.1: **Schematics for bidirectional near-field characterization.** (a) side profile of a heat-assisted magnetic recording head (LD: laser diode, ABS: air-bearing surface), which incorporates a (b) waveguide-coupled plasmonic antenna. Bidirectional near-field characterization was performed using (c) scanning electron microscopy cathodoluminescence and (d) scattering scanning near-field optical microscopy.

4.2 Scanning Electron Microscopy Cathodoluminescence

Cathodoluminescence (CL) occurs when electrons incident on a material cause the emission of photons through material-dependent coherent (plasmons) or incoherent (minority carrier generation and recombination, color center excitation) processes.[22,23] The resulting CL photons can be spatially mapped and spectroscopically analyzed with SEM. Hyperspectral maps of nanostructured optical response of the sample can be obtained with resolution approaching 10 nm. SEM-CL has been used to generate plasmon resonance maps of metallic nanostructures,[94–98] and in this work it was used to probe the

response of the waveguide-coupled plasmonic antenna incorporated into a prototype HAMR head. While the electrons have easy access to the plasmonic antenna located at the top of the head on the air-bearing surface (ABS), full characterization of the head's optical system requires collection of the CL photons at the output of the head's integrated waveguide.

Samples containing multiple HAMR heads were mounted above an optical collection fiber (Figure B.14) in a custom holder (Figure B.15). The CL photons output from the fiber were then coupled either to a spectrometer and CCD camera or to a photon-counting APD (avalanche photo-diode) with a band-pass filter as the electrons were raster scanned over the antenna region (Figure B.16). Intensity mappings were generated by integrating the signal over 20 nm wavelength windows to better observe the head's (antenna's) resonant behavior as a function of output wavelength. Near 625 nm (Figure 4.2a), the right side at the top metal face of the E-shaped antenna exhibits the strongest resonance. With increasing wavelength, a resonance begins to appear at the "notch" region (center of the "E") as the side resonance begins to disappear (Figure 4.2b, B.17). Near 750 nm (Figure 4.2c), the output CL photons are localized to only the notch region.

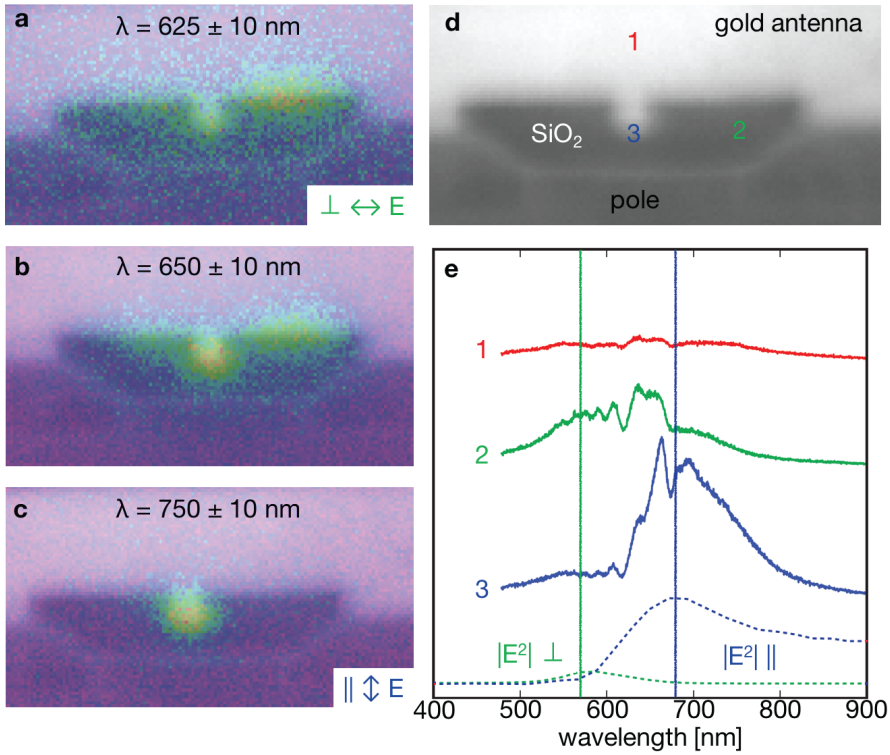

Figure 4.2: **CL analysis as performed inside a scanning electron microscope.** (a-c) Full field intensity maps were collected over the antenna region for discrete and narrow (20 nm) wavelength windows revealing the spatial location of the resonances on the air-bearing surface. (Additional maps for other wavelengths can be found in Figure B.17.) E-antenna notch width ∼50 nm. Based on these maps, (d) three distinct and different points on the air-bearing surface surrounding the plasmonic antenna were chosen and (e) full spectra were compared with modeling.

Complete spectra shown in Figure 4.2e were collected from three regions of interest marked in Figure 4.2d: 1. Approximately 100 nm above the center of the "E" notch (a low CL intensity reference), 2. The region to the right of the notch overlapping with the waveguide (resonant near 625 nm), and 3. The notch region, which localizes the optical field for heating the magnetic media (resonant near 665-760 nm, Figure B.17). The antenna is designed to be resonant at 830 nm during drive operation, but this resonance is blue-shifted when no magnetic media is present. Features in the spectra (Figure 4.2e) can be attributed to three sources. First, the plasmonic resonance is evident as the broad feature matching the modeled profiles. Second, the sharp peaks near 650 nm are

due to the well-known luminescence of oxygen-rich SiO_2.[99] Finally, the lower wavelength bumps are likely due to wavelength-dependent cavity effects from the waveguide itself.

The results of wavelength and polarization-dependent electromagnetic simulations of field intensity at the disk height when the antenna is excited through the integrated waveguide are shown for region (3) at the bottom of Figure 4.2e. The waveguide-antenna system was engineered to focus parallel-polarized light (relative to the notch) to position (3) at resonance, while perpendicular-polarized light is neither focused nor resonantly enhanced at the notch region but does exhibit a delocalized mode spread throughout the stem of the E.[64,65] The CL collection system using the multimode fiber (Figure B.14) did not preserve the polarization of the transmitted light, but it is believed that the general agreement between the shape of the CL spectra in region (3) with the parallel simulation is consistent with CL excitation of the plasmonic resonance. The spectra of region (2) may be due to excitation of the delocalized perpendicular waveguide mode combined with luminescence from the SiO_2, while region (1) does not couple well to the waveguide modes. The experimental system could be improved through the use of a polarization-maintaining optical fiber for collection.

4.3 Scattering Scanning Near-field Optical Microscopy

Scattering scanning near-field optical microscopy (sSNOM) was used to directly map the near-field intensity distribution of the HAMR device close to the ABS as a function of the waveguide excitation wavelength and polarization. sSNOM uses an atomic force microscopy (AFM) tip as a local scattering center, coupling near-field light into the far-field where it can be collected by an objective for detection.[85–88] With the use of a lock-in amplifier to record different harmonics of an AFM tip oscillating at the cantilever resonant frequency (ω_0), the desired near-field signal can be separated from the background far-field light with good signal-to-background sensitivity.[25,89] sSNOM is an excellent technique for probing plasmonic structures,[24,71,73,74] and was used to characterize the behavior of a HAMR waveguide-coupled plasmonic antenna both in this work as well in our previous work.[42] In these sSNOM experiments, external laser light was coupled into the integrated HAMR waveguide exciting the plasmonic antenna much like in drive operation (Figure B.18). As the sample scanned under the oscillating tip,

the different harmonic components of the scattered signal were collected and mapped. As reported previously, the higher harmonics ($5\omega_0$ - $6\omega_0$) were more representative of the near-field profile as seen by the magnetic disk during drive operation. Near-field maps were collected for six harmonics over a range of incident laser polarizations (-100° to 100° in increments of 10° where 0° was parallel to the notch) for incident wavelengths of 830 nm (Figure 4.3a), the designed head operation wavelength, as well as 633 nm (Figure 4.3b) in order to more fully map out the HAMR performance and to complement the SEM-CL measurements.

Several observations can be made from the data in Figure 4.3. The harmonics intensity for the 830 nm light is >10× that of the 633 nm light, which was expected since the head (waveguide and plasmonic antenna) was designed to operate at 830 nm. At this wavelength, the polarization dependence of nanofocusing was observed for all harmonics (Figures 4.3a,c, B.19 - B.21), with the expected maximum intensity for parallel (0°) excitation and minimum intensity for perpendicular (-90° and 90°) excitation.[64,65] The observed maximum intensities deviated from the expected $cos^2(\theta)$ dependence on polarization angle θ near the parallel polarization.[68] It is believed that this was an experimental artifact due to saturation of the APD or the lock-in preamplifier due to the large far-field transmission of the waveguide at resonance, which does not have a heating effect on the media. The waveguide was designed to operate most efficiently with parallel polarization at 830 nm, and only a fraction of the laser light is converted to the evanescent near-field by the plasmonic antenna. It is worth noting that follow-up measurements of the 0° parallel polarization were performed with care to eliminate saturation. Similar decay trends in maximum intensity as a function of harmonic were observed when compared to the saturated set presented here confirming the cause of the saturation, demonstrating its spatially uniform nature, and validating the presented near-field mappings.

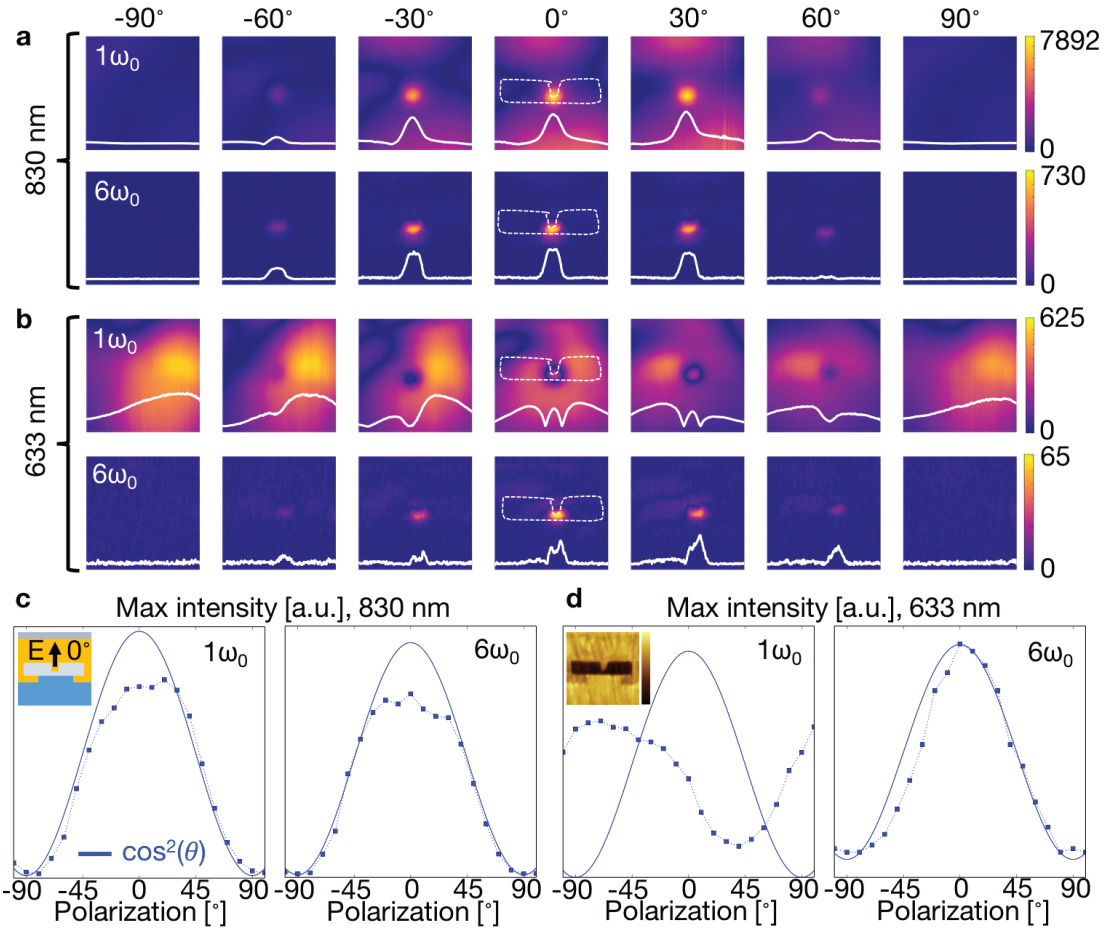

Figure 4.3: **sSNOM images of HAMR heads as a function of wavelength and polarization.** Near-field maps for the $1\omega_0$ and $6\omega_0$ with both (a) 830 nm and (b). 633 nm wavelengths as well as polarizations ranging from -90° deg (perp, TE) to 0° (para TM) to +90° (perp, TE). All maps are 400 nm ×400 nm. The intensity maxima from all maps were extracted and plotted against the expected $cos^2(\theta)$ intensity decay curve for both (c) 830 nm light and (d) 633 nm light. The full data set ranged from -100° to 100° in increments of 10° and covered six harmonics for both wavelengths. The AFM color scale ranges from -3.8 to +1.6 nm, and the map is 400 nm × 400 nm. Additional images can be found in Appendix B.2.2.

The background saturation observed in the 830 nm data set was not observed in the data set collected using 633 nm laser light as is evident in Figure 4.3d right (and Figures B.22 - B.24) in which the $6\omega_0$ nicely follows the expected $cos^2(\theta)$ decay trend. In addition, the presence of a near-field resonance of smaller intensity for the parallel (0°)

electric field matched the results from the SEM-CL measurements and modeling. The fundamental frequencys ($1\omega_0$) harmonic mappings also show the same behavior as observed with SEM-CL; with perpendicular electric field polarizations (-90° and 90°), the recorded intensity of the resonance was dominant on the right of the E-shaped antennas notch feature. Comparing the sSNOM near-field mappings in Figure 4.3b, $1\omega_0$ with the SEM-CL map in Figure 4.2b centered at 650 nm suggests that this wavelength region of SEM-CL data is largely comprised of CL photons with a variety of polarizations, especially when considering the presence of a smaller relative intensity feature on the left side of the notch as well as the reduced intensity of the rightmost feature relative to the intensity maximum located at the notch. Since the fundamental frequencys ($1\omega_0$) scattering cross-section is known to couple more light from the optical far-field, and these side resonances are not present in the higher harmonics ($6\omega_0$), we can conclude that the corresponding SEM-CL signal (625-675 nm) is more likely due to optical excitations that couple well into the far-field modes of the waveguide-plasmonic antenna system. These characterizations of the near- versus far-field and polarization components for the different features observed in the SEM-CL and sSNOM maps are also consistent with the simulated spectra for the antenna. The complete set of near-field mappings for all measured polarizations, wavelengths, and six harmonics as well as their maximum intensity curves can be found in Appendix B.2.

In conclusion, the optical near-field of waveguide-coupled plasmonic antennas in HAMR heads was characterized bidirectionally with both near-field excitation mapping and probed near-field mapping using SEM-CL and sSNOM. Both techniques were able to provide unique insight into the heads behavior during drive operation and conclusions drawn from their results exhibited good agreement. Furthermore, the usefulness of the described methods has been firmly demonstrated for the development of HAMR technology as well as future devices based on the near-field properties of light.

Chapter 5

Plasma-enhanced Atomic Layer Deposition for Plasmonic Titanium Nitride

For many years, the plasmonics community has searched for alternative materials in hopes of resolving issues with common plasmonic metals (*e.g.* gold, silver, etc.).[14,16,43,49,100,101] Successful use of plasmonics within many applications, especially on the industrial scale, have been limited by losses,[14,100] poor surface adhesion,[102,103] a lack of well-controlled nano-scale fabrication processes, as well as chemical, thermal, and mechanical instabilities.[16,76] However, synthetic metals have the potential to overcome some of these challenges and thus enable the widespread use of plasmonics and improvement of plasmonic structures and devices.[46] For applications in the visible and near-infrared, most of the focus of synthetic metal studies have been on transparent conducting oxides and nitride materials, with particular focus on titanium nitride as the best potential rival for gold.[19,37,46,47,50] Traditional methods for depositing titanium nitride have many disadvantages for industrial applications and are incompatible with processing requirements. For example, the most common technique for depositing titanium nitride is sputtering performed at 700-800°C,[19,35,50] which far exceeds the temperature limits of 400°C for the CMOS industry and 200°C for the heat-assisted magnetic recording (HAMR) industry.[20] Sputtered titanium nitride films have substrate dependent properties and

orientation effects related to epitaxial nucleation,[47] which does not lend itself well to inhomogeneous substrates with non-planar features. As an alternative, we deposit titanium nitride by plasma enhanced atomic layer deposition (PEALD),[20,58,104,105] a conformal technique capable of coating three-dimensional surfaces with Ångström-level thickness resolution at low temperatures (300°C).

5.1 Plasma-enhanced Atomic Layer Deposition

In this work, deposition of titanium nitride was performed via conventional PEALD (Oxford FlexAL) with cycling as shown in Figure 5.1. First, (Figure 5.1a) a precursor gas, tetrakis(dimethylamino)titanium (TDMAT), was introduced into the vacuum chamber (base pressure $\sim 10^{-6}$ Torr) and reacted with the substrate surface at 300°C, followed by a pumping/purging step to remove unreacted precursor gases. Next, a plasma of H_2 and N_2 gas (Figure 5.1b) was introduced whose radicals perform two functions: hydrogen radicals assist the removal of $[(CH_3)_2N]$ ligands from the metal-organic precursor, and nitrogen radicals bond to open titanium sites. After a designated time, these gases were removed, and one cycle of PEALD was complete (Figure 5.1c) leaving behind no more than one atomic layer of titanium nitride. These processes usually deposited $\sim$1 Å/cycle, or $\sim 1/4$ atomic layer of titanium nitride per cycle. Recipes for the films discussed in this paper are given in Table 5.1, and chamber conditions (either after cleaning or seasoned with previous oxide depositions) are given throughout the text.

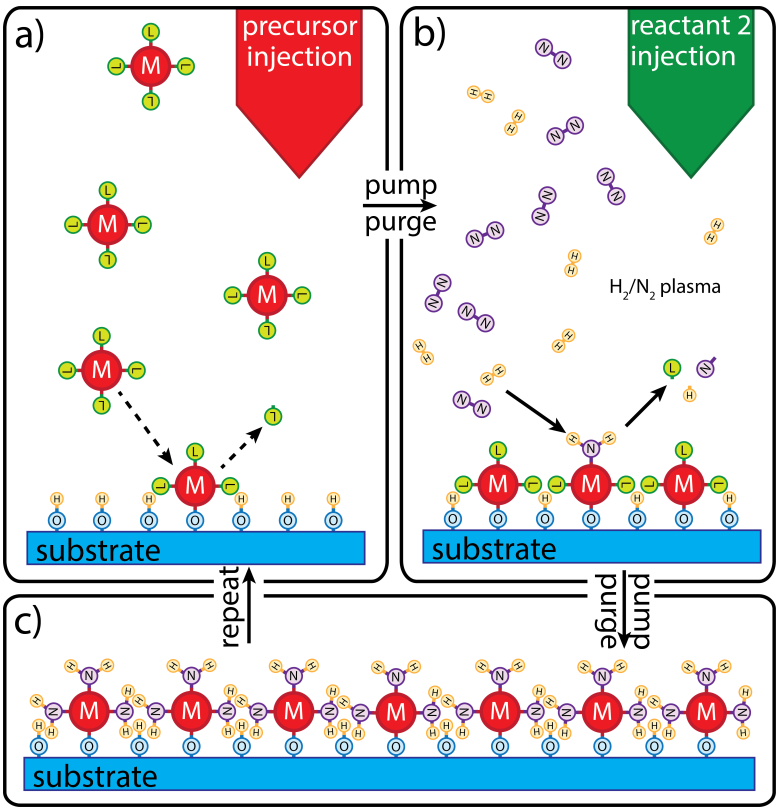

Figure 5.1: **Deposition process.** Plasma-enhanced atomic layer deposition processing of titanium nitride includes (a) a precursor reaction step with TDMAT followed by (b) a plasma step with H_2 and N_2 gases to create (c) a thin titanium nitride coating on the substrate surface each cycle.

	Recipe 1	**Recipe 2**
PRECURSOR		
Dosage (s)	0.8	0.8
Pressure (mTorr)	40	40
Purge (s)	3	3
PLASMA 1		
Gas(es)	N_2	N_2, H_2
Flow rate (sccm)	40	20, 20
Pressure (mTorr)	10	10
Time (s)	10	30
PLASMA 2		
Gas(es)	N_2, H_2	
Flow rate (sccm)	3, 50	
Pressure (mTorr)	10	
Time (s)	30	

Table 5.1: **Deposition recipes.** Deposition recipes for the films discussed in this paper. The N_2 present in the second plasma of Recipe 1 aids the striking of the H_2 plasma.

5.2 *In situ* Spectroscopic Ellipsometry

Spectroscopic ellipsometry (J. A. Woollam M2000) was performed *in situ* at the end of each titanium nitride deposition cycle to monitor growth and aid in process development. The ellipsometer was used to record the amplitude (Ψ, Figure 5.2a) and phase (Δ, Figure 5.2b) from ∼200-1700 nm. Models to approximate the optical and physical properties of the sample (including the substrate) were developed, and two types of models for the titanium nitride layer were compared. First, a physical model with one Drude and three Lorentz oscillators was chosen, where the dielectric function, $\epsilon(\omega)$, is defined as:

$$\epsilon_m(\omega) = \epsilon_\infty - \frac{\omega_p^2}{\omega^2 + i\gamma\omega} + \sum_{j=1}^{3} \frac{f_j \omega_{0,j}^2}{\omega_{0,j}^2 - \omega^2 - i\gamma_j \omega} \tag{5.1}$$

where ω_p and γ are the plasma frequency and damping, respectively, for the Drude parameter, $\omega_{0,j}$ and $\gamma_{0,j}$ are the j^{th} Lorentz oscillator frequency and damping, respectively, and f_j is the j^{th} amplitude of the Lorentz oscillator. For a 300 cycle film (Recipe 1 deposited on 250 nm thermal silica on a silicon wafer in a clean chamber), the resulting fit parameters are included in Table 5.2. The fit quality was defined by the (root) mean square error (MSE), a difference between the model fit and the measured data,[32] and was found to be 12.7.

Parameter	**Fit Value**
Thickness	27.3 nm
$\hbar\omega_p$	4.85 eV
$\hbar\omega_1$	0.920 eV
$\hbar\omega_2$	4.11 eV
$\hbar\omega_3$	6.07 eV
$\hbar\gamma$	0.706 eV
$\hbar\gamma_1$	0.974 eV
$\hbar\gamma_2$	2.39 eV
$\hbar\gamma_3$	3.49 eV
f_1	19.9
f_2	1.89
f_3	3.43
ϵ_∞	3.00

Table 5.2: **Ellipsometry material parameters.** Spectroscopic ellipsometry Drude-Lorentz model fit results for a 300 cycle titanium nitride film deposited with Recipe 1.

Mathematically-based B-spline models, including Kramers-Kronig rules, have been used to fit plasmonic and refractory materials,[106,107] and so the B-spline was also applied to the 300 cycle titanium nitride film yielding a more accurate fit (MSE 7.23, Figure 5.2a,b) with a thickness of 27.1 nm, initial refractive index values of n = 2 and k = 1, 0.1 eV resolution (58 points), ϵ_∞ = 3.00, IR amplitude = 6.77, and IR damping = 0, and a resulting node graph (Figure 5.2c). $\epsilon_m^{'}$ and $\epsilon_m^{''}$ (Figure 5.2d,e) were extracted from

the titanium nitride layer in both models. While appearing very similar, comparing their corresponding figures of merit ($FOM = -\epsilon_m^{'}/\epsilon_m^{''}$, Equation 2.14), a quantitative measure of the plasmonic quality of the film, shows a ∼10% difference at 750 nm (Figure 5.2f).

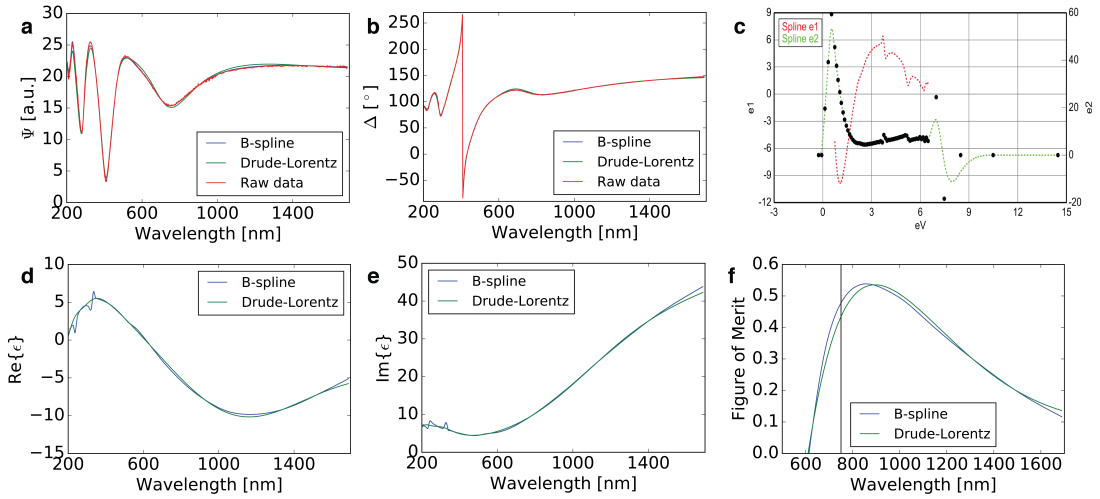

Figure 5.2: **Ellipsometry fitting methods.** Spectroscopic ellipsometry was performed in situ during titanium nitride deposition (300 cycles of Recipe 1 yielded 27.3 nm of titanium nitride as fit by the Drude-Lorentz model), and the output data was fit with two models to extract the complex dielectric function. Both a physical model with one Drude and three Lorentz oscillators as well as a mathematical B-spline model with Kramers-Kronig rules were used. Their fits are compared in (a,b,c) as well as their (d,e) extracted pseudo dielectric functions and (f) figure of merit (FOM). The fitting parameters are included in Table 5.2.

In situ spectroscopic ellipsometry of a 2250 cycle deposition (Recipe 1 deposited on 250 nm thermal silica on a silicon wafer in a clean chamber) yielding a ∼216 nm titanium nitride film shows how the film properties evolve during deposition. Using the more physically accurate (and meaningful) Drude-Lorentz model, the data was fit at numerous cycle intervals (100, 150, 300, 500, 800, 1000, 1250, 1500, 1900, and 2250 cycles) corresponding to increasing film thicknesses (8, 12, 24, 42, 69, 89, 117, 144, 180, 216 nm). The most significant changes were observed in the real part of the dielectric function (Figure 5.3a), which was believed to be due to the improved carrier concentration and mobility (i.e. more conductive and metal-like) as a result of

the cumulative plasma time exposure of the films earlier-deposited material throughout the deposition process and more bulk-like nature of the thicker films. In contrast, the imaginary part of the dielectric function exhibited little change, but it did appear to gradually decrease with increasing film thickness. The FOM was also calculated and more clearly shows the films optical properties and the wavelength range over which it is plasmonic.

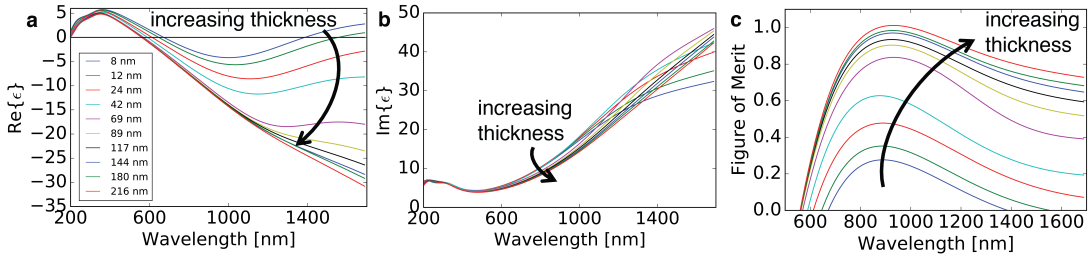

Figure 5.3: **Thickness dependence of optical properties.** *In situ* spectroscopic ellipsometry revealed the evolution of a film throughout its growth process. Thin films (<10 nm) are plasmonic, but barely, and are not optimal. As the thickness grows, the $\epsilon_m^{'}$ shows significant improvement, which may be due to the improvement of the films electrical properties (higher carrier concentration and mobility) as a result of the longer cumulative plasma time and the increase in thickness. Thick films have the best plasmonic properties.

5.3 Auger Electron Spectroscopy

With spectroscopic ellipsometry it is possible to determine the optical and electronic properties of titanium nitride films, as well as their thicknesses, but it cannot reveal differences in chemical composition due to varying deposition schemes and chemistries or to varying starting conditions of the PEALD chamber. If two nominally equivalent films yield different ellipsometry results, elemental composition should be measured, and here Auger electron spectroscopy (AES) was used for such a case where residual films in the PEALD chamber were suspected to release contaminants.

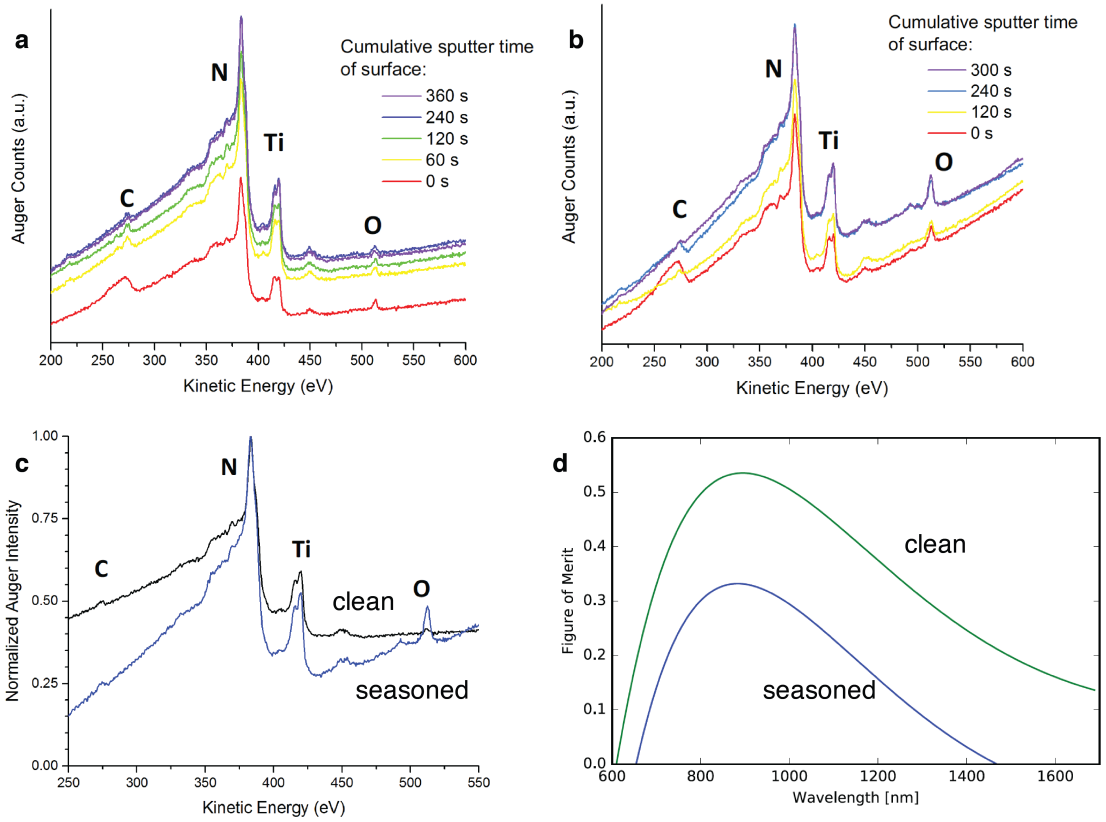

Figure 5.4: **Effects of deposition chamber condition.**Reliable PEALD deposition is dependent on the chamber conditions, especially the plasma tubes cleanliness. Two comparable film chemistries yielded strikingly different results when deposited in (a) a clean vs. (b) a seasoned chamber. Auger depth profiling allowed the comparison of surface vs. bulk chemical information and (c) revealed a high oxygen content in the bulk of the film deposited in the seasoned chamber as compared to the film deposited under clean conditions. (d) The FOM showed that the film deposited in the seasoned chamber was plasmonic over a much shorter wavelength range, and it did not exhibit strong plasmonic properties as compared to its clean chamber counterpart.

After a regular cleaning and repair of the PEALD (in which all previously deposited film was removed from the deposition chamber, gas and precursor inlets, load lock input, and the ceramic plasma tube), many titanium nitride films were deposited including the same 300 cycle film (Recipe 1) discussed in Figure 5.2 and Section 5.2, which was analyzed with AES. Because the first 1-2 nm of the titanium nitride surface is partially oxidized in open air, an argon ion gun was used to sputter away the films surface to

allow for measurement of the bulk properties (Figure 5.4a). After sputtering for 240-360 s, the interior of the film was reached and showed still small concentrations of two contaminants: carbon (from the precursor ligands) and oxygen (residual in gas form, not removed from chamber by the turbo pump). The same analysis was performed on a 300 cycle film (also Recipe 1 deposited on 250 nm thermal silica on a silicon wafer) that was deposited in a seasoned chamber (which included many previous oxide depositions) from before the cleaning (Figure 5.4b), and a comparison of the two films (Figure 5.4c) showed that the film deposited in a chamber seasoned with oxide materials suffered from increased oxygen contamination. The increased oxygen content was likely responsible for the reduced FOM and wavelength range over which the film was plasmonic (Figure 5.4d). Additional film properties, including sheet resistance as measured by four-point probe (FPP), are included in Table 3 and demonstrate the increased resistivity caused by the oxygen present in the film, which directly effects the Drude parameter and the optical properties observed with spectroscopic ellipsometry.

	Clean Chamber	**Seasoned Chamber**
Thickness (nm)	27.3	21.9
Sheet resistance ($\Omega/\square$)	125	250
Resistivity ($\mu\Omega$cm)	341	547

Table 5.3: **Material parameters under different chamber conditions.** Comparison of thickness (spectroscopic ellipsometry) and electrical properties (FPP) for films deposited in clean and seasoned chambers.

The likely source of the oxygen is cross-contamination from metal oxide ALD films grown in the same tool, which could include AlOx, SiOx, TiOx, HfOx, CoOx, WoOx, and MoOx. The latter three oxides are known to be volatile and are likely to break down when exposed to the hydrogen plasma in the titanium nitride process, creating two problems: 1. Oxygen from previously deposited films will be reintroduced into the deposition chamber with the hydrogen radicals in the form of water and then redeposited into the titanium nitride film and 2. Residual metal (Co, W, Mo) remain as a conductive coating (in addition to the conductive titanium nitride coating) inside the plasma tube, potentially degrading the inductively coupled plasma source. Deposition

was also observed inside the plasma tube, providing an oxygen source in the region of the remote plasma. These results demonstrate the importance of keeping the nitride films and oxide films in separate deposition systems.

5.4 Grating Fabrication and Characterization

As a stepping stone to future three-dimensional lithography of plasmonic structures with PEALD titanium nitride, two-dimensional grating structures were fabricated from a ∼150 nm titanium nitride film (Recipe 2 deposited on fused silica in a seasoned chamber) using electron beam lithography with HSQ resist which, after exposure, forms a silica-like layer. A low power chlorine plasma etch (Oxford PlasmalabSystem100) was found to etch the titanium nitride with 10:1 selectivity over the silica substrate and mask and was used to pattern the titanium nitride gratings. The etch conditions were: Cl_2 flow rate: 30 sccm, 5 mTorr, 20 C; RF forward power: 30 W, DC bias 76 V; inductively coupled plasma forward power: 2000 W; etch rate ∼7 nm/s.[108] The scanning electron micrograph of a 900 nm period grating revealed straight side walls (Figure 5.5a), and the top view (Figure 5.5b) showed that the grating lines had the desired width of ∼300 nm.

Titanium nitride gratings with five different periods were fabricated and measured optically with dark field scattering spectroscopy, which showed specific signatures in their spectra dependent on their periods (Figure 5.5c,d). Two spectrometer grating positions were used to capture the full spectra. The 900 nm grating was also modeled with Lumerical (Figure 5.5e,f) where the SE data for that films deposition was included in the model as the refractive index for the titanium nitride material. Modeling results show reasonable agreement with peaks and troughs in similar locations as the measured grating, which demonstrates the accuracy of the models used for the ellipsometry data and the ability to easily pattern the plasmonic titanium nitride.

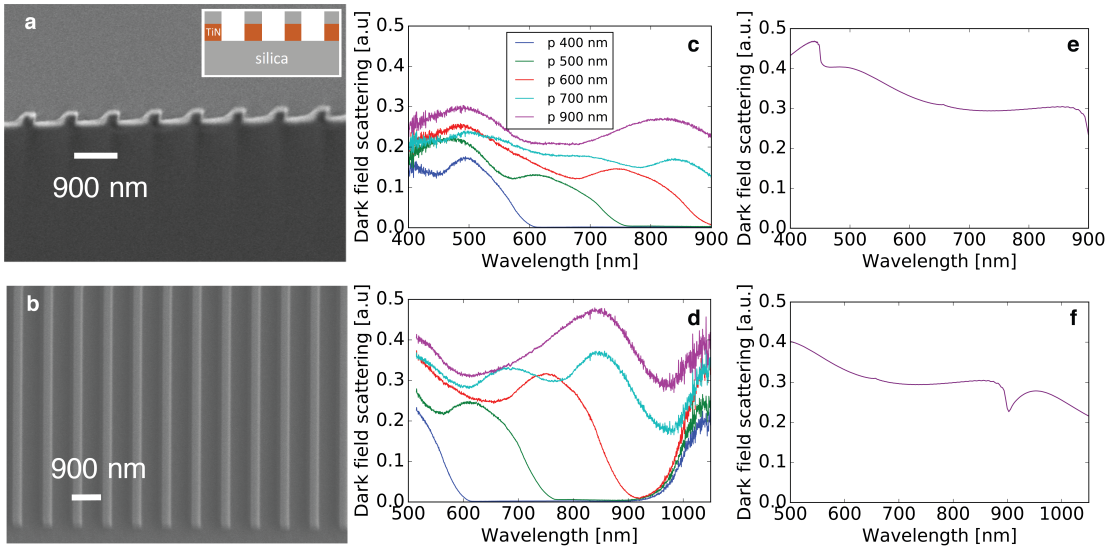

Figure 5.5: **Fabrication of titanium nitride gratings.** Reliable PEALD deposition is dependent on the chamber conditions, especially the plasma tubes cleanliness. Two comparable film chemistries yielded strikingly different results when deposited in (a) a clean vs. (b) a seasoned chamber. Auger depth profiling allowed the comparison of surface vs. bulk chemical information and (c) revealed a high oxygen content in the bulk of the film deposited in the seasoned chamber as compared to the film deposited under clean conditions. (d) The FOM showed that the film deposited in the seasoned chamber was plasmonic over a much shorter wavelength range, and it did not exhibit strong plasmonic properties as compared to its clean chamber counterpart.

In conclusion, we have demonstrated PEALD of titanium nitride and analyzed its optical, electrical, and chemical properties with SE, FPP, and AES. We have discussed important parameters for attaining consistent, high-quality films and the sensitivity of the deposited titanium nitride to oxide cross-contamination resulting from previously performed oxide depositions. Finally, we demonstrated ease of patterning of the titanium nitride film with a chlorine plasma etch process and verified the performance of a 900 nm period plasmonic grating using optical measurements and theoretical modeling.

Chapter 6

Chemistry of Atomic Layer Deposited Titanium Nitride

Use of atomic layer deposited titanium nitride industrially for plasmonic applications requires thorough understanding of material properties' dependence on deposition parameters as well as the resulting films' behavior in a variety of conditions and atmospheres. In the previous chapter, deposition chemistry of PEALD titanium nitride was thoroughly discussed including necessary processing steps for stable, consistent, and reliable material deposition. The next step in understanding PEALD titanium nitride films involved investigating its properties in post-deposition conditions that may relate to conditions experienced in end applications or post-processing possibilities that can yield more useful material properties. For example, the polystyrene beads used as a photonic crystal substrate in Chapter 7 are temperature sensitive and cannot be exposed to direct titanium nitride deposition at 300°C. Rather, as-deposited film properties should be explored for a variety of deposition temperatures motivated by the possibility of finding post-processing conditions that generate equal or superior quality titanium nitride that was originally deposited at substrate compatible lower temperatures (<100°C). Synthetic metal materials of higher plasmonic quality and conductivity are possible using annealing and may be useful for some applications.[109] While higher temperature annealing during *fabrication* is not ideal for all applications, devices designed to *operate* at higher temperatures such as HAMR heads or some photonic crystal devices, including

those used for solar thermophotovoltaics, would benefit from well-understood material behavior and optical quality.[46]

6.1 As-deposited Material Properties

To study the chemistry of PEALD titanium nitride, 300-cycle depositions were performed at different temperatures (40°C, 90°C – both using Recipe 1b in Table A.1, 180°C, 200°C, 300°C – using Recipe 1a in Table A.1) using Recipe 1 as in Table 5.1 (and Recipes 1a,b in Table A.3) yielding different thicknesses, conductivities, plasmonic properties, compositions, and crystallinities.[110] Figure 6.1a shows a linear increase in the thickness and therefore the deposition rate (in Å/cycle) with increasing deposition (substrate) temperature.[111] Columnar grains ∼10 nm in size were observed using scanning electron microscopy (Figure 6.1b) of a material resulting from a similar deposition recipe (Recipe 3 in Table A.3).

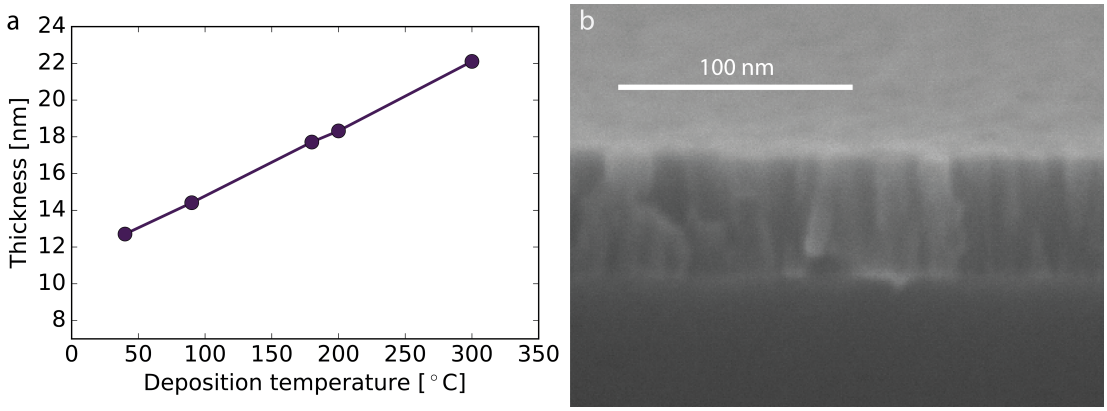

Figure 6.1: **Thickness vs. deposition temperature.** (a) 300 cycles of PEALD titanium nitride were deposited temperatures ranging between 40-300°C and resulted in increasing film thicknesses and deposition rates with increasing temperature. (b) 800 cycles of titanium nitride deposited on a flat surface (thermal silica) at 300°C has columnar grains ∼10 nm in size.

As previously discussed in 5.2, the dielectric function and plasmonic figure of merit (FOM) are dependent on film thickness with thinner films having lower FOMs. Additionally, comparing the 12 and 24 nm films in Figure 5.3 (deposited at 300°C) with the 40°C deposited 12 nm film's dielectric function (Figure 6.2), it can be seen that

the films deposited at lower temperatures are not plasmonic ($\epsilon'_m \geq 0$). Variable angle spectroscopic ellipsometry (VASE) together with a Drude-Lorentz model to fit the titanium nitride dielectric function as described in 5.2 were used to measure the optical properties of the titanium nitride.

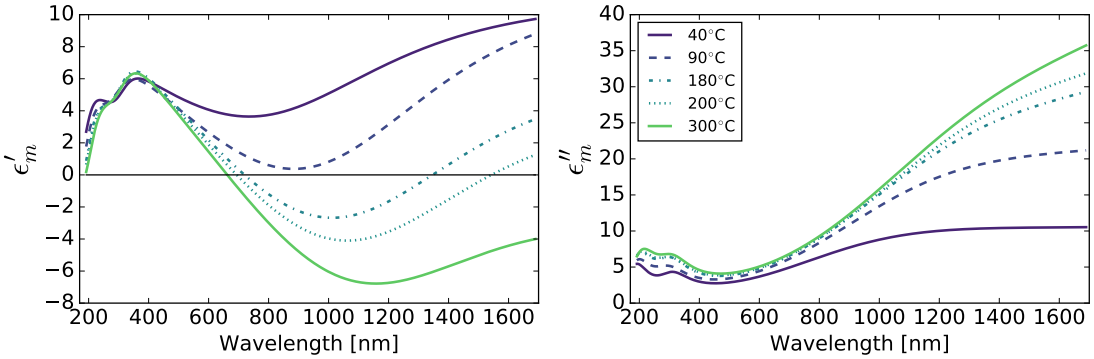

Figure 6.2: **Dielectric function vs. deposition temperature.** Titanium nitride's dielectric function is dependent on both its thickness (Figure 5.3) as well as its deposition temperature, with thicker films deposited at higher temperatures having stronger plasmonic quality. The corresponding FOM plot is included in Figure 6.8.

6.2 Material Properties of Annealed Films

To further understand the differences in the as-deposited materials, improve their plasmonic properties, and investigate potential for high quality films originating from lower temperature (<100°C) depositions, the films were annealed at several temperatures between 500°C and 1100°C. Their thicknesses and plasmonic FOMs were determined using VASE, and film conductivity was measured using the Hall effect as well as VASE. Anneals were performed in a glass tube furnace pumped and purged with argon (twice) before flowing 250 sccm Ar and 20 sccm H_2 through the tube (see Appendix A.5). The furnace temperature was ramped from room temperature (∼20°C) to the annealing temperature as fast as possible (∼10s of minutes), held constant for one hour, and then lowered. The hydrogen gas flow was stopped only once the samples were cool enough to remove from the furnace (≤80-100°C). The hydrogen flow was continued during the cooling stage to prevent possible film oxidation, which has been shown in titanium nitride films annealed at temperatures ≥150-200°C in atmospheres containing oxygen (or

an oxygen leak).[112,113] Full or partial film oxidation (beyond the native oxide of 1-2 nm) of the as-deposited titanium nitride when annealed in air between 200-500°C was also observed but is not plotted.

6.2.1 Film Thickness and Conductivity

Sample annealing in the reducing hydrogen atmosphere was found to cause a reduction in film thickness (Figure 6.3a) and an increase in conductivity (Figure 6.3b). These effects were presumably caused by the removal of impurities such as carbon and oxygen as well as the formation of larger grains and the increase crystalline order within the sample (as opposed to remaining nanocrystalline or amorphous) and increased film density.[114,115] According to Figure 6.3, the films deposited at 90°C and 300°C have equal conductivity after annealing at 1100°C even though the 90°C-deposited film is barely more than half of the 300°C-deposited film thickness.

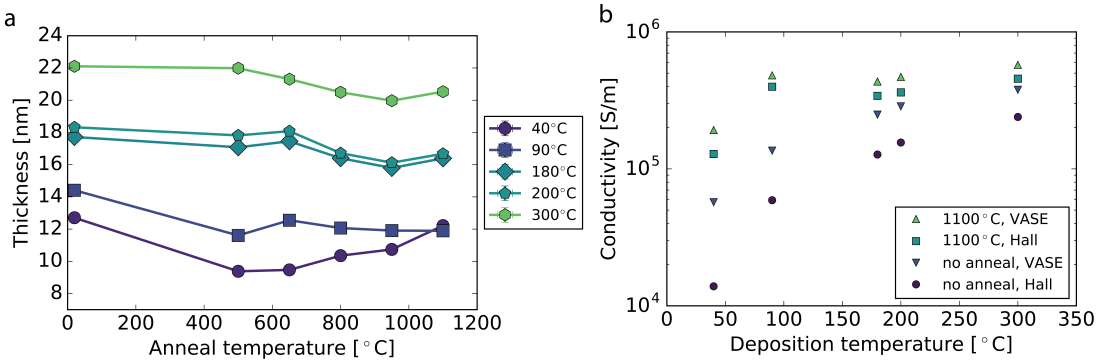

Figure 6.3: **Film properties vs. annealing temperature.** (a) A decrease in film thickness and (b) an increase in film conductivity were observed as a result of annealing.

The conductivities calculated from the VASE measurements using the equation:

$$\sigma = \mu N_e e \tag{6.1}$$

where σ is the DC conductivity of the material. It should be noted that the conductivities measured with SE (an optical technique) are consistently higher than measurements performed with complementary electrical techniques such as four-point probe and the Hall effect (as was used in this case, Ecopia HMS-5000). This is due to the effect of

grain boundary scattering reducing the electrically measured conductivities. This effect becomes more dominant for thinner films.[32]

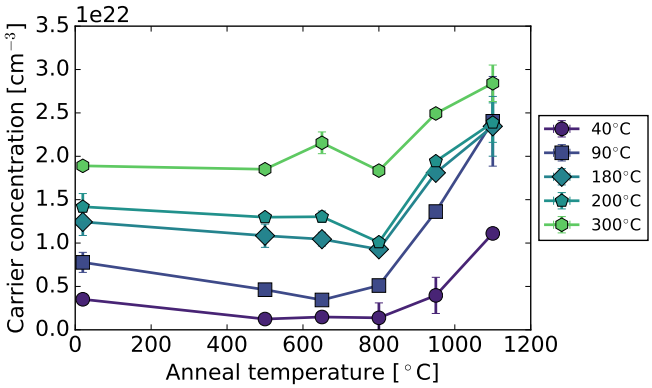

Figure 6.4: **Carrier concentration of annealed films.**

The SE measurements also showed the high temperature (950°C and 1100°C) annealed titanium nitride to have larger carrier concentrations matching expectations from literature.[116] These higher conductivities and larger carrier concentrations relate directly to the plasmonic properties through the Drude parameter and will result in shifting of the dielectric function and plasmonic FOM.

6.2.2 Film Plasmonic FOM

Annealed films' optical properties were observed using VASE, and their FOMs were calculated from the Drude-Lorentz extracted pseudo transformed dielectric function. Key observations include the slight degradation in FOM for films annealed at 500°C (Figures 6.5 and 6.8), of which the cause has not yet been determined. In addition, the 950°C anneal yielded the films with the overall largest plasmonic FOM (Figure 6.5); however, anneals at 1100°C were still capable of further blue shifting the wavelength location of the maximum FOM and the plasmonic transition wavelength, λ_p (Figure 6.7).

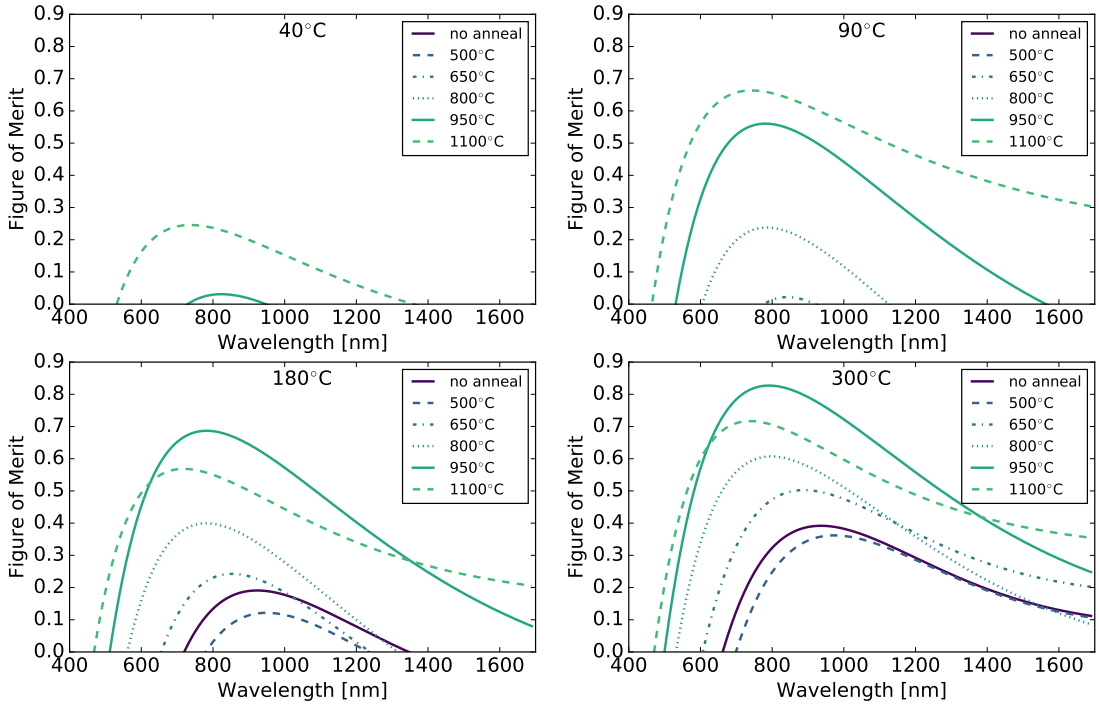

Figure 6.5: **Figure of merit of annealed samples.** Films deposited at 40°C, 90°C, 180°C, and 300°C can be observed as it evolves from each anneal. (The deposition at 200°C was left off because of its similarity with the deposition at 180°C.)

One notable observation from the FOMs presented in Figure 6.5 is the different decay trend present in the near infrared for anneals at 800°C and 950°C. In this wavelength region, the titanium nitride's plasmonic quality diminished more quickly and in some cases (*e.g.* 180°C deposited sample) the film annealed at 800°C ceases to be plasmonic (FOM < 0) at lower wavelengths than even the as-deposited version. The dominant contributor to this trend should be the third and final Lorentz oscillator near 1 eV, which was added to the Drude-Lorentz model in order to fit the near infrared region of the measured spectrum. Based on previous literature, this oscillator is due to the $\Gamma'_{25} \rightarrow \Gamma_{12}$ interband transition.[35,117]

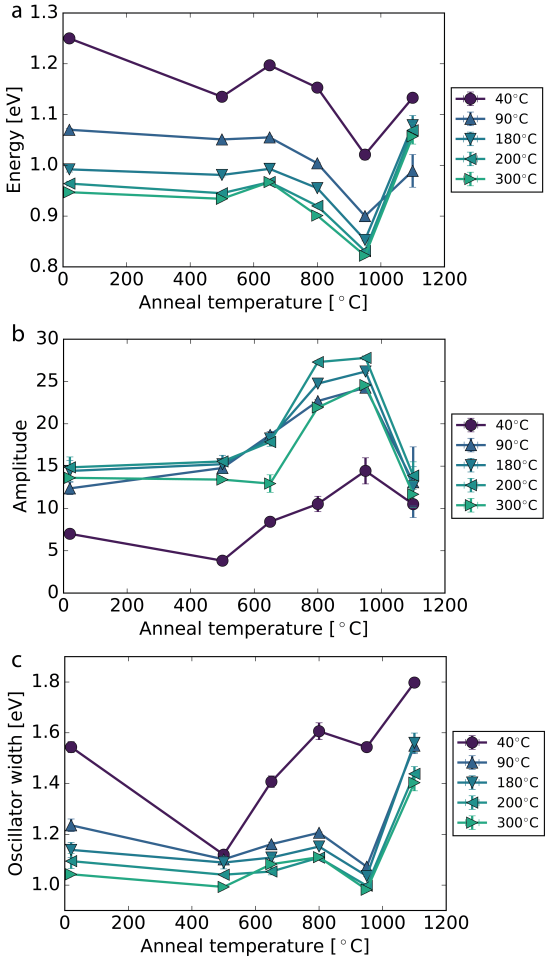

Figure 6.6: **Oscillator fit parameters vs. anneal temperature.** The lowest energy Lorentz oscillator added to the SE model is usually located ∼1 eV, but its exact properties shift with annealing temperature. The (a) oscillator energy, (b) amplitude (dimensionless), and (c) oscillator width can describe the varying optical properties in the near infrared dependent on anneal temperature.

Viewing the ∼1 eV oscillator's parameters in Figure 6.6 aid in understanding the titanium nitride films' behavior in the near infrared with annealing. First, for anneals at 800°C and 950°C the energy position of the oscillator shifts to lower values. Second, the amplitude of this interband transition significantly increases ($\gtrsim$50%) as compared to films annealed at other temperatures. Finally, the oscillator width does not appear to show a significant change. Since the red shifting of the oscillator should move its effects

further outside (or to the edge of) the SE measurement window, it can be inferred that the increased oscillator amplitude is likely the cause of the reduced plasmonic behavior in this region. Anneals at at 800°C and 950°C may generate an alternate crystalline structure with shifted and stronger resonant properties, although exactly what that is has yet to be determined.

Another observation from the FOMs presented in Figure 6.5 is the blue shifting (and general improvement) of the plasmonic properties with annealing temperature. Both the plasmonic transition wavelength (λ_p) and the wavelength of maximum FOM (λ_{maxFOM}) are shown in Figure 6.7. With increasing anneal temperature, λ_p appears to converge near 465-470 nm regardless of deposition temperature. λ_{maxFOM} is also rather independent of deposition temperature.

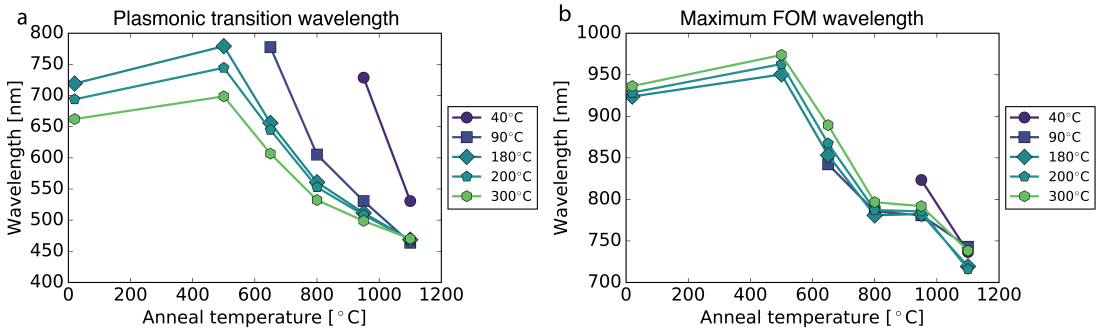

Figure 6.7: **Plasmonic properties vs. annealing temperature.** (a) As the films are annealed at higher temperatures, the wavelength at which they become plasmonic both blue shifts begins to converge near 465-470 nm. (b) The peak plasmonic behavior (maximum FOM) also blue shifts from the near infrared into the visible.

Finally, when annealed at 1100°C, the film deposited at 90°C obtained a plasmonic FOM and conductivity comparable to that of the 300°C deposited film annealed under the same conditions (Figures 6.3 and 6.8, 1100°C), and even skipped over the 180°C and 200°C deposited films' FOMs. As mentioned previously, this behavior is surprising since the 90°C deposited film is significantly thinner than the 300°C deposited film. To understand this behavior, chemical composition analysis and grain size measurements must be performed.

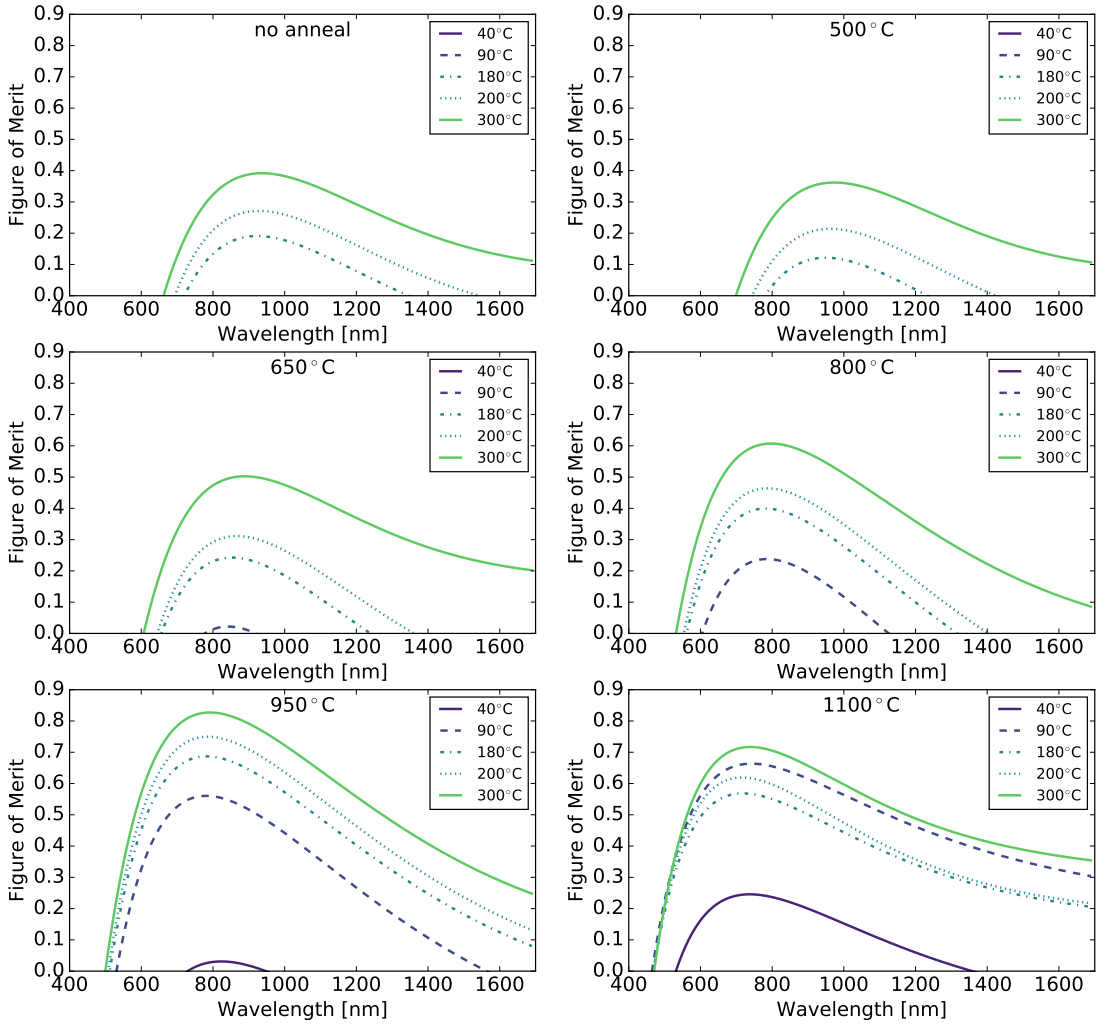

Figure 6.8: **Figure of merit of annealed samples.** Annealing generally improves the plasmonic quality of the titanium nitride films. Surprisingly when annealed at 1100°C, the film deposited at 90°C exceeds the plasmonic quality of the films deposited at 180°C and 200°C and approaches the quality of the film deposited at 300°C even though it is significantly thinner (Figure 6.3a).

6.2.3 Film Composition

Auger electron spectroscopy was used to investigate the contamination of oxygen and carbon in the titanium nitride bulk material (reached using argon ion sputtering) both before and after annealing for multiple deposition temperature. The anneals containing

hydrogen were successful at removing much of the carbon from the titanium nitride film, which accounts for some of the improvement in material properties (carbon prevents crystallization[110]); however, more effects are present. It was observed that for the films annealed at 1100°C, the 90°C deposited film contained more contaminants than the 300°C deposited film, and therefore the reduced contamination does not account for why the 90°C deposited film sees significantly more improvement when annealed at 1100° compared to the other samples under the same annealing condition.

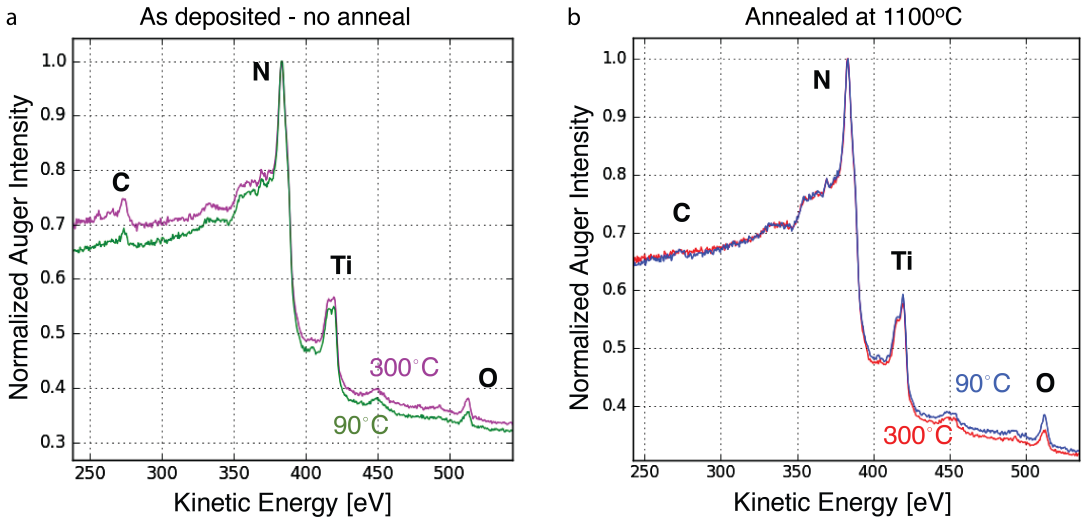

Figure 6.9: **Bulk contamination of annealed films.** Auger electron spectroscopy of samples deposited at 90°C and 300°C (a) before and (b) after annealing at 1100°C reveal that the impurities are more easily removed from the 300°C deposited sample, and the post-annealing and high FOM 90°C sample has more remaining contamination.

Another observation from Figure 6.9 includes the change in relative titanium to nitrogen content in the film as evidenced by the shape of the titanium (and nitrogen) peak at ~420 eV. The as-deposited films in Figure 6.9a appear to be over-stoichiometric or nitrogen rich (TiN_x where x>1), but the films annealed at 1100°C are now titanium rich (x~0.67) and possibly due to either a new stoichiometry (Ti_3N_2 titanium(II)nitride), nitrogen vacancies in the lattice, or selective sputtering of the lighter nitrogen element by the argon ion gun used for obtaining measurements of the bulk film.[118] Previous work on PEALD titanium nitride with TDMAT showed high contamination levels for

thermally enhanced processes (no plasma, 37% oxygen and 9% carbon) and contamination below 6% for optimized plasma-enhanced processes, which we believe to be the case for the 300°C-deposited film in this work.[111]

Since the presence of contaminants oxygen and carbon cannot account for the 90°C deposited film's exceptional plasmonic FOM and conductivity after annealing at 1100°, it is believed that the grain size may account for the improved properties. In this case, a more amorphous as-deposited material would allow for easier atom mobility and rearrangement during high-temperature annealing than the larger ∼10 nm grains present in the 300°C-deposited film. To measure the grain size, x-ray diffraction was unsuccessfully attempted (films were too thin). Transmission electron microscopy (TEM) measurements are currently underway.

In conclusion, we have explored the properties of titanium nitride films under different PEALD conditions as well as the effects of post-processing conditions on their electrical, optical, chemical, and physical properties. While TEM results are still outstanding, we can conclude that the higher quality plasmonic films deposited at lower temperatures (<100°C) are possible through post-processing anneals in reducing atmospheres. Further application their uses will be discussed in Chapter 7.

Chapter 7

Towards Plasmonic and Conductive Photonics in Three Dimensions

Photonic crystals are periodic nanostructured materials with optical badgaps which can prohibit certain wavelengths regions of light from propagating through the crystal.[119,120] The most promising applications for photonic crystals and photonic bandgaps lies in the visible and near infrared frequencies.[121] Optoelectronic applications include microlasers, light emitting diodes, and telecommunications[121] as well as electrically tunable color films or photovoltaics (both as emitters), which both require the photonic crystal to be electrically conductive.[122] Creating electrically conductive photonic crystals is rather difficult since metals are hard to nanostructure in two dimensions, and obtaining a variety of designed and precise periodic structures in three dimensions is nearly impossible with metals. In order to obtain conductive photonic crystals, previous researchers have resorted to forming nanocomposites of polymers with carbon nanotubes, which is nontrivial.[122] The other leading obstacle for producing and realizing the potential of photonic crystals is the inexpensive and reliable three-dimensional fabrication of these structures with appropriate optical properties, which often include plasmonic materials.[121,123] Atomic layer deposition (ALD) has been demonstrated as a high-throughput and inexpensive technique capable of fabricating photonic crystals with a diverse variety

of materials including oxides,[124,125] and transparent conducting oxides,[126] nitrides,[127] and sulfides.[128] In addition, plasma enhanced atomic layer deposition (PEALD) has been demonstrated for high aspect ratio conformal coatings over complex geometries while simultaneously providing better quality material and is therefore ideal for the three-dimensional fabrication of photonic crystals.[58,105] Furthermore, the deposition of conductive and plasmonic materials such as titanium nitride may enable the required quality of photonic crystals through the use of silver or other plasmonic metals.[129,130] This chapter presents work towards conductive and plasmonic photonics in three dimensions using conformal coatings of PEALD titanium nitride on silica inverse opals.

7.1 Titanium Nitride Properties

The conductive and plasmonic titanium nitride films used in this work were deposited using PEALD with a two stage plasma as described in Recipe 1a in Appendix A.1.[31] Various thicknesses of titanium nitride ranging between 2 and 50 nm were used in order observe the photonic crystal properties with films varying in optical (Figure 7.1a-b) and electronic (Figure 7.1c) properties with different compound effects when many layers are encountered by light interacting with the photonic crystal. The measurements in Figure 7.1 were performed on flat films deposited onto silicon substrates with 250 nm of thermal silica during the same deposition as each corresponding inverse opal sample. It should be noted that even the 2 nm film exhibited high electrical conductivity (using the Hall effect) even after any oxidation could have occurred.[32,33] The conductivity calculations from SE were calculated using Equation 6.1.

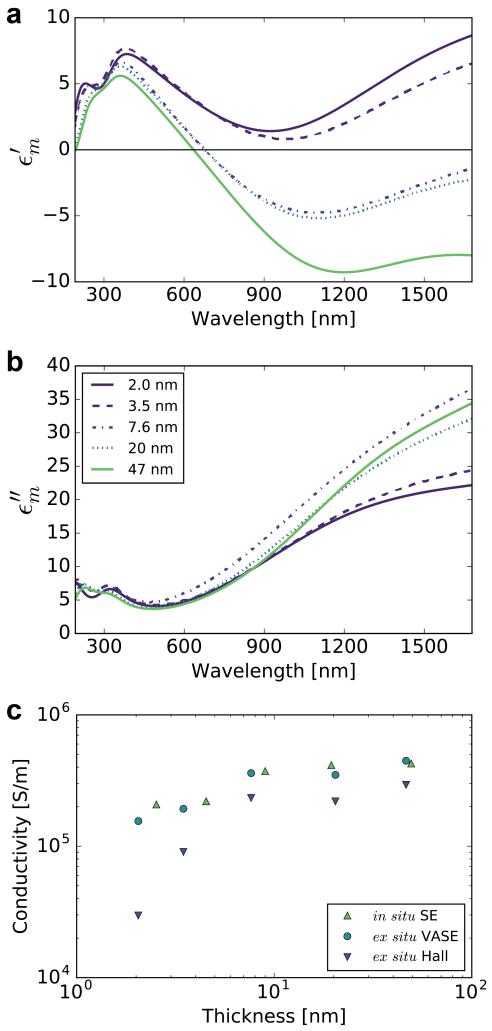

Figure 7.1: **Dielectric function and conductivity.** Optical and electronic properties of titanium nitride thin films used for inverse opals. The real (a) and imaginary (b) parts of the dielectric function as fit by *ex situ* variable angle spectroscopic ellipsometry. (c) Spectroscopic ellipsometry was also used to measure the film thickness and conductivity in the as-deposited films (measured *in situ* during deposition) and films measured after deposition and exposure to air. These optical measurements of conductivity are compared to electrical transport measurements performed using the Hall effect.

In situ spectroscopic ellipsometry (SE) was performed during film deposition, and variable angle SE (VASE, J. A. Woollam) at angles between 45° and 75° in 5° increments were performed *ex situ* after deposition was complete and the native oxide layer had

grown (1-2 nm). Both data sets were fit using a Drude-Lorentz model with one Drude and three Lorentz oscillators as described in Chapter 5.2.[31] The model used to fit the VASE measurements also included a titania oxide layer on the surface, and as a result of surface oxidation, the titanium nitride was usually measured to be thinner than shown by the *in situ* measurements. The one exception is the ∼20 nm sample, which appears to be of lower quality and therefore was more difficult to fit with same parameters as the higher quality samples. In addition, while the thinnest two films had small plasmonic windows between $\sim \lambda_1$ and λ_2 as measured *in situ*, this plasmonic quality was no longer evident in the VASE measurements (Figure 7.1a) presumably due to the reduced thickness from the native oxide growth as well as possible oxidation between the nanocrystalline grain boundaries.[110]

7.2 Inverse Opal Fabrication

The inverse opal fabrication begins with 390 nm diameter polystyrene (PS) beads evaporated onto a quartz substrate as described in Appendix A.6.[131] The deposition of titanium nitride for inverse opals is restricted by the thermal stability of the beads used as the opal template. The PS beads have a glass transition temperature at ∼100°C limiting process parameters for material deposition. Titanium nitride can be successfully deposited onto the beads directly at 90°C (which was demonstrated); however, the titanium nitride is most conductive and plasmonic when deposited at higher temperatures. For this reason, we chose to first create an inverse opal skeleton with silica (10 nm) deposited using PEALD at a lower temperature of 40°C (Figure 7.2a). This sample was then baked in air at 650°C for 30 minutes to remove the PS beads. Optical measurements of the silica inverse opals were performed before conformally coating them with titanium nitride at 300°C yielding an inverse opal photonic crystal coated with a conductive and plasmonic layer of titanium nitride. Scanning electron microscopy (SEM) was used to look at cross sectioned photonic crystal sample of silica inverse opals coated with 47 nm of titanium nitride. Figure 7.2b shows the uniform coating of titanium nitride on the silica lattice as well as the cavities where the polystyrene beads defined the lattice shape. In addition, the nanoporosity of the lattice openings where the beads formerly touched can also be seen. This SEM image was recorded after the annealing

experiments discussed in Chapter 7.5 were performed indicating that the inverse opal structure was able to withstand high temperatures.

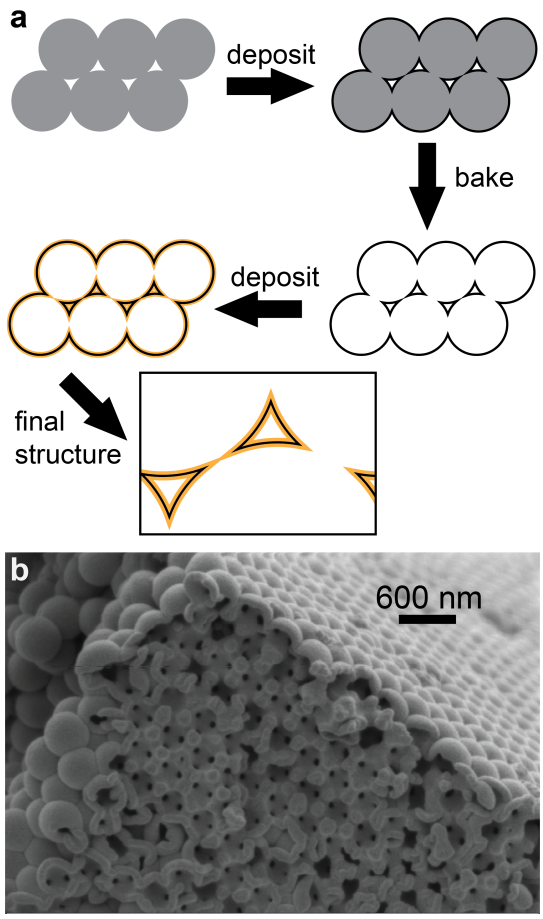

Figure 7.2: **Inverse opal fabrication.** Fabrication of titanium nitride plasmonic and conductive inverse opals (photonic crystal). (a) Polystyrene beads in solution were evaporated onto a quartz slide and allowed to dry. These opals were coated with atomic layer deposited silica and then removed via annealing. The left behind silica inverse opal was then coated with titanium nitride. (b) A scanning electron micrograph of an inverse opal coated with 47 nm of titanium nitride shows the complex, periodic, and high surface area of the conductive inverse opal lattice. It should be noted that this image was taken *after* the anneals discussed in the following section.

7.3 Photonic Crystal Reflected Intensity

To observe the photonic effects of the titanium nitride coated onto the silica inverse opals, reflected intensity measurements were performed with VASE from ∼190-1690 nm or 0.73 to 6.9 eV. The photonic crystals were measured at angles ranging from 45° to 80° in 5° increments (Figures 7.3a,b). Measurements of the 10 nm silica inverse opal lattice (Figure 7.3a) were performed before adding the titanium nitride layer (Figure 7.3b). In addition, a slight red shift in the photonic resonance is evident in Figures 7.3c,d. The photonic crystal shows a distinct resonance that shifts with angle, and by applying a thin coating of titanium nitride, the photonic crystal becomes conductive only minimally compromising the photonic crystal's resonant reflected intensity. In order to further understand the optical effects of the titanium nitride on the silica inverse opal, annealing of the photonic crystals should be performed.

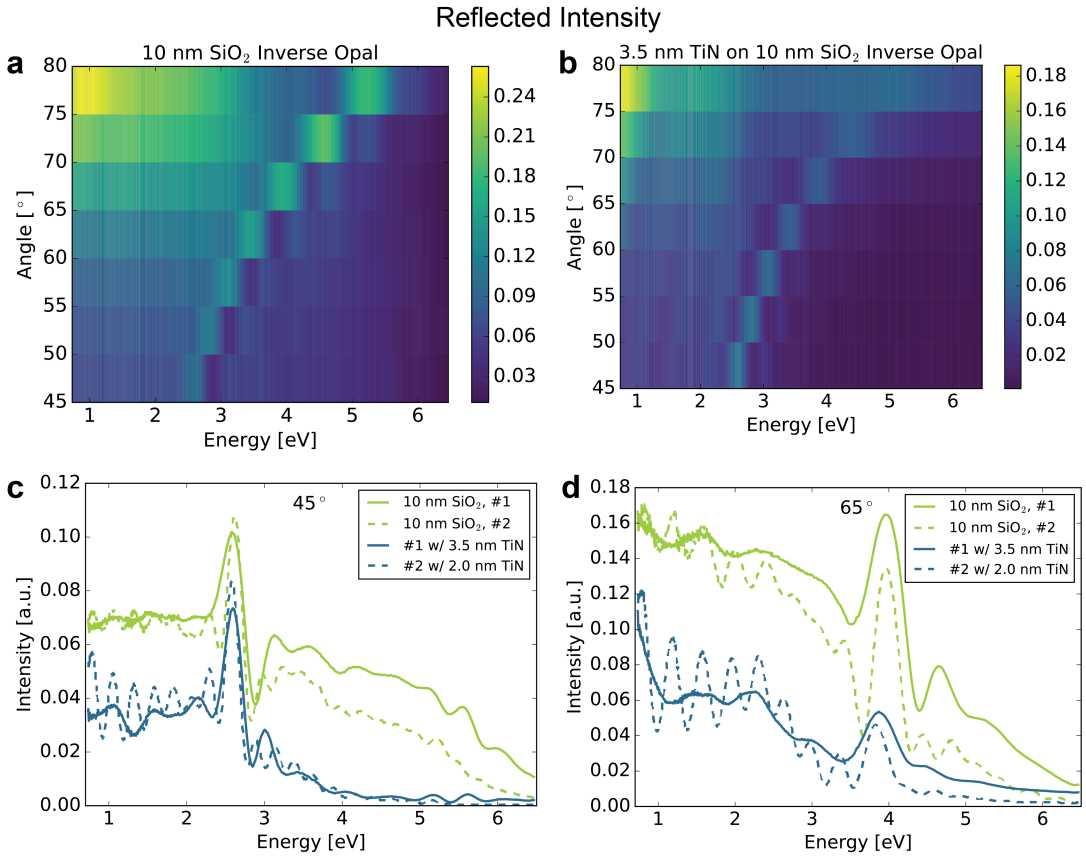

Figure 7.3: **Inverse opal reflected intensity.** Reflected intensity of inverse opals as measured by variable angle spectroscopic ellipsometry (VASE). (a) A strong photonic mode is present in the silica inverse opal, which only experience some attenuation when coated with 3.5 nm of conductive and refractory titanium nitride (b), which is more evident when comparing the reflected intensity of two inverse opal samples measured at (c) 45°. (d) A small red shift in photonic resonance after titanium nitride deposition is more evident when the crystal is measured at 65°.

7.4 Annealing Effects on Flat Films

The results presented in Chapter 6.2.2 show that the dielectric function of titanium nitride can be shifted depending on annealing temperature, which will change the resonant properties of the photonic crystal. Specifically, the plasmonic transition wavelength (λ_p, where $\epsilon'_m = 0$) of the titanium nitride shifts and may move in or out of resonance with

the photonic crystal as a result of annealing.

Prior to the fabrication of the ultrathin titanium nitride coated inverse opals discussed above in Figure 7.3, the inverse opals coated in thicker layers were measured optically, subjected to annealing, and measured again. These anneals and measurements were conducted along with flat films of titanium nitride from the same depositions in order to directly observe the dielectric function of the titanium nitride as a result of the anneal. Since the inverse opals were undergoing all annealing experiments, flat films were used that also experienced all of the anneals performed. To verify that annealing is additive and previous lower temperature anneals minimally affect a later anneal at a higher temperature, other flat film samples which only experienced one anneal were also used, and they showed good agreement with the films that experienced all anneals. The measurements plotted in Figures 7.4 - 7.7 were from the films that only experienced one anneal. Because annealing at 500°C was shown to decrease film quality, the inverse opals were not annealed at this temperature, and experiments began at 650°C.

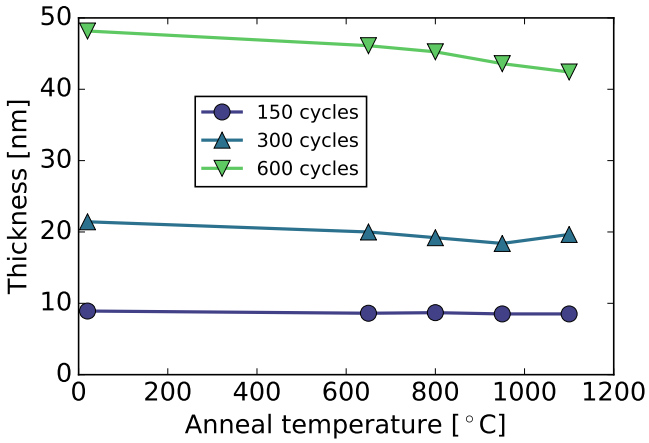

Figure 7.4: **Thickness change with anneal temperature.** Due to grain reordering and impurity removal, annealing of titanium nitride films causes a reduction in thickness. This thickness change was measured on flat films and is expected to affect the photonic crystal resonant behavior as well.

As was observed in the experiments in Chapter 6.2, annealing the titanium nitride films causes a reduction in film thickness due to reordering of grains and reduction of impurities. Referencing the thicknesses in Figure 7.4 will be useful for interpretation

of the following results, which are sometimes plotted against thickness and sometimes referred to as the "150-cycle" deposition wherever appropriate. In addition, the plasmonic quality of the films as determined by their FOMs were also observed to generally improve with annealing (Figures 7.5, 7.7).

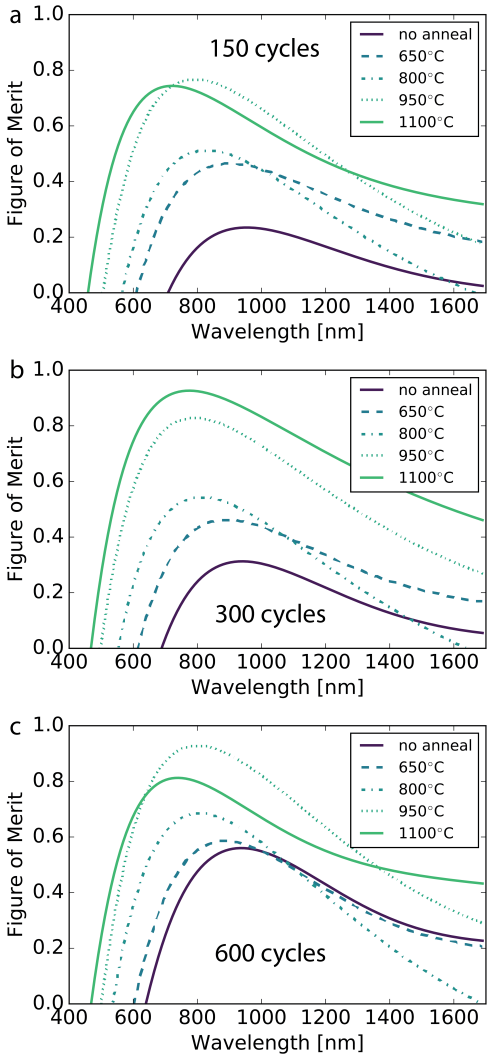

Figure 7.5: **Figures of merit vs. anneal temperature.** Annealing also causes a change in the plasmonic properties of the titanium nitride. The figures of merit (FOMs) for each anneal condition and film thickness (a) 150 cycles, (b) 300 cycles, and (c) 600 cycles demonstrate the evolution in film plasmonic quality in the visible and near infrared.

The same decay trend that was present in the near infrared for anneals at 800°C and 950°C in Figures 6.5, 6.6, and 7.6 is also present in the films annealed for the flat films annealed here (as expected), and some cease to be plasmonic (FOM < 0) near 1600 - 1700 nm (Figure 7.5). (Although this behavior was not as evident in Chapter 6.2.)

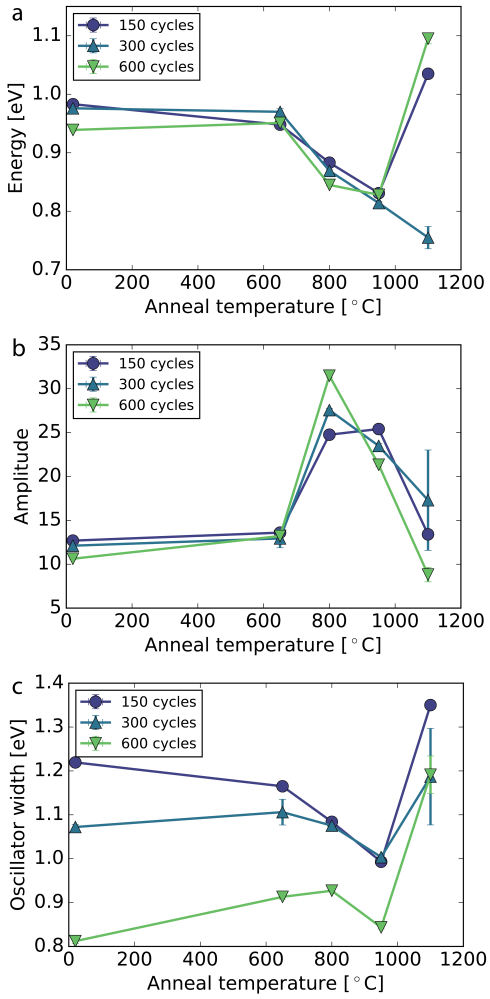

Figure 7.6: **Oscillator fit parameters vs. anneal temperature.** The lowest energy Lorentz oscillator added to the SE model is usually located ∼1 eV, but its exact properties shift with annealing temperature. The (a) oscillator energy, (b) amplitude (dimensionless), and (c) oscillator width can describe the varying optical properties in the near infrared dependent on anneal temperature and generally agree with the experiments presented in Figure 6.6.

Further inspection of the annealed films' FOMs in Figure 7.5 shows the expected blue shifting of the plasmonic transition wavelength (λ_p) and the location of the maximum FOM (λ_{FOMmax}), which are plotted in Figure 7.7.

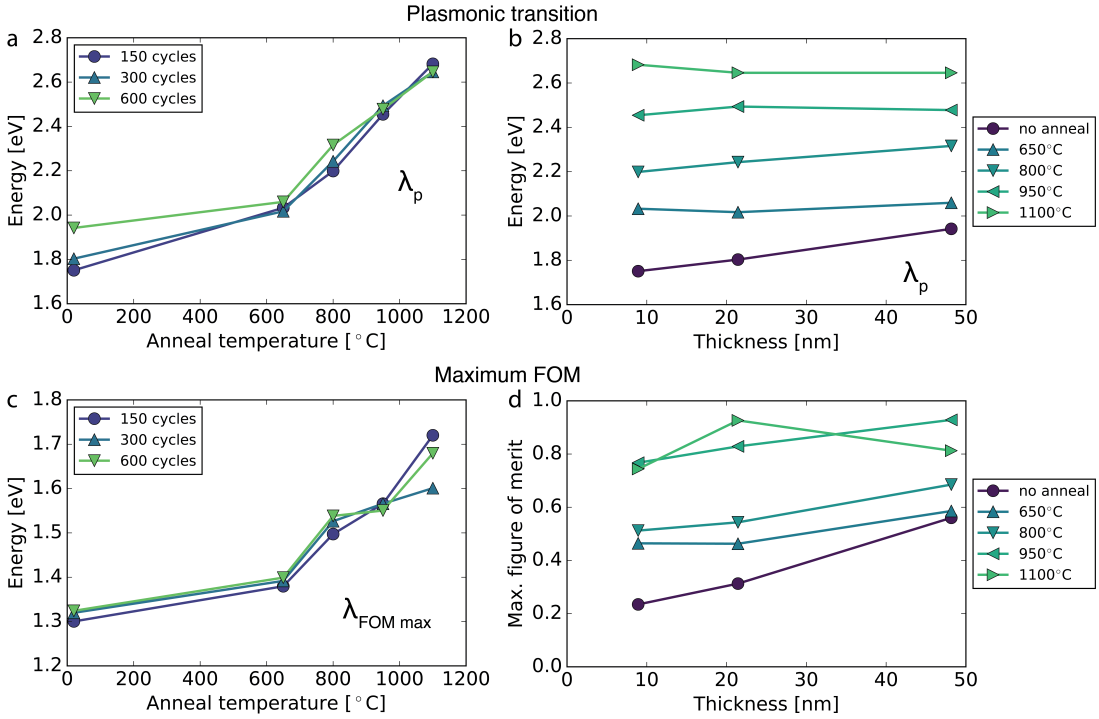

Figure 7.7: **Plasmonic properties vs. anneal temperature.** Extracting individual data points from the FOM plots is useful for understanding the plasmonic behavior of the films. (a,b) The plasmonic transition wavelength (λ_p) of the films blue shifts with increasing anneal temperature and after anneals shows less dependence on the film thickness in contrast to the as deposited samples. (c,d) The peak FOM also blue shifts with increasing annealing temperature. As was observed in Chapter 6.8, annealing up to 950°C causes an increase in the peak value of the FOM, which then decreases slightly after annealing at 1100°C. The one exception in this work is the 300-cycle sample, which is discussed further in Figure 7.8.

The 300-cycle sample annealed at 1100°C exhibits behavior different than expected based on previous anneals and measurements due to the timing of its deposition. (This film was first in the series to be deposited in the shared tool following oxides, and more cleaning or a titanium nitride predeposition or conditioning could have helped the quality.) This is evident in high FOM in Figure 7.5 and the low energy position of the

Lorentz oscillator in Figure 7.6a. When fitting the SE data, the software optimizes for a root mean square error (MSE), and is shown in Figure 7.8a for all samples. While most have acceptable MSE values of ∼6-14 nm, the MSE for the 300-cycle sample annealed at 1100°C was unable to be optimized with an MSE below 20. The main contributing factor this error is the carrier concentration (note the large error bar of 18% in Figure 7.8b), which determines the Drude parameter and is most evident in the ultraviolet. Figure 7.8c shows the SE fit of the raw measurement data where the fit is poorest below 400 nm.

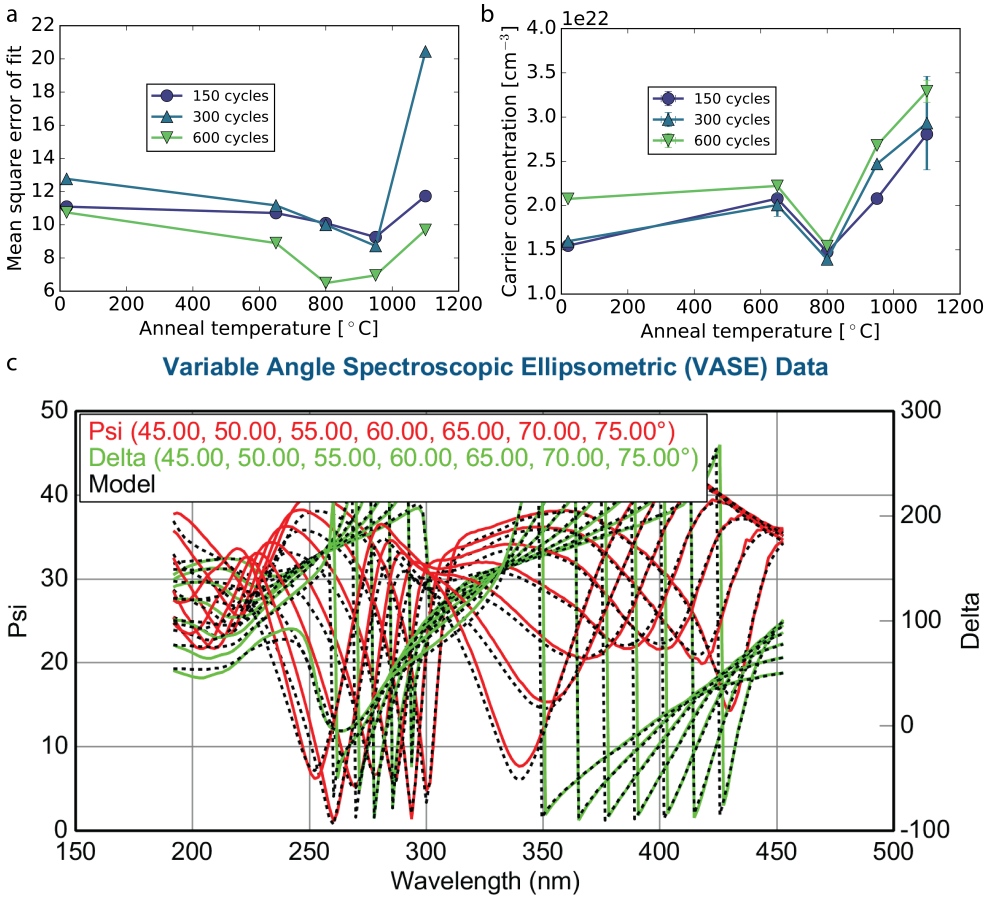

Figure 7.8: **Carrier concentration and ellipsometry fit.** (a) The fit quality of the spectroscopic ellipsometry measurements can be quantified by the root mean square error (MSE) of the fit. All samples exhibit a reasonably good MSE except the 300-cycle sample after annealing at 1100°C. (b) This high MSE is due to high error (18%) in the fitting of the carrier concentration of that sample. (c) For the spectral fits of this sample, the poor fit is reflected through a poor fit in the sub-400 nm wavelength region, or where the Drude parameter of the dielectric function is dominant.

7.5 Annealing Effects on Photonic Crystals

The characterization of the annealed *flat* titanium nitride films is foundational to the understanding of the behavior of the annealed titanium nitride coated silica inverse opals. Inverse opals coated with 150, 300, and 600 cycles of titanium nitride were

annealed simultaneously with their respective flat films and then measured with VASE. After each anneal (650°C, 800°C, 950°C, and 1100°C) their reflected intensities were recorded from 45°-80° in 5° increments. The anneals were performed with progressively increasing temperature. Due to the high reflectivity of the thicker titanium nitride, photonic resonances were weaker as less light is able to pass through or interact with the entire photonic crystal (due to absorption). Therefore, the reflected intensity of the 150-cycle sample normalized by a flat region on the quartz substrate (also coated with 10 nm of silica and 150 cycles of titanium nitride) is plotted in Figure 7.9. While the photonic crystal resonance is known to blue shift with increasing angle of incidence (Figure 7.3), a blue shift is also observed with increasing annealing temperature presumably due to the blue shifting of the plasmonic transition wavelength. In addition, photonic crystal theory predicts that the resonance should increase when the plasmonic transition wavelength ($\epsilon'_m = 0$) is resonant with the photonic crystal, which may be the cause of the increased photonic crystal reflected intensity for anneals at 650°C and 800°C.

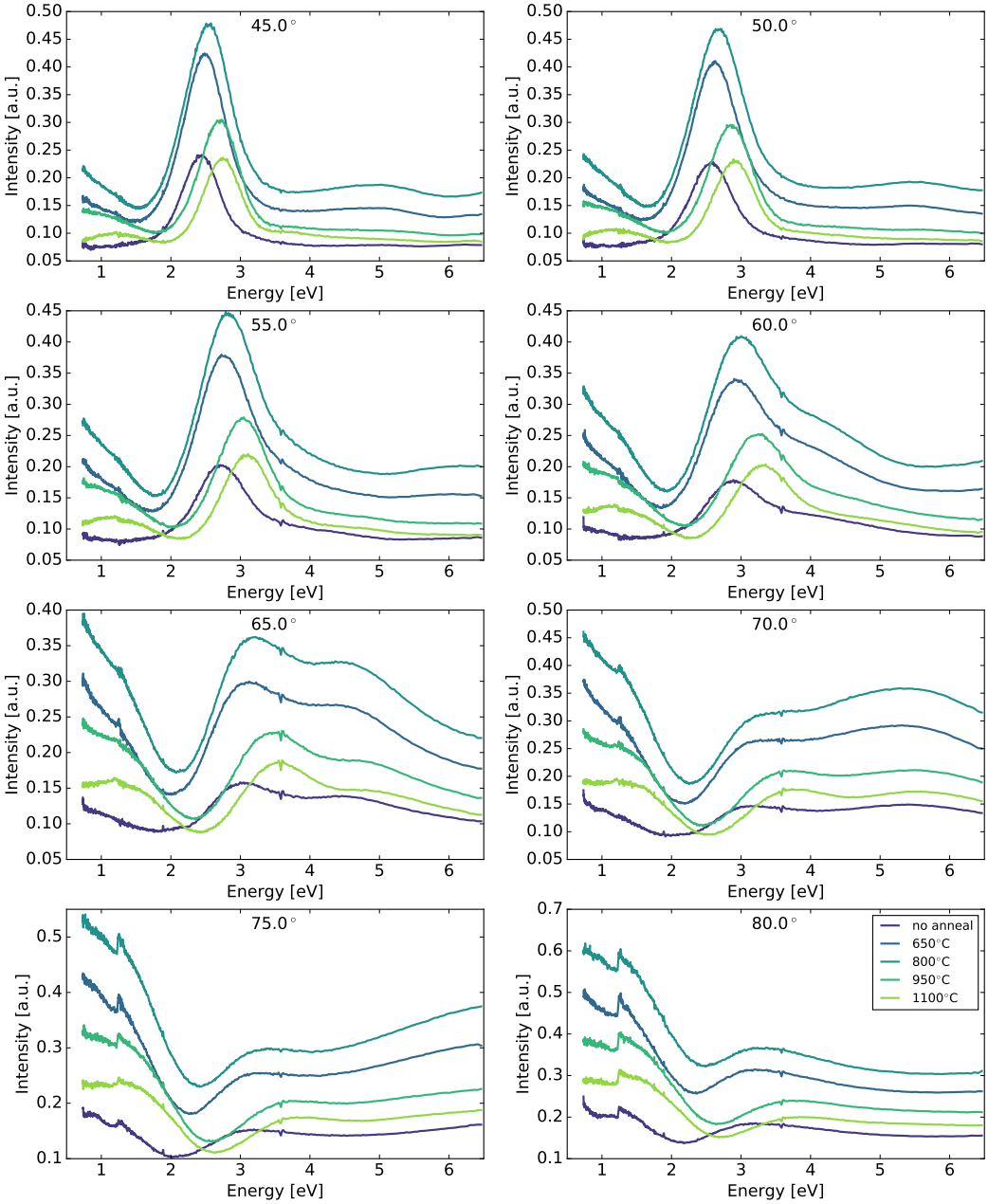

Figure 7.9: **Photonic crystal resonance shifts.** 150 cycles (7-10 nm) of titanium nitride was deposited onto a silica inverse opal lattice, measured with VASE at 8 angles (45°, 50°, 55°, 60°, 65°, 70°, 75°, 80°), annealed, measured, etc. It should be noted that this reflected intensity measurements from the inverse opals were normalized by the reflected intensity measured from a flat region of the sample. Annealing causes a blue shift in photonic crystal resonance, with the peak reflected intensity occurring after the 800°C anneal.

The photonic crystal resonance dependence on the annealing temperature can be quantified through extracting the energy locations of the resonance maximums for each anneal, which is plotted in Figure 7.10 for the 45° measurement. The blue shifting of the photonic resonance appears to "saturate" around 2.75 eV, which is reached when the film is annealed at 1100°C. For higher angle measurements, this peak becomes harder to discern since it merges with a second higher energy resonance.

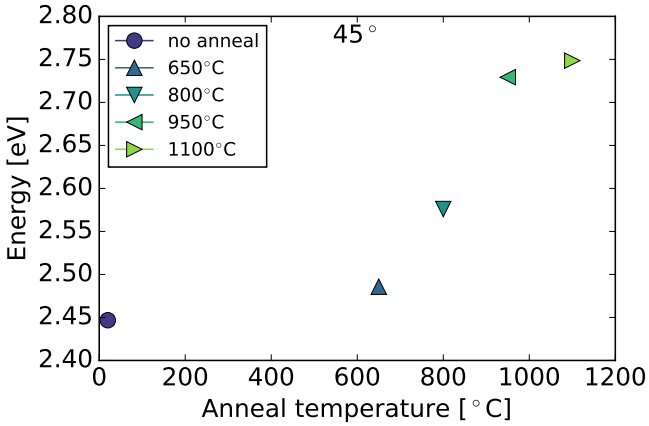

Figure 7.10: **Photonic crystal resonance shift vs. anneal temperature.** The location of the peak reflected intensity of the silica inverse opal coated with 150 cycles of titanium nitride blue shifts most notably after being annealed at 800°C and 950°C (measured at 45° after each anneal).

Finally, the angle dependence of the photonic crystal resonance for the most-resonant sample (annealed at 800°C) was followed and is plotted in Figure 7.11 with the resonance shifting about 0.5 eV over the 15° range. While there appears to be a rather linear trend in the resonance shift through this region, it should not be extrapolated to a 0° measurement angle. According to previous work on inverse opal photonic crystals with gold nanoparticles, the angle dependent measurements show the greatest blue shifting of the resonance with increasing angle in the 35°-60° region; however, the angle-dependent resonance position asymptotically approaches the photonic crystal resonance (at 0°) with decreasing angle.[123] The plasmonic transition of this sample occurs ∼2.2-2.3 eV (Figures 7.7a,b), which is less than the position (∼2.57 eV) of the resonance measured at 45° (Figures 7.10 and 7.11). In addition, Figures 7.7a,b show a large change in plasmonic transition with annealing, which means it may be possible that the plasmonic resonance

of the titanium nitride film increased in energy with annealing and around 800° became aligned with the photonic crystal resonance creating the larger reflected intensity. Once annealed at higher temperatures, the titanium nitride plasmonic resonance continued to increase in energy and was no longer in line with the photonic crystal resonance, so the reflected intensity decreased.

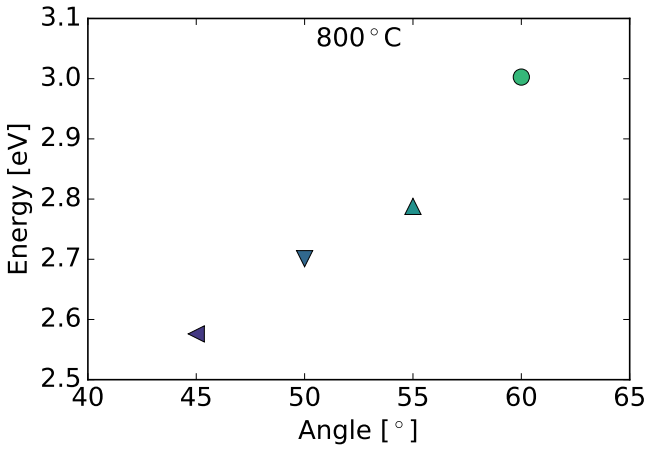

Figure 7.11: **Photonic crystal resonance shift vs. angle.** The peak reflected intensity of the 150-cycle inverse opal occurs when the sample is annealed at 800°C, which may be due to overlapping plasmon resonance with the photonic crystal resonance occurring at 0° incident angle, which cannot be measured with VASE (shown for 45° - 60°.) but can be estimated to be near 2.2 eV, which is near the plasmonic transition wavelength (λ_p) for titanium nitride annealed at 800°C.[131]

In conclusion, this chapter presented work toward conductive and plasmonic photonic crystals in three dimensions, which are difficult to achieve with traditional materials and fabrication techniques, but are made possible using PEALD titanium nitride. We presented a scaleable and high-throughput fabrication technique for making conductive and plasmonic inverse opals, examined their properties as the dielectric function of the titanium nitride was manipulated using annealing, and demonstrated through SEM and optical measurements that these inverse opal structures can survive high temperature environments. Finally, beyond conductive photonic crystals, the fabricated material can also serve as a high surface area electrode for the creation of supercapacitors or water desalination devices.

Chapter 8

Conclusion

This dissertation presented original research that enables the manufacturing of mass-produced plasmonic devices through the establishment of near-field characterization techniques and validating models as well as the engineering of stable plasmonic thin film titanium nitride that can be conformally applied to arbitrary surfaces.

sSNOM was demonstrated as capable of characterizing HAMR heads for next-generation hard disk drives. A validation model was generated using simulated electric field data, AFM tip effects, and electrostatic theory in order to derive meaning from the near-field maps and offer predictions for future measured plasmonic devices. The optical near-field of waveguide-coupled plasmonic antennas in HAMR heads was also characterized bidirectionally using SEM-CL and sSNOM to map both near-field excitations and probed near-fields. Each technique provided unique insight into the heads behavior during drive operation and was demonstrated as useful for the development of scaled-up plasmonic devices.

PEALD of titanium nitride was engineered as a conductive and plasmonic thin film, and its optical, electrical, chemical, and physical properties were analyzed with SE, VASE, FPP, the Hall effect, AES, and SEM with important parameters for attaining reliable, high-quality film depositions given. In addition, annealing was used to further investigate and optimize the films' properties in order to understand the necessary conditions for obtaining the best films qualities for the appropriate applications. Finally, titanium nitride structures were demonstrated in both two (gratings) and three dimensions (inverse opals) as an initial foundation for the later creation of more complex and

mass-produced plasmonic devices. The three dimensional plasmonic and conductive photonic crystals, which can uniquely be made possible using PEALD titanium nitride. Furthermore, these conductive photonic crystal devices can also double as high surface area electrodes, which could be useful for supercapacitors as well as water desalination devices.

Looking to the future, additional proof-of-concept structures should be fabricated in order to more fully demonstrate the usefulness of PEALD titanium nitride for creating stable and scaled-up plasmonic devices. As mentioned in Chapter 2.3.2, "applying an ultrathin (<10 nm, but more like 2-5 nm) coating of titanium nitride or other synthetic metal as a conformal coating around a metallic plasmonic structure offers the desired thermal, chemical, and mechanical protection without giving up the necessary plasmonic and thermal properties." These "candy-coated" plasmonic devices are uniquely seen by the HDD community to be a solution to HAMR's material challenges associated with the plasmonic antenna, and the titanium nitride would serve well as an adhesion layer to the waveguide.[132] In addition, attention should be paid to other synthetic metals such as zirconium nitride as well as ternary and quaternary nitride materials, which have shown promise in some theoretical and experimental investigations.[54,55,133–135]

References

[1] Mark L. Brongersma, John W. Hartman, and Harry A. Atwater. Plasmonics: Electromagnetic energy transfer and switching in nanoparticle chain-arrays below the diffraction limit. *Materials Research Society Symposium Proceedings*, 582:H10.5, 1999.

[2] Mark L. Brongersma. Introductory lecture: nanoplasmonics. *Faraday Discuss.*, 178:9–36, 2015.

[3] Harry A. Atwater. The promise of plasmonics. *Scientific American*, 296:56–63, 2007.

[4] N. Kinsey, M. Ferrera, G. V. Naik, V. E. Babicheva, V. M. Shalaev, and A. Boltasseva. Experimental demonstration of titanium nitride plasmonic interconnects. *Optics Express*, 22(10):12238–12247, may 2014.

[5] A. V. Akimov, A. Mukherjee, C. L. Yu, D. E. Chang, A. S. Zibrov, P. R. Hemmer, H. Park, and M. D. Lukin. Generation of single optical plasmons in metallic nanowires coupled to quantum dots. *Nature*, 450(7168):402–406, 2007.

[6] Rupert F. Oulton, Volker J. Sorger, Thomas Zentgraf, Ren-Min Ma, Christopher Gladden, Lun Dai, Guy Bartal, and Xiang Zhang. Plasmon lasers at deep subwavelength scale. *Nature*, 461(7264):629–632, 2009, 0509168v1.

[7] David L. Jeanmaire and Richard P. Van Duyne. Surface Raman Spectroelectrochemistry Part I. Heterocyclic, aromatic, and aliphatic amines adsorbed on the anodized silver electrode. *Journal of Electroanalytical Chemistry*, 84:1–20, 1977.

[8] Jeffrey N. Anker, W. Paige Hall, Olga Lyandres, Nilam C. Shah, Jing Zhao, and Richard P. Van Duyne. Biosensing with plasmonic nanosensors. *Nature Materials*, 7(6):442–453, 2008.

[9] Nathan C. Lindquist, Prashant Nagpal, Kevin M. McPeak, David J. Norris, and Sang-Hyun Oh. Engineering metallic nanostructures for plasmonics and nanophotonics. *Reports on Progress in Physics*, 75(3):036501, 2012, NIHMS150003.

[10] Harry A. Atwater and Albert Polman. Plasmonics for improved photovoltaic devices. *Nature Materials*, 9(10):865–865, 2010.

[11] Ahmed E. Khalifa and Mohamed A. Swillam. Cheap and efficient plasmonic solar cell. *SPIE Photonics West 2014-OPTO: Optoelectronic Devices and Materials*, 8981:89811R, 2014.

[12] W. A. Challener, Chubing Peng, A. V. Itagi, D. Karns, Wei Peng, Yingguo Peng, XiaoMin Yang, Xiaobin Zhu, N. J. Gokemeijer, Y.-T. Hsia, G. Ju, Robert E. Rottmayer, Michael A. Seigler, and E. C. Gage. Heat-assisted magnetic recording by a near-field transducer with efficient optical energy transfer. *Nature Photonics*, 3(5):303–303, 2009.

[13] Barry C. Stipe, Timothy C. Strand, Chie C. Poon, Hamid Balamane, Thomas D. Boone, Jordan A. Katine, Jui-Lung Li, Vijay Rawat, Hiroaki Nemoto, Akemi Hirotsune, Olav Hellwig, Ricardo Ruiz, Elizabeth Dobisz, Dan S. Kercher, Neil Robertson, Thomas R. Albrecht, and Bruce D. Terris. Magnetic recording at 1.5 Pb m2 using an integrated plasmonic antenna. *Nature Photonics*, 4(July):484–488, 2010.

[14] Alexandra Boltasseva and Harry A. Atwater. Low-loss plasmonic metamaterials. *Science*, 331(6015):290–291, 2011.

[15] Dean J. Campbell and Y. J. Xia. Plasmons: Why should we care? *Journal of Chemical Education*, 84(1):91–96, 2007.

[16] Tong Zhao, Michael Christopher Kautzky, William Albert Challener, and Michael Allen Seigler. HAMR NFT materials with improved thermal stability, 2013.

[17] A. Sherman. Growth and properties of LPCVD titanium nitride as a diffusion barrier for silicon device technology. *Journal of The Electrochemical Society*, 137(6):1892–1897, 1990.

[18] Steven M. George. Atomic layer deposition: An overview. *Chemical Reviews*, 110(1):111–131, 2010.

[19] Urcan Guler, Justus C. Ndukaife, Gururaj V. Naik, A. G. Agwu Nnanna, Alexander Kildishev, Vladimir M. Shalaev, and Alexandra Boltasseva. Local heating with titanium nitride nanoparticles. *Nano Letters*, 13:6078–6083, 2013.

[20] H. Kim. Atomic layer deposition of metal and nitride thin films: Current research efforts and applications for semiconductor device processing. *Journal of Vacuum Science & Technology B: Microelectronics and Nanometer Structures*, 21(6):2231–2261, 2003.

[21] Ing-Song Yu, Hsyi-En Cheng, Chun-Chieh Chang, Yan-Wei Lin, Hou-Tong Chen, Yao-Chin Wang, and Zu-Po Yang. Substrate-insensitive atomic layer deposition of plasmonic titanium nitride films. *Optical Materials Express*, 7(3):777, mar 2017.

[22] F. J. García de Abajo. Optical excitations in electron microscopy. *Reviews of Modern Physics*, 82(1):209–275, 2010, 0903.1669.

[23] Mathieu Kociak, Odile Stéphan, Alexandre Gloter, Luiz F. Zagonel, Luiz H G Tizei, Marcel Tencé, Katia March, Jean Denis Blazit, Zackaria Mahfoud, Arthur Losquin, Sophie Meuret, and Christian Colliex. Seeing and measuring in colours: Electron microscopy and spectroscopies applied to nano-optics. *Comptes Rendus Physique*, 15(2-3):158–175, 2014, 0906.1077.

[24] Jens Dorfmuller, Ralf Vogelgesang, R. Thomas Weitz, Carsten Rockstuhl, Christoph Etrich, Thomas Pertsch, Falk Lederer, and Klaus Kern. Fabry-Perot Resonances in One-Dimensional Plasmonic Nanostructures. *Nano Letters*, 9(6):2372–2377, jun 2009.

[25] R. Hillenbrand and F. Keilmann. Complex optical constants on a subwavelength scale. *Physical Review Letters*, 85(14):3029–3032, 2000.

[26] David J. Griffiths. *Introduction to Electrodynamics*. Prentice Hall, Upper Saddle River, New Jersey, 3 edition, 1999.

[27] John David Jackson. *Classical Electrodynamics*. John Wiley & Sons, Inc., Hoboken, New Jersey, 3 edition, 1999.

[28] Stefan Alexander Maier. *Plasmonics: Fundamentals and Applications*. Springer Science, New York, New York, 2007.

[29] P. Drude. Zur electronentheorie der metalle. *Annalen der Physik (Berlin)*, pages 566–613, 1900.

[30] P. Drude. Zur electronentheorie der metalle ii. Teil. Galvanomagnetische und thermomagnetische effecte. *Annalen der Physik (Berlin)*, pages 369–402, 1900.

[31] Lauren M. Otto, Aaron T. Hammack, Shaul Aloni, D. Frank Ogletree, Deirdre L. Olynick, Scott Dhuey, Bethanie J. H. Stadler, and Adam M. Schwartzberg. Plasma-enhanced atomic layer deposition for plasmonic TiN. 9919:99190N, 2016.

[32] E. Langereis, S. B. S. Heil, H. C. M. Knoops, W. Keuning, M. C. M. van de Sanden, and W. M. M. Kessels. In situ spectroscopic ellipsometry as a versatile tool for studying atomic layer deposition. *Journal of Physics D: Applied Physics*, 42(7):073001, 2009.

[33] E. Langereis, S. B. S. Heil, M. C. M. Van De Sanden, and W. M. M. Kessels. In situ spectroscopic ellipsometry study on the growth of ultrathin TiN films by plasma-assisted atomic layer deposition. *Journal of Applied Physics*, 100(2):023534, 2006.

[34] E. Langereis, S. B. S. Heil, M. C. M. van de Sanden, and W. M. M. Kessels. Initial growth and properties of atomic layer deposited TiN films studied by in situ spectroscopic ellipsometry. *Physica Status Solidi (C)*, 2(12):3958–3962, 2005.

[35] P. Patsalas and S. Logothetidis. Optical, electronic, and transport properties of nanocrystalline titanium nitride thin films. *Journal of Applied Physics*, 90(9):4725–4734, 2001.

[36] J. Rivory, J. M. Behaghel, S. Berthier, and J. Lafait. Optical properties of substoichiometric TiN_x. *Thin Solid Films*, 78:161–165, 1981.

[37] Justin A. Briggs, Gururaj V. Naik, Trevor A. Petach, Brian K. Baum, David Goldhaber-Gordon, and Jennifer A. Dionne. Fully CMOS-compatible titanium nitride nanoantennas. *Applied Physics Letters*, 108(5), 2016.

[38] A. P. Hibbins, J. R. Sambles, and C. R. Lawrence. Surface plasmon-polariton study of the optical dielectric function of titanium nitride. *Journal of Modern Optics*, 45(10):2051–2062, 1998.

[39] D. Steinmüller-Nethl, R. Kovacs, E. Gornik, and P. Rödhammer. Excitation of surface plasmons on titanium nitride films: Determination of the dielectric function. *Thin Solid Films*, 237:277–281, 1994.

[40] Mustafa H. Chowdhury, Krishanu Ray, Stephen K. Gray, James Pond, and Joseph R. Lakowicz. Aluminum nanoparticles as substrates for metal-enhanced fluorescence in the ultraviolet for the label-free detection of biomolecules. *Analytical Chemistry*, 81(4):1397–1403, 2009.

[41] Mark W. Knight, Lifei Liu, Yumin Wang, Lisa Brown, Shaunak Mukherjee, Nicholas S. King, Henry O. Everitt, Peter Nordlander, and Naomi J. Halas. Aluminum plasmonic nanoantennas. *Nano Letters*, 12(11):6000–6004, 2012.

[42] Nan Zhou, Xianfan Xu, Aaron T. Hammack, Barry C. Stipe, Kaizhong Gao, Werner Scholz, and Edward C. Gage. Plasmonic near-field transducer for heat-assisted magnetic recording. *Nanophotonics*, 3(3):141–155, 2014.

[43] Paul R. West, Satoshi Ishii, Gururaj V. Naik, Naresh K. Emani, Vladimir M. Shalaev, and Alexandra Boltasseva. Searching for better plasmonic materials. *Laser & Photonics Reviews*, 4(6):795–808, 2010.

[44] Urcan Guler, Vladimir M. Shalaev, and Alexandra Boltasseva. Nanoparticle plasmonics: Going practical with transition metal nitrides. *Materials Today*, 18(4):227–237, 2014.

[45] Urcan Guler, Alexandra Boltasseva, and Vladimir M. Shalaev. Refractory plasmonics. *Science*, 344(6181):263–264, 2014.

[46] Alexandra Boltasseva and Vladimir M. Shalaev. All that glitters need not be gold. *Science*, 347(6228):1308–1310, 2015.

[47] Urcan Guler, Alexander V. Kildishev, Alexandra Boltasseva, and Vladimir M. Shalaev. Plasmonics on the slope of enlightenment: The role of transition metal nitrides. *Faraday Discuss.*, 178:71–86, 2015.

[48] Urcan Guler, Dmitry Zemlyanov, Jongbum Kim, Zhuoxian Wang, Rohith Chandrasekar, Xiangeng Meng, Eric Stach, Alexander V Kildishev, Vladimir M Shalaev, and Alexandra Boltasseva. Plasmonic Titanium Nitride Nanostructures via Nitridation of Nanopatterned Titanium Dioxide. 2017.

[49] Gururaj V. Naik, Vladimir M. Shalaev, and Alexandra Boltasseva. Alternative plasmonic materials: Beyond gold and silver. *Advanced Materials*, 25(24):3264–3294, 2013.

[50] Gururaj V. Naik, Bivas Saha, Jing Liu, Sammy M. Saber, Eric A. Stach, Joseph M. K. Irudayaraj, Timothy D. Sands, Vladimir M. Shalaev, and Ale Boltasseva. Epitaxial superlattices with titanium nitride as a plasmonic component for optical hyperbolic metamaterials. *Proceedings of the National Academy of Sciences*, 111(21):7546–7551, 2014.

[51] G. Martinez, V. Shutthanandan, S. Thevuthasan, J. F. Chessa, and C. V. Ramana. Effect of thickness on the structure, composition and properties of titanium nitride nano-coatings. *Ceramics International*, 40(4):5757–5764, 2014.

[52] Lili Gui, Shahin Bagheri, Nikolai Strohfeldt, Mario Hentschel, Christine M. Zgrabik, Bernd Metzger, Heiko Linnenbank, Evelyn L. Hu, and Harald Giessen. Nonlinear refractory plasmonics with titanium nitride nanoantennas. *Nano Letters*, 16:5708–5713, 2016.

[53] Zih-Yang Yang, Yi-Hsun Chen, Bo-Huei Liao, and Kuo-Ping Chen. Room temperature fabrication of titanium nitride thin films as plasmonic materials by high-power impulse magnetron sputtering. *Optical Materials Express*, 6(2):540–551, 2016.

[54] Adrien Lalisse, Gilles Tessier, Jérome Plain, and Guillaume Baffou. Plasmonic efficiencies of nanoparticles made of metal nitrides (TiN, ZrN) compared with gold. *Scientific Reports*, 6(November):38647, 2016.

[55] Caitlin Fisher, Lindsay C. Botten, Christopher G. Poulton, Ross C. McPhedran, and C. Martijn de Sterke. End-fire coupling efficiencies of surface plasmons for silver, gold, and plasmonic nitride compounds. *Journal of the Optical Society of America B*, 33(6):1044, jun 2016.

[56] Robert L. Olmon, Brian Slovick, Timothy W. Johnson, David Shelton, Sang-Hyun Oh, Glenn D. Boreman, and Markus B. Raschke. Optical dielectric function of gold. *Physical Review B*, 86(23):235147, dec 2012.

[57] Wei Li, Urcan Guler, Nathaniel Kinsey, Gururaj V. Naik, Alexandra Boltasseva, Jianguo Guan, Vladimir M. Shalaev, and Alexander V. Kildishev. Refractory plasmonics with titanium nitride: broadband metamaterial absorber. *Advanced Materials*, 26:7959–7965, 2014.

[58] Dongchan Jang, Lucas R. Meza, Frank Greer, and Julia R. Greer. Fabrication and deformation of three-dimensional hollow ceramic nanostructures. *Nature Materials*, 12(10):893–898, 2013.

[59] D. S. Stone, K. B. Yoder, and W. D. Sproul. Hardness and elastic modulus of TiN based on continuous indentation technique and new correlation. *Journal of Vacuum Science & Technology A: Vacuum, Surfaces, and Films*, 9(4):2543–2547, jul 1991.

[60] Nathan Nelson-Fitzpatrick, Csaba Guthy, Somayyeh Poshtiban, Eric Finley, Kenneth D. Harris, Brian J. Worfolk, and Stephane Evoy. Atomic layer deposition of TiN for the fabrication of nanomechanical resonators. *Journal of Vacuum Science & Technology A: Vacuum, Surfaces, and Films*, 31(2):021503, 2013.

[61] Martin Moskovits. Surface-enhanced spectroscopy. *Reviews of Modern Physics*, 57(3):783–826, 1985.

[62] E. Abbe. VII.-On the Estimation of Aperture in the Microscope. *Journal of the Royal Microscopical Society*, 1(3):388–423, 1881.

[63] Hideki T. Miyazaki and Yoichi Kurokawa. Squeezing visible light waves into a 3-nm-thick and 55-nm-long plasmon cavity. *Physical Review Letters*, 96(9):1–4, 2006.

[64] Mark I. Stockman. Nanofocusing of optical energy in tapered plasmonic waveguides. *Physical Review Letters*, 93(13):137404, 2004.

[65] Yves C. Martin, Hendrik F. Hamann, and H. Kumar Wickramasinghe. Strength of the electric field in apertureless near-field optical microscopy. *Journal of Applied Physics*, 89(10):5774–5778, 2001.

[66] O. Painter, R. K. Lee, A. Scherer, A. Yariv, J. D. O'Brien, P. D. Dapkus, and I. Kim. Two-dimensional photonic band-gap defect mode laser. *Science*, 284(June):1819–1822, 1999.

[67] Haiming Zhu, Yongping Fu, Fei Meng, Xiaoxi Wu, Zizhou Gong, Qi Ding, Martin V. Gustafsson, M. Tuan Trinh, Song Jin, and X.-Y. Zhu. Lead halide perovskite nanowire lasers with low lasing thresholds and high quality factors. *Nature Materials*, 14(April):636–643, 2015.

[68] Amnon Yariv and Pochi Yeh. *Photonics*. Oxford University Press, Inc., New York, New York, 6 edition, 2007.

[69] Pu-Ling Lu and Stanley H. Charap. Magnetic viscosity in high-density recording. *Journal of Applied Physics*, 75(10):5768–5770, 1994.

[70] Dieter Weller and Andreas Moser. Thermal effect limits in ultrahigh-density magnetic recording. *IEEE Transactions on Magnetics*, 35(6):4423–4439, 1999.

[71] Kohei Imura, Tetsuhiko Nagahara, and Hiromi Okamoto. Imaging of surface plasmon and ultrafast dynamics in gold nanorods by near-field microscopy. *Journal of Physical Chemistry B*, 108(42):16344–16347, 2004.

[72] T. Taubner, F. Keilmann, and R. Hillenbrand. Nanoscale-resolved subsurface imaging by scattering-type near-field optical microscopy. *Optics Express*, 13(22):8893–8899, 2005.

[73] Matthias Rang, Andrew C. Jones, Zhou Fei, Zhi Yuan Li, Benjamin J. Wiley, Xia Younan, and Markus B. Raschke. Optical near-field mapping of plasmonic nanoprisms. *Nano Letters*, 8(10):3357–3363, 2008.

[74] R. Esteban, R. Vogelgesang, J. Dorfmüller, a. Dmitriev, C. Rockstuhl, C. Etrich, and K. Kern. Direct near-field optical imaging of higher order plasmonic resonances. *Nano Letters*, 8(10):3155–3159, 2008.

[75] M. Schnell, A. Garcia-Etxarri, J. Alkorta, J. Aizpurua, and R. Hillenbrand. Phase-resolved mapping of the near-field vector and polarization state in nanoscale antenna gaps. *Nano Letters*, 10(9):3524–3528, 2010.

[76] Nan Zhou, Yan Li, and Xianfan Xu. Resolving near-field from high order signals of scattering near-field scanning optical microscopy. *Optics Express*, 22(15):18715, 2014.

[77] E. A. Ash and G. Nicholls. Super-resolution aperture scanning microscope. *Nature*, 237:510–512, 1972.

[78] A. Lewis, M. Isaacson, A. Harootunian, and A. Muray. Development of a 500 Å spatial resolution light microscope. *Ultramicroscopy*, 13:227–231, 1984, arXiv:1011.1669v3.

[79] D. W. Pohl, W. Denk, and M. Lanz. Optical stethoscopy: Image recording with resolution $\lambda/20$. *Applied Physics Letters*, 44(7):651–653, 1984.

[80] Eric Betzig and Jay K. Trautman. Near-field optics: Microscopy, spectroscopy, and surface modification beyond the diffraction limit. *Science*, 257(5067):189–195, 1992.

[81] Eric Betzig and Robert J. Chichester. Single molecules observed by near-field scanning optical microscopy. *Science*, 262(5138):1422–1425, 1993.

[82] H. A. Bethe. Theory of diffraction by small holes. *Physical Review*, 66(7-8):163–182, 1944.

[83] C. J. Bouwkamp. On Bethe's theory of diffraction by small holes. *Philips Research Reports*, 5:321–332, 1950.

[84] L. Novotny and B. Hecht. Near-field optical probes. In *Principles of Nano-Optics*, chapter 6, pages 170–183. Cambridge University Press, Cambridge, UK, second edition, 2012.

[85] Hemantha K. Wickramasinghe and Clayton C. Williams. Apertureless near field optical microscope, 1990.

[86] F. Zenhausern, Y. Martin, and H. K. Wickramasinghe. Scanning interferometric apertureless microscopy: Optical imaging at 10 Angstrom resolution. *Science*, 269(5227):1083–1085, 1995.

[87] A. Lahrech, R. Bachelot, P. Gleyzes, and A. C. Boccara. Infrared-reflection-mode near-field microscopy using an apertureless probe with a resolution of lambda/600. *Optics Letters*, 21(17):1315–1317, 1996.

[88] B Knoll and F Keilmann. Near-field probing of vibrational absorption for chemical microscopy. *Nature*, 399(May):7–10, 1999.

[89] Alpan Bek, Ralf Vogelgesang, and Klaus Kern. Apertureless scanning near field optical microscope with sub-10 nm resolution. *Review of Scientific Instruments*, 77(4):043703, 2006.

[90] Bernhard Knoll and Fritz Keilmann. Enhanced dielectric contrast in scattering-type scanning near-field optical microscopy. *Optics Communications*, 182(4-6):321–328, 2000.

[91] Alexandre Bouhelier, Michael R. Beversluis, and Lukas Novotny. Near-field scattering of longitudinal fields. *Applied Physics Letters*, 82(25):4596–4598, 2003.

[92] Liwei Chen, Li Cheung Chin, Paul D. Ashby, and Charles M. Lieber. Single-walled carbon nanotube AFM probes: Optimal imaging resolution of nanoclusters and biomolecules in ambient and fluid environments. *Nano Letters*, 4(9):1725–1731, 2004.

[93] Montserrat Calleja, Marta Tello, and Ricardo García. Size determination of field-induced water menisci in noncontact atomic force microscopy. *Journal of Applied Physics*, 92(9):5539–5542, 2002.

[94] J. T. van Wijngaarden, E. Verhagen, A. Polman, C. E. Ross, H. J. Lezec, and H. A. Atwater. Direct imaging of propagation and damping of near-resonance surface plasmon polaritons using cathodoluminescence spectroscopy. *Applied Physics Letters*, 88(22):221111, 2006.

[95] Carrie E. Hofmann, Ernst Jan R. Vesseur, Luke A. Sweatlock, Henri J. Lezec, F. Javier García de Abajo, Albert Polman, and Harry A. Atwater. Plasmonic modes of annular nanoresonators imaged by spectrally resolved cathodoluminescence. *Nano Letters*, 7(12):3612–3617, 2007.

[96] R. Gómez-Medina, N. Yamamoto, M. Nakano, and F. J. García de Abajo. Mapping plasmons in nanoantennas via cathodoluminescence. *New Journal of Physics*, 10(10):105009, 2008.

[97] E. J. R. Vesseur, René De Waele, Martin Kuttge, and Albert Polman. Direct observation of plasmonic modes in Au nanowires using high-resolution cathodoluminescence spectroscopy. *Nano Letters*, 7(9):2843–2846, 2007.

[98] Edward S. Barnard, Toon Coenen, Ernst Jan R Vesseur, Albert Polman, and Mark L. Brongersma. Imaging the hidden modes of ultrathin plasmonic strip antennas by cathodoluminescence. *Nano Letters*, 11(10):4265–4269, 2011.

[99] Linards Skuja. The origin of the intrinsic 1.9 eV luminescence band in glassy SiO2. *Journal of Non-Crystalline Solids*, 179:51–69, 1994.

[100] D. A. Bobb, G. Zhu, M. Mayy, A. V. Gavrilenko, P. Mead, V. I. Gavrilenko, and M. A. Noginov. Engineering of low-loss metal for nanoplasmonic and metamaterials applications. *Applied Physics Letters*, 95(15):151102, 2009, 0907.2484.

[101] Gururaj V. Naik, Jongbum Kim, and Alexandra Boltasseva. Oxides and nitrides as alternative plasmonic materials in the optical range. *Optical Materials Express*, 1(6):1090–1099, 2011.

[102] Kaustubh S. Gadre and T. L. Alford. Contact angle measurements for adhesion energy evaluation of silver and copper films on parylene-n and SiO2 substrates. *Journal of Applied Physics*, 93(2):919–923, 2003.

[103] Martin Hegner, Peter Wagner, and Giorgio Semenza. Ultralarge atomically flat template-stripped Au surfaces for scanning probe microscopy. *Surface Science*, 291:39–46, 1993.

[104] S. B. S. Heil, E. Langereis, F. Roozeboom, M. C. M. van de Sanden, and W. M. M. Kessels. Low-temperature deposition of TiN by plasma-assisted atomic layer deposition. *Journal of The Electrochemical Society*, 153(11):G956–G965, 2006.

[105] Micheal Burke, Alan Blake, Ian M. Povey, Michael Schmidt, Nikolay Petkov, Patrick Carolan, and Aidan J. Quinn. Low sheet resistance titanium nitride films by low-temperature plasma-enhanced atomic layer deposition using design of experiments methodology. *Journal of Vacuum Science & Technology A: Vacuum, Surfaces, and Films*, 32(3):031506, 2014.

[106] Blaine Johs and Jeffrey S. Hale. Dielectric function representation by B-splines. *Physica Status Solidi (A) Applications and Materials Science*, 205(4):715–719, 2008.

[107] Chen Gong and Marina S Leite. Noble metal alloys for plasmonics. *ACS Photonics*, 3(4):507–513, apr 2016.

[108] H K Chiu, T L Lin, Y Hu, K C Leou, H C Lin, M S Tsai, and T Y Huang. Characterization of titanium nitride etch rate and selectivity to silicon dioxide in a Cl2 helicon-wave plasma. *Journal of Vacuum Science & Technology A: Vacuum, Surfaces, and Films*, 19(2):455–459, 2001.

[109] Adam Tarniowy, Ryszard Mania, and Mieczyslaw Rekas. The effect of thermal treatment on the structure , optical and electrical properties of amorphous titanium nitride thin films. pages 93–100, 1997.

[110] Ville Miikkulainen, Markku Leskela, Mikko Ritala, and Riikka L. Puurunen. Crystallinity of inorganic films grown by atomic layer deposition: Overview and general trends. *Journal of Applied Physics*, 113(2):021301, 2013.

[111] J. Musschoot, Q. Xie, D. Deduytsche, S. Van den Berghe, R. L. Van Meirhaeghe, and C. Detavernier. Atomic layer deposition of titanium nitride from TDMAT precursor. *Microelectronic Engineering*, 86(1):72–77, 2009.

[112] Z .H. Cen, B. X. Xu, J. F. Hu, R. Ji, Y. T. Toh, K. D. Ye, and Y .F. Hu. Temperature effect on titanium nitride nanometer thin film in air. *Journal of Physics D: Applied Physics*, 50(7):075105, 2017.

[113] Naresh C. Saha and Harland G. Tompkins. Titanium nitride oxidation chemistry: An x-ray photoelectron spectroscopy study. *Journal of Applied Physics*, 72(7):3072–3079, 1992.

[114] S. C. Sun and M. H. Tsai. Effect of rapid thermal annealing on the electrical and physical properties of metalorganic chemical-vapor-deposited TiN. *Applied Physics Letters*, 670(1996):670, 1995.

[115] J. W. Elam, M. Schuisky, J. D. Ferguson, and S. M. George. Surface chemistry and film growth during TiN atomic layer deposition using TDMAT and NH3. *Thin Solid Films*, 436(2):145–156, 2003.

[116] J. M. Poitevin, D. Maheo, and G. Lemperiere. Thermal stability of TiN films deposited onto silicon substrates. *Thin Solid Films*, 176:7–11, 1989.

[117] V. Ern and A. C. Switendick. Electronic band structure of TiC, TiN, and TiO. *Physical Review*, 137(6A):A1927–A1936, 1965.

[118] J. Haupt, M. A. Baker, M. F. Stroosnijder, and W. Gissler. Auger electron spectroscopy studies on TiN. *Surface and Interface Analysis*, 22:167–170, 1994.

[119] E Yablonovitch. Inhibited Spontaneous Emission in Solid-State Physics and Electronics. *Physical Review Letters*, 58(20):2059–2062, 1987.

[120] Sajeev John. Strong localization of photons in certain disordered dielectric superlattices. *Physical Review Letters*, 58(23):2486–2489, 1987.

[121] Kurt Busch and Sajeev John. Photonic band gap formation in certain self-organizing systems. *Physical Review E*, 58(3):3896–3908, 1998.

[122] Yusuke Imai, Chris E. Finlayson, Pola Goldberg-Oppenheimer, Qibin Zhao, Peter Spahn, David R. E. Snoswell, Andrew I. Haines, G. Peter Hellmann, and Jeremy J. Baumberg. Electrically conductive polymeric photonic crystals. *Soft Matter*, 8:6280–6290, 2012.

[123] Valentina Morandi, Franco Marabelli, Vincenzo Amendola, Moreno Meneghetti, and Davide Comoretto. Colloidal photonic crystals doped with gold nanoparticles: Spectroscopy and optical switching properties. *Advanced Functional Materials*, 17(15):2779–2786, 2007.

[124] M. Scharrer, X. Wu, A. Yamilov, H. Cao, and R. P H Chang. Fabrication of inverted opal ZnO photonic crystals by atomic layer deposition. *Applied Physics Letters*, 86(15):151113, 2005.

[125] Jae Hwang Lee, Wai Leung, Jinho Ahn, Taeho Lee, In Sung Park, Kristen Constant, and Kai Ming Ho. Layer-by-layer photonic crystal fabricated by low-temperature atomic layer deposition. *Applied Physics Letters*, 90(15):151101, 2007.

[126] J. Üpping, R. Salzer, M. Otto, T. Beckers, L. Steidl, R. Zentel, R. Carius, and R. B. Wehrspohn. Transparent conductive oxide photonic crystals on textured substrates. *Photonics and Nanostructures - Fundamentals and Applications*, 9(1):31–34, 2011.

[127] Alessandro Rugge, Jill S. Becker, Roy G. Gordon, and Sarah H. Tolbert. Tungsten nitride inverse opals by atomic layer deposition. *Nano Letters*, 3(9):1293–1297, 2003.

[128] J. S. King, C. W. Neff, C. J. Summers, W. Park, S. Blomquist, E. Forsythe, and D. Morton. High-filling-fraction inverted ZnS opals fabricated by atomic layer deposition. *Applied Physics Letters*, 83(13):2566–2568, 2003.

[129] Alexander Moroz. Three-dimensional complete photonic-band-gap structures in the visible. *Physical Review Letters*, 83(25):5274–5277, 1999.

[130] Alvaro Blanco, Emmanuel Chomski, Serguei Grabtchak, Marta Ibisate, Sajeev John, Stephen W. Leonard, Cefe Lopez, Francisco Meseguer, Hernan Miguez, Jessica P. Mondia, Geoffrey A. Ozin, Ovidiu Toader, and Henry M. van Driel. Large-scale synthesis of a silicon photonic crystal with a complete three-dimensional bandgap near 1.5 micrometers. *Nature*, 405(6785):437–440, may 2000.

[131] E. Ashley Gaulding, Guiji Liu, Christopher T. Chen, Laura Löbbert, Austin Li, Gideon Segev, Johanna Eichhorn, Shaul Aloni, Adam Schartzberg, Ian D. Sharp, and Francesca Toma. Fabrication and optical characterization of polystyrene opal templates for the synthesis of scalable, nanoporous (photo)electrocatalytic materials by electrodeposition. *J. Mater. Chem. A*, 2017.

[132] W. M. Kim, S. H. Kim, K. S. Lee, T. S. Lee, and I. H. Kim. Titanium nitride thin film as an adhesion layer for surface plasmon resonance sensor chips. *Applied Surface Science*, 261:749–752, 2012.

[133] Mukesh Kumar, Satoshi Ishii, Naoto Umezawa, and Tadaaki Nagao. Band engineering of ternary metal nitride system Ti_1-x Zr_xN for plasmonic applications. *Optical Materials Express*, 6(1):29, jan 2016, arXiv:1410.3920v1.

[134] S. Kassavetis, A. Hodroj, C. Metaxa, S. Logothetidis, J. F. Pierson, and P. Patsalas. Optical and electronic properties of conductive ternary nitrides with rare- or alkaline-earth elements. *Journal of Applied Physics*, 120(22):225106, 2016.

[135] S. Kassavetis, D. V. Bellas, G. Abadias, E. Lidorikis, and P. Patsalas. Plasmonic spectral tunability of conductive ternary nitrides. *Applied Physics Letters*, 108(26), 2016.

[136] C. H. Ahn, S. G. Cho, H. J. Lee, K. H. Park, and S. H. Jeong. Characteristics of TiN thin films grown by ALD using TiCl4 and NH3. *Metals and Materials International*, 7(6):621–625, 2001.

Appendix A

Experimental Methods

A.1 Predicting sSNOM Methods

Steady state electromagnetic modeling of the plasmonic system was performed using the FDTD method in Lumerical.

sSNOM measurements were performed with the AIST-NT CombiScope 1000-SPM and tips from Nanosensors (ATEC-NC). The auto non-contact/tapping default mode was used with the 160 μm cantilevers ($\sim$300 kHz resonance), 80 nm oscillation amplitude, and 87 percent set point. An 830 nm laser (diode: Sanyo DL8142-201) was polarized (Thorlabs LPVIS100-MP) and directed with free space optics into the microscope. The microscopes bottom objective (Olympus ULWD MSPlan 50) mount was piezo tuned in three dimensions first for coarse alignment and then for optimal coupling of the laser spot into the waveguide once the tip was hovered over the plasmonic antenna. A 50$\times$ objective (Mitutoyo NIR M Plan Apo NIR 50$\times$, 378-825-5) was precisely aligned with piezo scanners (in objectives xy plane, manual in z) and used to collect the scattered light, which was then observed by an APD (Thorlabs APD120A). The resulting signal passed through a lock-in amplifier (Zurich Instruments HF2LI), and data was collected through the AIST-NT software.

A.2 Bidirectional Characterization Methods

SEM-CL measurements were performed at the Molecular Foundry using custom instrumentation. A HAMR "rowbar" (a linear array of fabricated HAMR heads not yet diced into individual sensors) was mounted on an XY nano-positioning stage (stacked Attocube ECS×3030 closed-loop high vacuum translators with better than 50 nm reproducibility), which was in turn mounted onto the SEM stepper-motor XYZ stage. A cleaved and polished multimode optical fiber (Thorlabs FG200LCC or equivalent, low-OH 200 μm 0.22 NA) was supported from the SEM stage facing the SEM optics. The SEM XYZ stage was used to position the fiber in the center of the SEM image, next the nano-positioning stage inserted the HAMR rowbar sample so that a single sensor was centered in the SEM image.

The SEM electron beam was scanned over the surface of the HAMR plasmonic antenna region to excite near-field optical modes, which coupled through the integrated optical waveguide (used for excitation in HAMR applications). The CL light was collected by the proximity-coupled optical fiber and delivered to external collection optics. A custom vacuum feedthrough was fabricated from a 1/8" Swagelock UltraTorr fitting. Collection fibers had an SMA connector at the external end, and were epoxied into a short section of 1/8" OD polished stainless steel tubing, which was inserted through the UltraTorr fitting, allowing a compression seal to be made on the steel tube.

Optical CL spectroscopy was performed using an Acton 2300i spectrograph with a 150 line/mm grating blazed at 500 nm coupled to an Andor Newton EMCCD spectroscopic camera, both controlled by custom LabView software. An input coupling lens matched the 0.22 fiber N.A to that of the spectrometer (0.1 N.A or f/4). Optical CL images/maps were collected using 20 nm band-pass optical filters and a Perkin-Elmer APD (avalanche photo-diode) single-photon detector. A Nikon 10× objective coupled the filtered fiber output into the APD.

A.3 Plasma-enhanced Atomic Layer Deposition Recipes

Recipes for atomic layer deposited titanium nitride films discussed in this dissertation. The N_2 present in the second plasma of Recipe 1a,b aids the striking of the H_2 plasma. Chapter 6's depositions used Recipe 1a for temperatures 180°C, 200°C, and 300°C,

Recipe 1b for temperatures 40°C and 90°C, and Recipe 3 for the 800 cycles at 300°C sample featured in Figure 6.1b. Longer precursor and plasma gas purge times were allowed for lower temperature depositions to ensure reactant removal before the following stage was introduced.

	Recipe 1a	Recipe 1b	Recipe 2	Recipe 3	Cleaning
PRECURSOR					
Dosage (s)	0.8	0.8	0.8	0.8	
Pressure (mTorr)	40	40	40	40	
Purge (s)	3	8	3	3	
PLASMA 1					
Gas(es)	N_2	N_2	N_2, H_2	N_2	O_2, SF_6
Flow rate (sccm)	40	40	20, 20	40	60, 40
Pressure (mTorr)	10	10	10	10	20
Time (s)	10	10	30	30	10 minutes
Purge (s)	3	5	3	3	2 minutes
PLASMA 2					
Gas(es)	N_2, H_2	N_2, H_2		H_2	
Flow rate (sccm)	3, 50	3, 50		40	
Pressure (mTorr)	10	10		10	
Time (s)	30	30		10	
Purge (s)	3	5		3	

Table A.1: **Deposition recipes.** Deposition recipes for the films discussed in this dissertation. A cleaning recipe is also included.

A PEALD recipe for titanium nitride without hydrogen was also attempted with very poor material resulting. Carbon is the most significant contaminant restricting the conductive and plasmonic properties of the titanium nitride, and the [$(CH_3)N$] ligands on the TDMAT precursor need the hydrogen in order to assist their removal. Use of a precursor such as $TiCl_4$ is ideal for removing the possibility of carbon contamination; however, halogen precursors have reactive tendencies with metal-organic precursors,

and so it is best to not mix them in the same tool to prevent dirtying of the precursor delivery lines.[33,136]

Typical Flexal base pressures at 300°C were in the low 10^{-6} Torr and decreasing to the low to mid 10^{-7} Torr for process temperatures as low as 40°C.

A.4 Stable Plasma-enhanced Atomic Layer Deposition of Nitrides

Use of atomic layer deposited nitride materials for industrial applications requires process predictability and stability. This section offers some pointers and lessons learned in order to achieve process reliability and stability and the highest quality conductive nitrides possible with a given tool and operating constraints.

As was discussed at the end of Chapter 5.3, depositing nitrides in a tool shared with oxide deposition is not ideal. Specifically the deposition of more volatile oxides such as CoOx, WOx, and MoOx can cause significant problems for subsequent nitride deposition if not handled properly. Problems include the contamination of oxygen in the nitride films and (hydrogen) plasma instability (and therefore process instability). These problems can be mitigated with incorporating two processing changes in recipe deposition and pre/post deposition cleaning.

Because PEALD is dependent on a plasma for processing, careful attention should be paid to the plasma tube and its condition throughout tool use (Figure A.1). PEALD tools such as the Oxford Flexal used in this work incorporate a mechanical valve that can be used to isolate the plasma tube from the deposition chamber during precursor dosage. This valve must be opened after precursor purge in order to allow gas flow through the chamber and the desired plasma interaction during the second stage of each cycle. Unfortunately, this mechanical valve is often not adequate and still allows deposition on the inside of the plasma tube. When volatile oxides are deposited on the inside of the plasma tube, the hydrogen plasma in the titanium nitride recipes breaks them down. Increased amounts of reactive oxygen are now present in the chamber and end up in the nitride film. A conductive metal film now also resides on the inside of the plasma tube and can "short" out the hydrogen plasma. The same "shorting" effect can also occur as a result of the conductive titanium nitride being deposited inside the

tube.

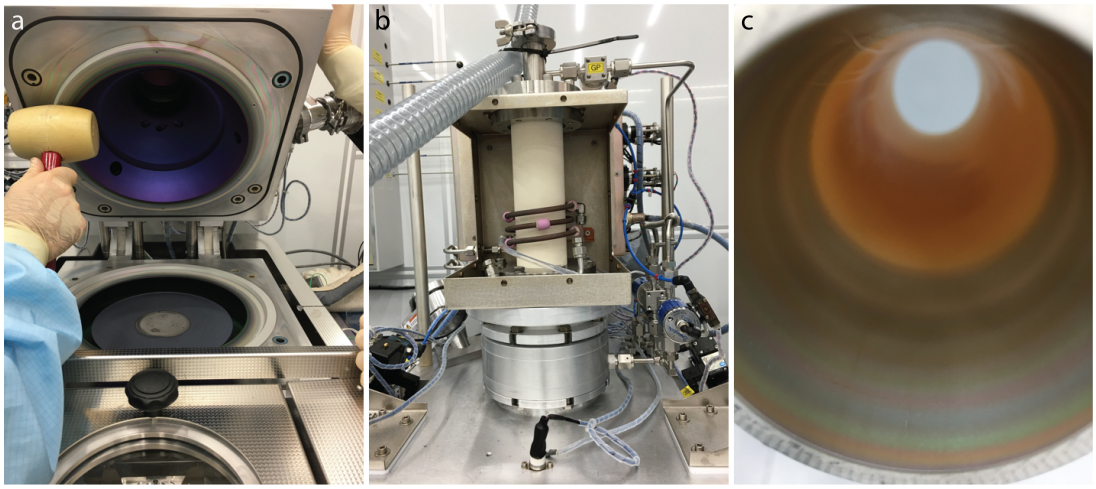

Figure A.1: **A view inside the PEALD chamber and its plasma tube.** (a) During the deposition process, the precursor is introduced through the holes at the chamber corners and the entire inside of the PEALD is coated in material. (b) The plasma tube is located above the deposition chamber and can be isolated from the precursor using a mechanical valve or gas flow. (c) Use of a mechanical valve for plasma tube isolation still allows some material deposition inside the plasma tube.

In order to resolve these issues, conversations were had with Oxford and the following solutions were applied:

- Instead of using the mechanical valve for plasma tube - chamber isolation, leave the valve open for all precursor dosages and instead flow an inert gas such as Ar or N_2 through the plasma tube and into the chamber. Flow rates of ~100 sccm were found to be sufficient. Note that these gases, even the nitrogen, are not reactive with the substrate when there is no plasma.

- Incorporate a plasma cleaning process using SF_6 between depositions. A recipe is included in Table A.1.

The SF_6 plasma is useful for removing much of whatever may have previously been deposited inside the plasma tube and somewhat in the chamber as well. Running the plasma for 10 minutes before beginning a titanium nitride deposition was found to be adequate. It is also essential to continue using the 10 minute plasma clean between

each separate titanium nitride deposition of ∼300 cycles. Less time is appropriate for thinner films, and more may be necessary for thicker films. Running several 300 cycle depositions separated by only 5 minutes of SF_6 plasma cleaning was not adequate and did adversely effect the stability of the third or fourth titanium nitride deposition. It is helpful if other researchers running the volatile oxides in the same chamber also follow up their work with an SF_6 plasma clean. In addition, the SF_6 plasma may cause a delay in film nucleation above the 8-12 cycles necessary without the cleaning. This should be taken into account when depositing ultrathin (<10 nm).

A.5 Annealing Experimentation

Anneals were performed in a glass tube furnace (ThermoFisher Scientific Lindberg Blue M, 1" tube, 1100°C max), where the tube ends, gas attachments, and glass slide sample holder were first cleaned with IPA. pumped to $\sim 1.5 \times 10^{-1}$ Torr and purged by filling the tube with argon (twice) before flowing 250 sccm Ar and 20 sccm H_2 through the argon filled tube. After the first pump down, a leak check was performed by isolating the pump from the tube and confirming that the tube's connections to the gas flow did not contain leaks. The furnace temperature was ramped from room temperature (∼20°C) to the annealing temperature as fast as possible (∼10's of minutes), annealed for one hour, and then cooled. The hydrogen gas flow was stopped only once the samples were cool enough to remove from the furnace (≤80-100°C). Samples of different deposition temperatures were annealed simultaneously under the same annealing conditions and always in the same order along the direction of gas flow through the tube.

A.6 Opal Synthesis

Quartz substrates (1 mm thick, purchased from VWR) were cleaved into 1×2 cm^2 pieces and cleaned using the following procedure: 1) sonication in an Alconox/deionized (DI) water solution for 15 minutes, 2) followed by sonication in pure DI water for 15 minutes, 3) and sonication in a 1:1:1 acetone:ethanol:DI water solution for 15 minutes. Finally, the substrates were plasma treated in air for ∼5 min. Care was taken between each step to inspect each substrate and remove any dust particles via nitrogen stream.

Non-functionalized 390 nm polystyrene (PS) beads (25 mg/mL in DI water) were purchased from Bangs Labs.

The slow-evaporation deposition of the PS bead opal templates is described in detail in a recent publication.[131] In brief, 390 nm PS bead solutions were diluted to 0.1 v/v% using Millipore® water (18.2 MΩ cm, at 25°C). A few drops of a 1% solution of TritonX were added (3 drops / 8 mL). The solution was sonicated for 15 minutes just before deposition. The substrates were each set in a small vial (1.5 cm diameter and 4.5 cm height) tilted at a 60°C angle (where 0°C is flat horizontal). 1.5 mL of the PS bead solution was carefully dispensed into the vials. The vials were arranged in a 4 4 grid on a hotplate for a total of 16 vials. A crystallization dish (15.0 cm diameter and 7.5 cm height) was used to cover the hotplate. Filter paper was taped to the bottom of the dish to protect the vials from condensation. The hotplate was then set to 50°C. The humidity and evaporation rate were reproduced by always keeping a constant amount of water in the enclosed system. After the deposition, the films were immersed in ethanol for 1 hour, and then removed and carefully dried from the back side of the substrate using a gentle stream of nitrogen. The films were then annealed on a hotplate at 90°C for 10 minutes.

Appendix B

Supporting Information

This appendix contains the supplemental information not included in the main stories for the HAMR characterization techniques presented in Chapters 3 and 4

B.1 Predicting sSNOM

This supporting information contains additional modeled near-field mappings as well as other graphs to more fully show how the modeled results change with different values used for the input parameters (tip radius, distance of closest approach DCA) and support paper conclusions.

B.1.1 Additional Mappings for the Parameters Chosen in the Main Text (15 nm radius, 8 nm DCA)

Figure B.1: **Complete harmonics for Figure 3.6.** (Next 3 pages.) The set of six harmonic mappings complementary to Figure 3.6 where only $1\omega_0$ and $6\omega_0$ were given.

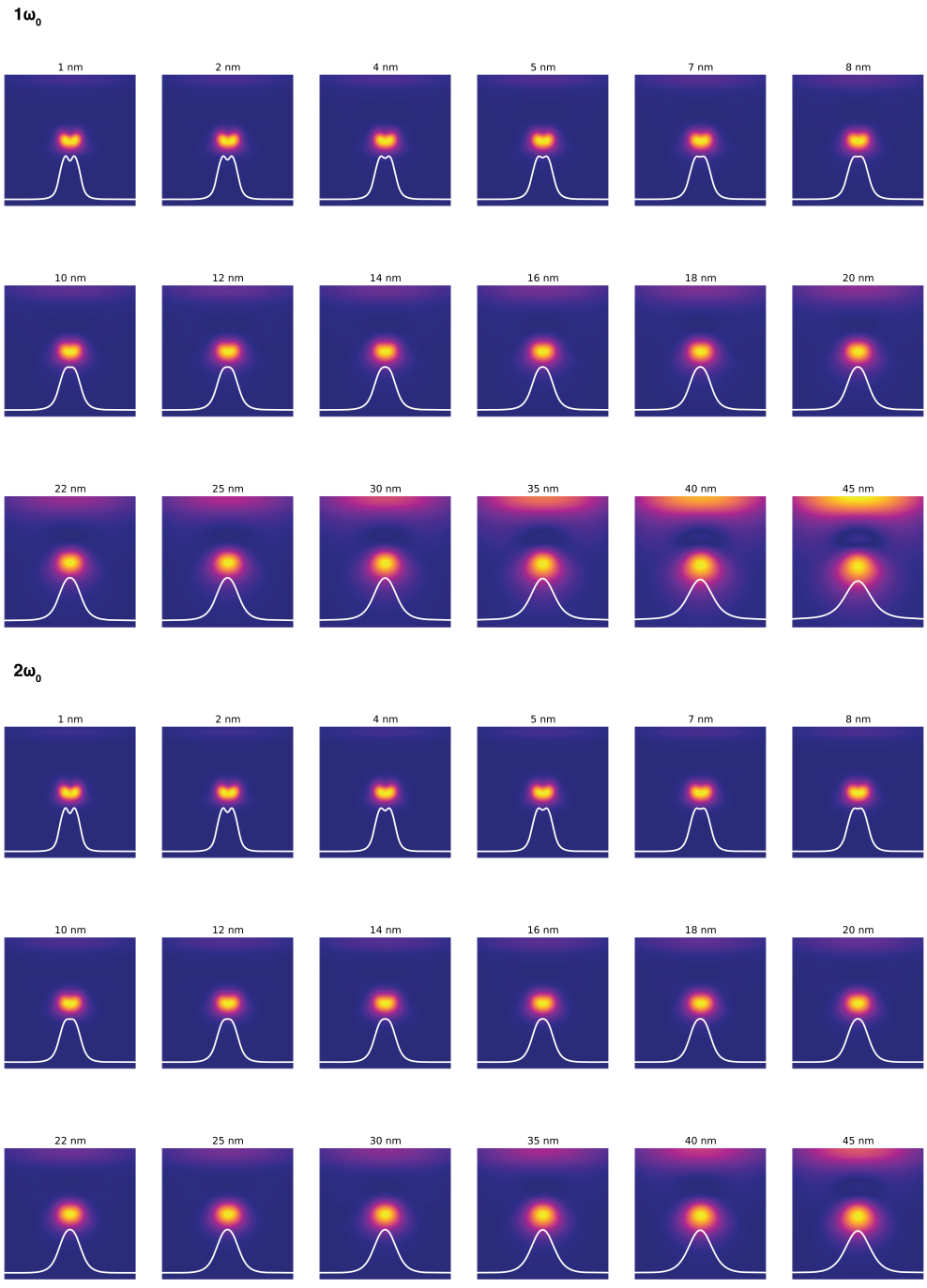
1ω0
1 nm
2 nm
4 nm
5 nm
7 nm
8 nm
10 nm
12 nm
14 nm
16 nm
18 nm
20 nm
22 nm
25 nm
30 nm
35 nm
40 nm
45 nm
2ω0
1 nm
2 nm
4 nm
5 nm
7 nm
8 nm
10 nm
12 nm
14 nm
16 nm
18 nm
20 nm
22 nm
25 nm
30 nm
35 nm
40 nm
45 nm

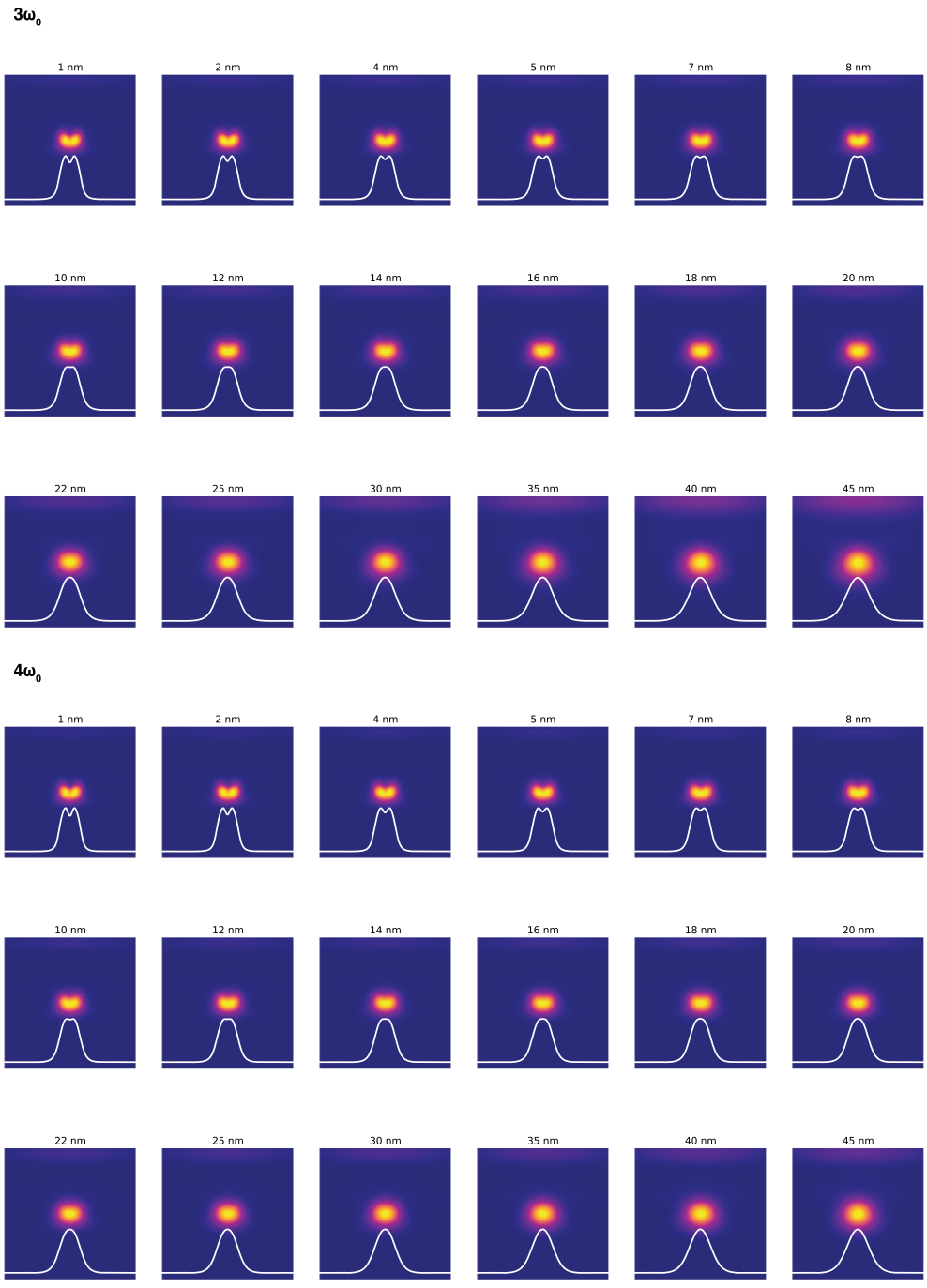
3ω0
1 nm
2 nm
4 nm
5 nm
7 nm
8 nm
10 nm
12 nm
14 nm
16 nm
18 nm
20 nm
22 nm
25 nm
30 nm
35 nm
40 nm
45 nm
4ω0
1 nm
2 nm
4 nm
5 nm
7 nm
8 nm
10 nm
12 nm
14 nm
16 nm
18 nm
20 nm
22 nm
25 nm
30 nm
35 nm
40 nm
45 nm

$5\omega_0$

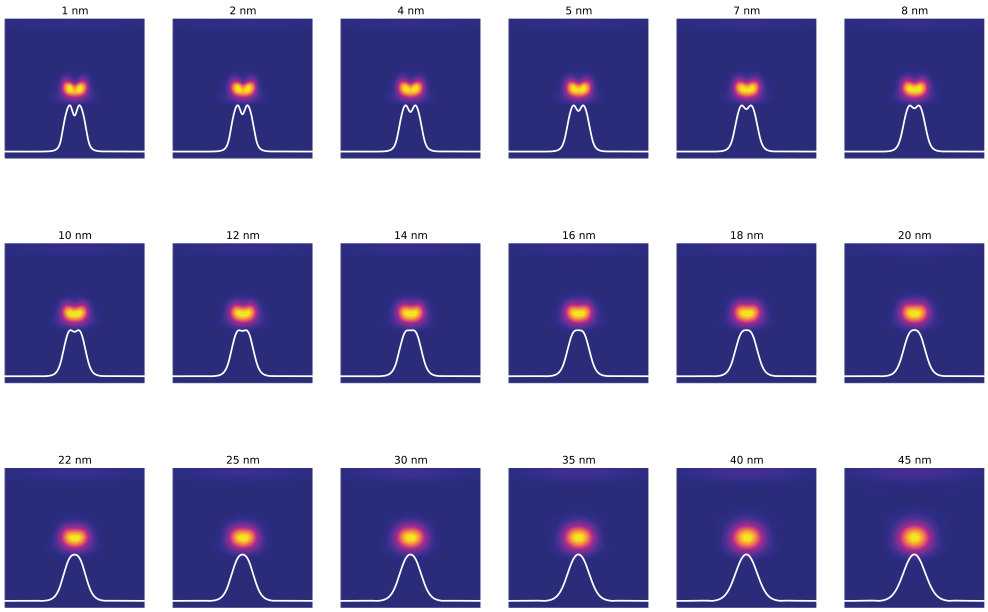

$6\omega_0$

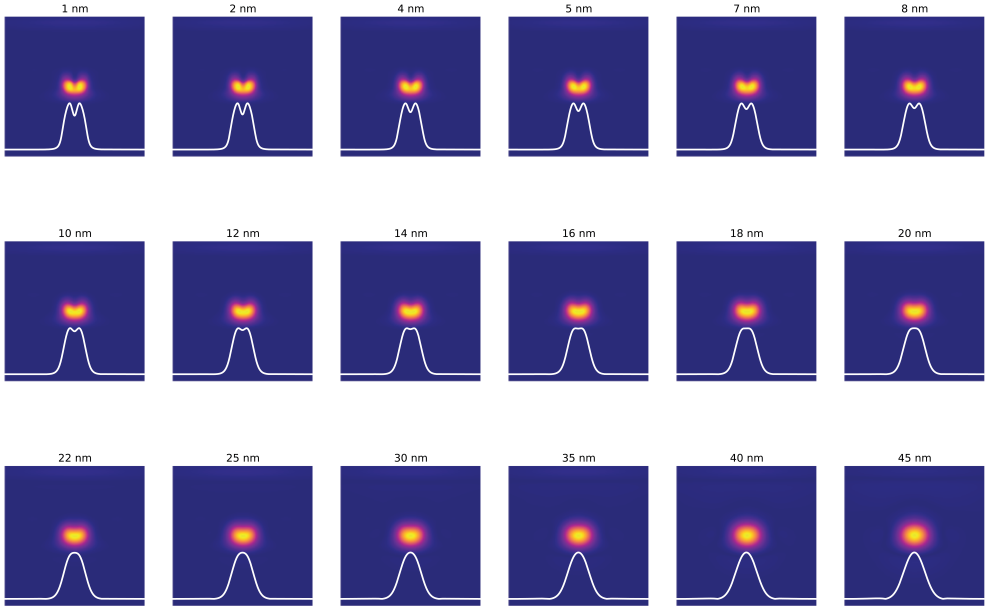

B.1.2 Figures for Observing Trends in the Maximums of Each Mapping as a Function of DCA Height, Tip Radius, and Harmonic

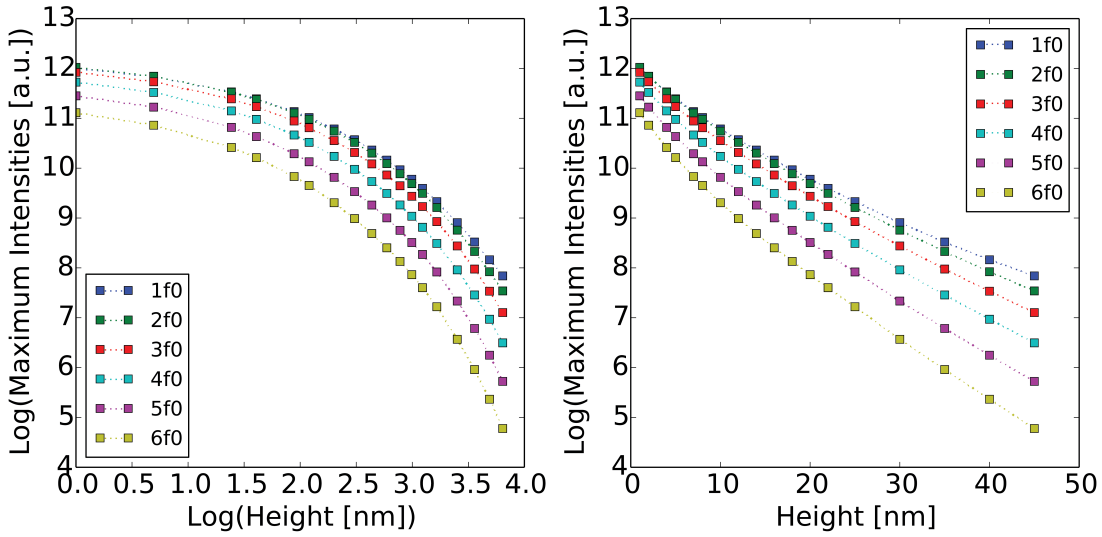

Figure B.2: **Maximum intensity decay with DCA and harmonic.** The decay relationship of the maximum intensity of each mapping as a function of both DCA height and harmonic. Faster decay is observed for higher DCAs as well as for higher harmonics.

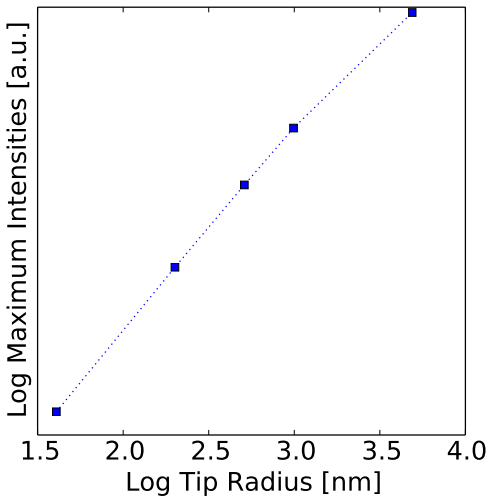

Figure B.3: **Maximum intensities vs. tip radius.** The maximum of each mapping as a function of modeled tip radius plotted for only the $1\omega_0$ but representative of all harmonics.

B.1.3 Near-field Mappings for Other Modeled Tip Radii

Figure B.4: **Harmonics for a 20 nm tip radius.** (Next page.) The modeled $1\omega_0$ and $6\omega_0$ for a 20 nm tip radius. A tip radius of this size was determined to be too large to fit the experimentally measured data. The near-field mappings generated by the model for the $6\omega_0$ do not show a bifurcation in the shape of the near-field spot as is seen in the experimental data. This is because the top-hat shaped tip with a 20 nm radius is now comparable in size to the plasmonic antenna and its near-field spot. The tip simply scatters the field from the two corner spots out across the whole antenna as it scans over, which smears out the observed response.

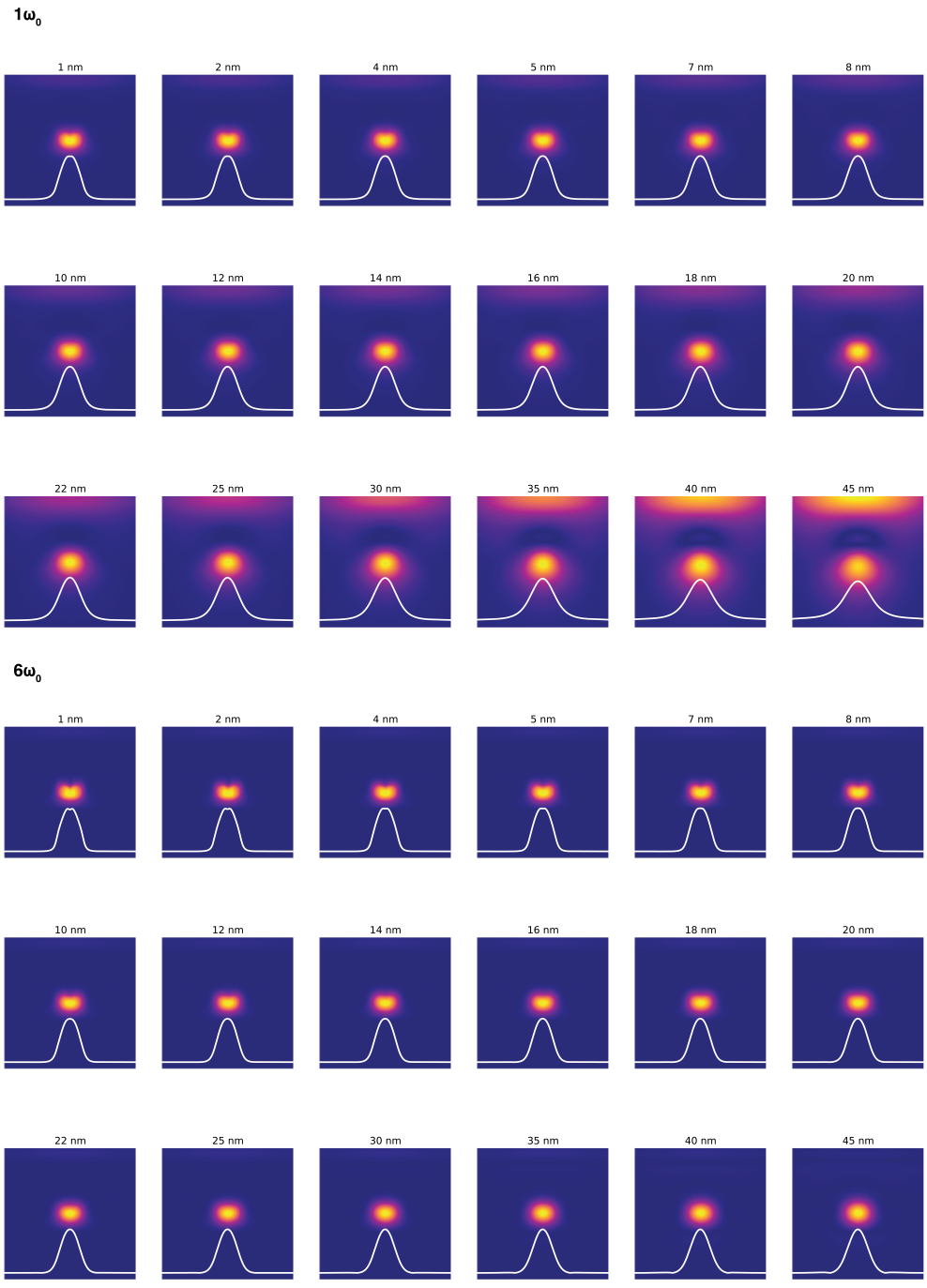
1ω0
1 nm
2 nm
4 nm
5 nm
7 nm
8 nm
10 nm
12 nm
14 nm
16 nm
18 nm
20 nm
22 nm
25 nm
30 nm
35 nm
40 nm
45 nm
6ω0
1 nm
2 nm
4 nm
5 nm
7 nm
8 nm
10 nm
12 nm
14 nm
16 nm
18 nm
20 nm
22 nm
25 nm
30 nm
35 nm
40 nm
45 nm

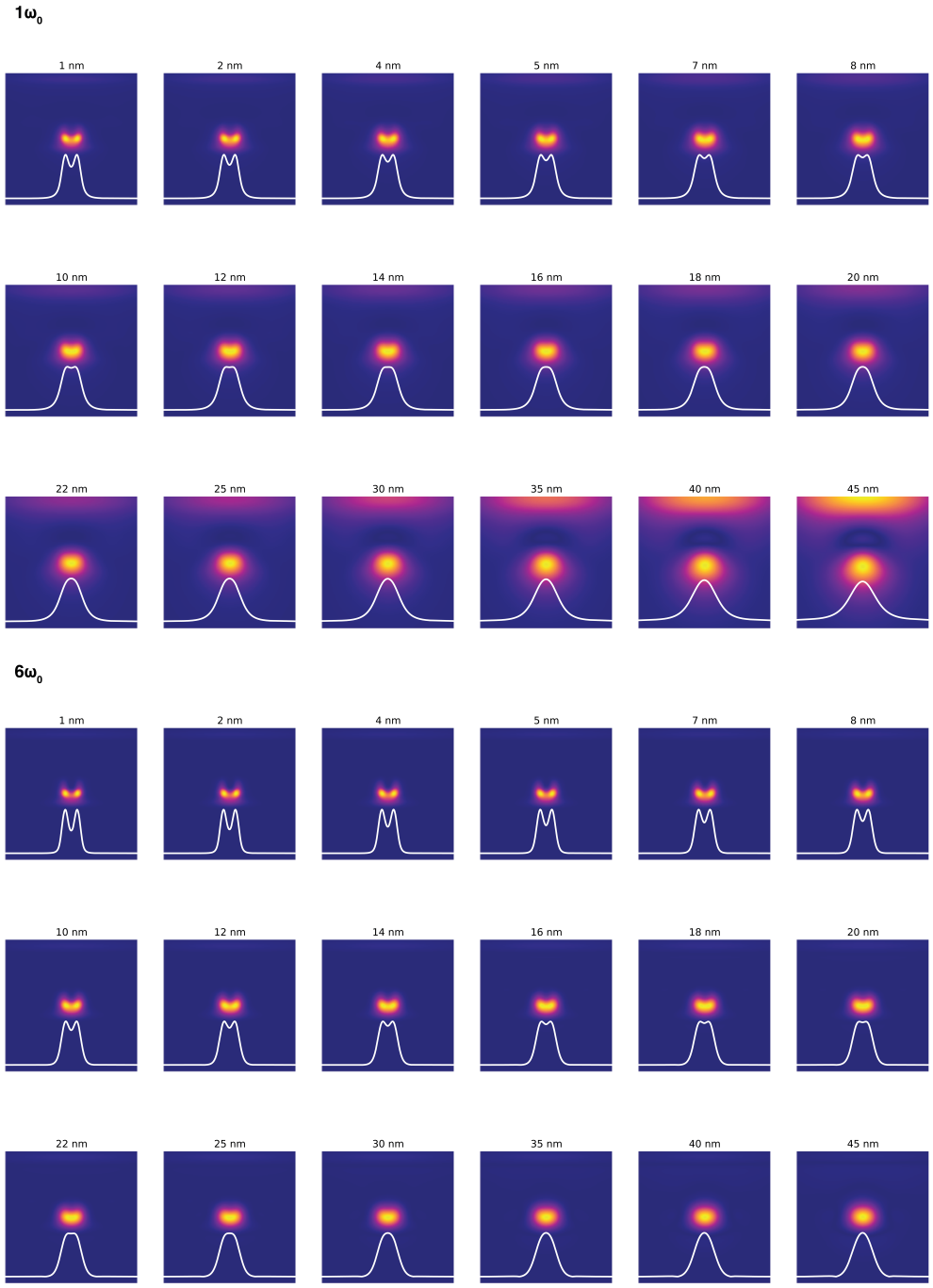

Figure B.5: **Harmonics for a 10 nm tip radius.** The modeled $1\omega_0$ and $6\omega_0$ for a 10 nm tip radius. This modeled tip radius together with a DCA of 16 nm shows reasonable agreement with the experimental data; however, based on AFM mechanics, we believed that this DCA was too large to be a reasonable estimate for our experimental conditions. Additional mappings for all harmonics modeled from this condition are in Figure B.6.

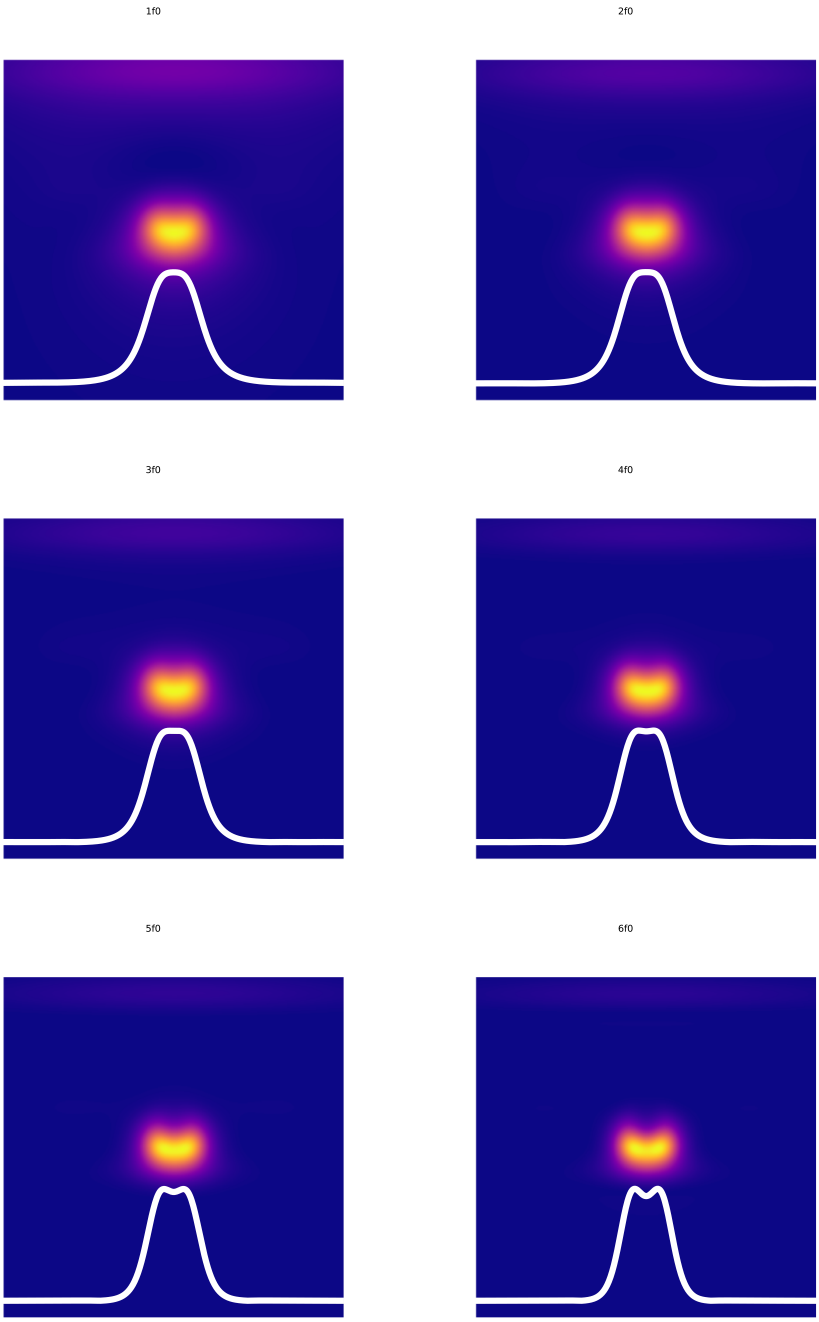

Figure B.6: **Harmonics for a 10 nm tip radius and 16 nm DCA.** All six modeled harmonic mappings for the 10 nm tip radius and 16 nm DCA condition.

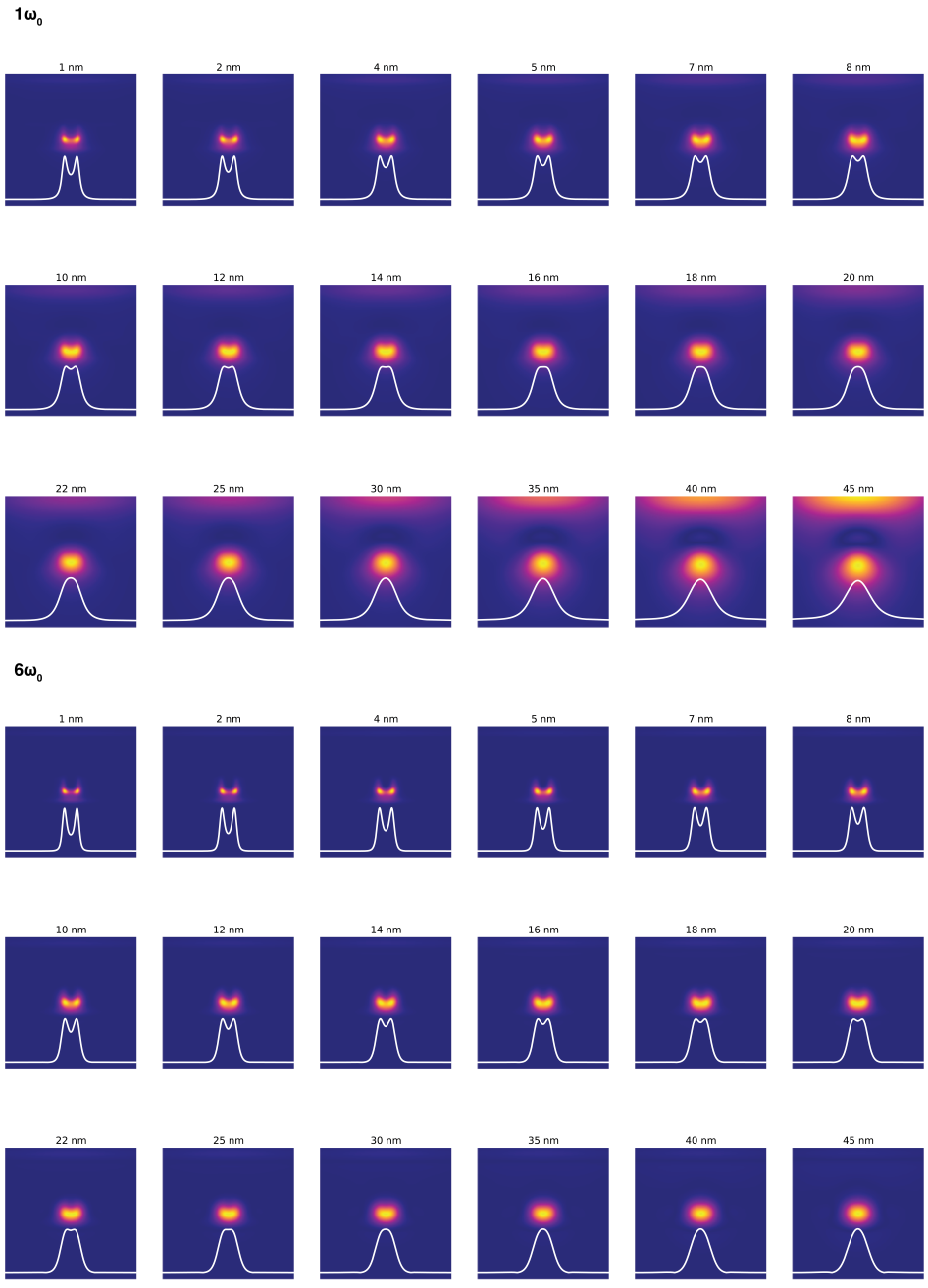

Figure B.7: **Harmonics for a 10 nm tip radius.** The modeled $1\omega_0$ and $6\omega_0$ for a 5 nm tip radius.

B.1.4 Near-field Mappings for Other Modeled Distances of Closest Approach

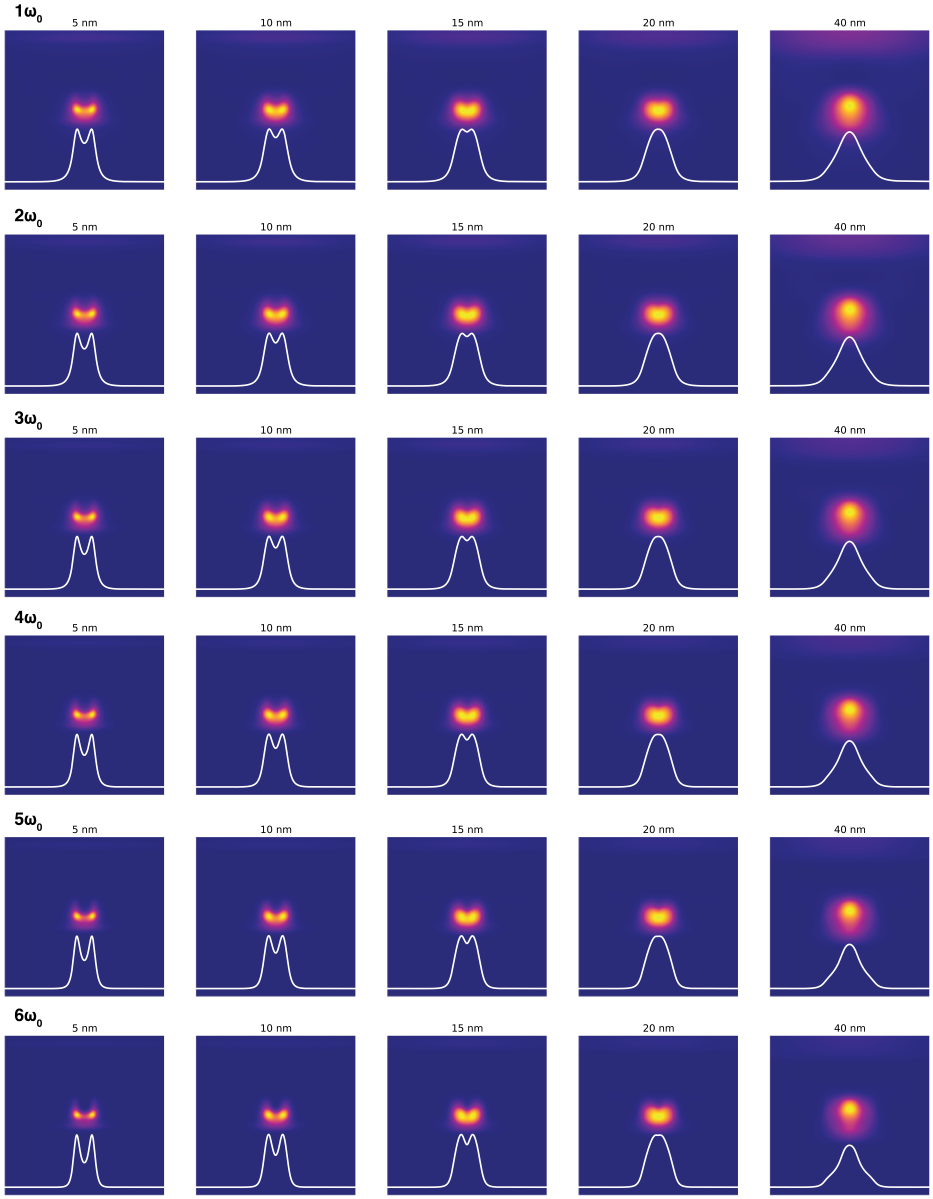

Figure B.8: **Harmonics for a 4 nm DCA.** A modeled 4 nm tip DCA shows the spot bifurcation in the $1\omega_0$ with the 15 nm tip radius, which is not in agreement with the experimental data and the AFM mechanical expectations.

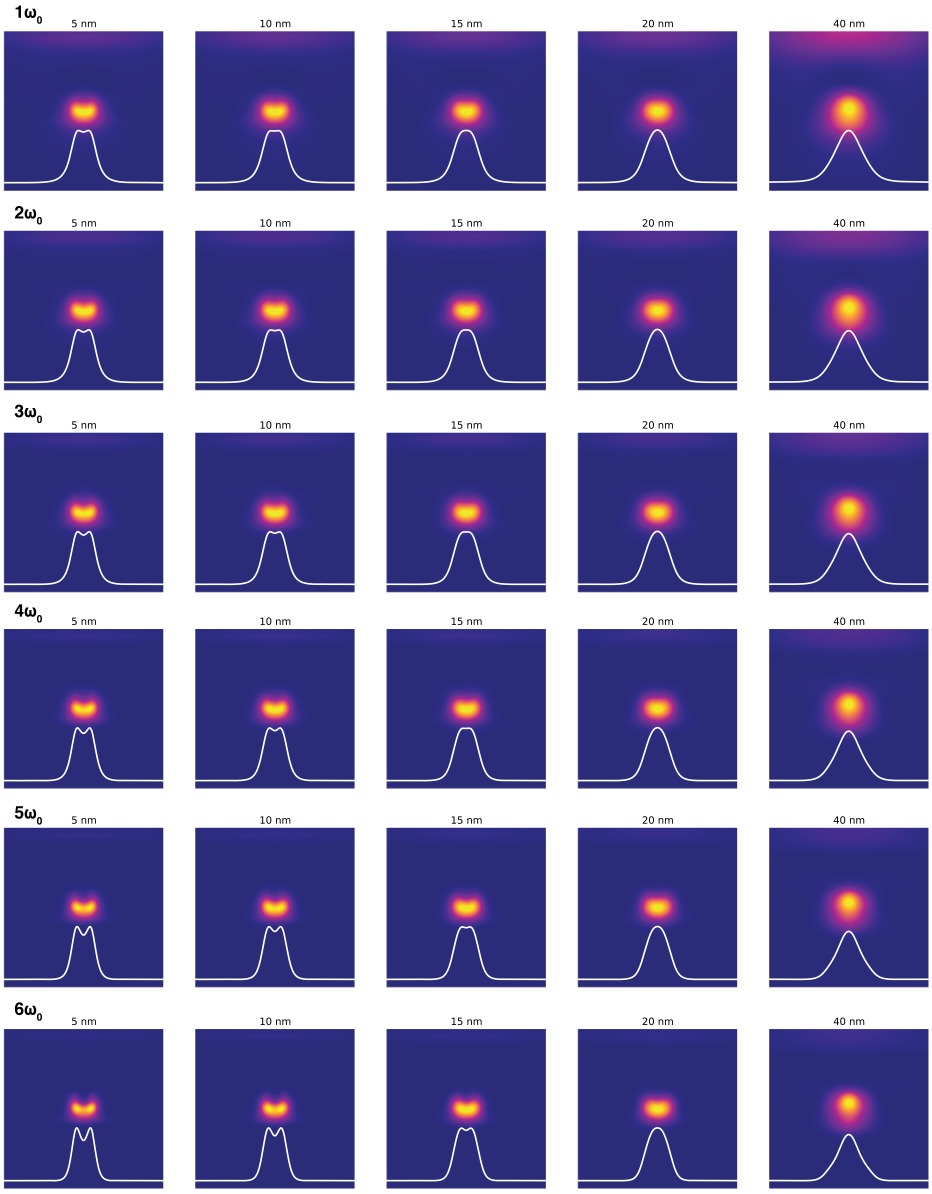

Figure B.9: **Harmonics for a 12 nm DCA.** A modeled 12 nm tip DCA does not show enough spot bifurcation in the $6\omega_0$ with the 15 nm tip radius, and it shows too much in the $1\omega_0$ with the 10 nm tip radius.

B.1.5 Simulated Electric Field Intensity

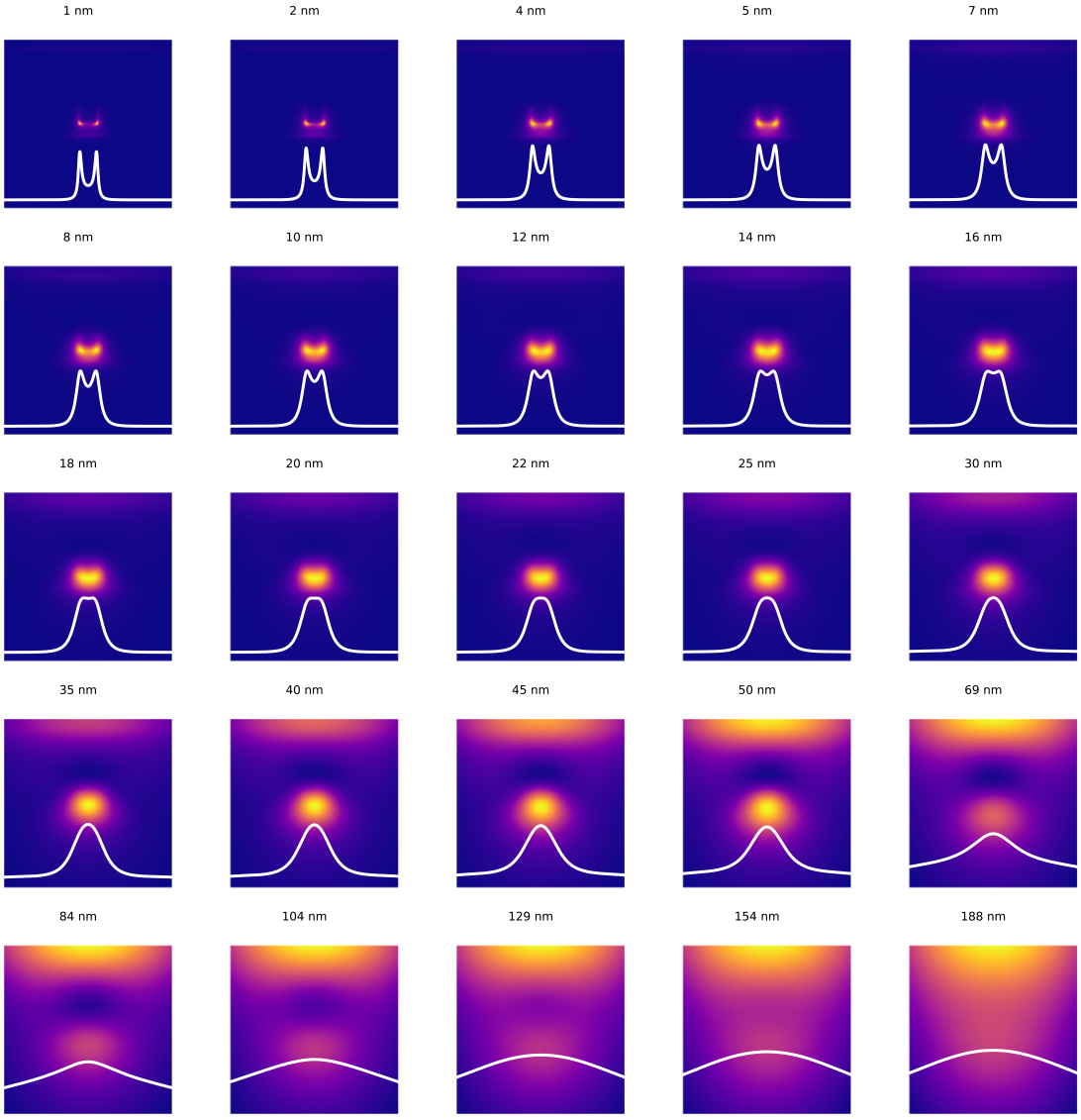

Figure B.10: **Simulated electric field intensity.** Simulated electric field intensity in discrete planes above the air-bearing surface (ABS) help us observe which regions play dominant roles in each harmonic mapped by the sSNOM model as well as the experimental sSNOM measurements. Maps are labeled with their height above the ABS.

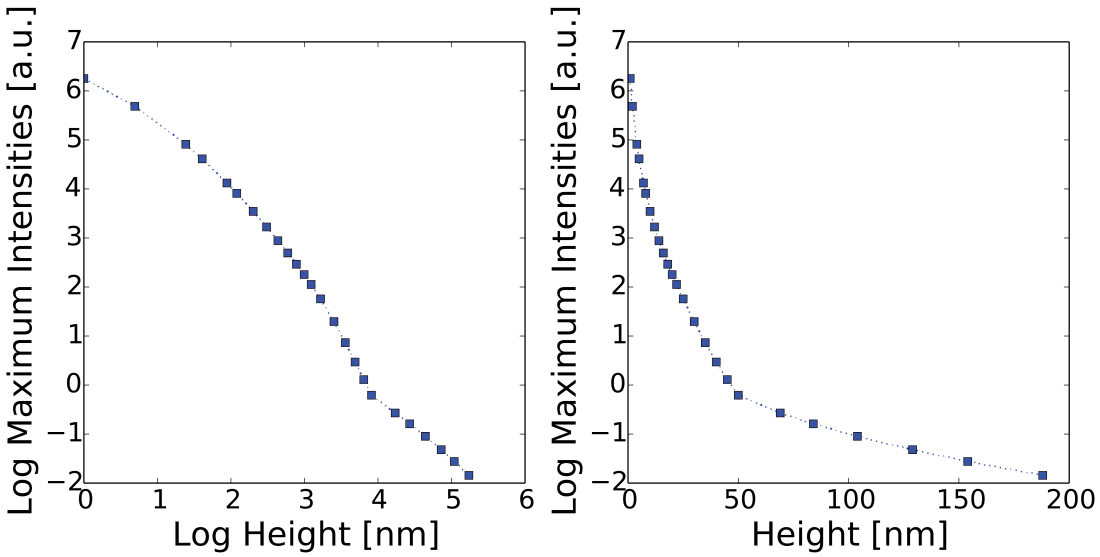

Figure B.11: **Maximum electric field intensities of the maps in Figure B.10 over the entire 400 nm × 400 nm region.** At a height of ∼50 nm above the ABS, the maximum electric field intensity region shifts from over the "notch" region of the plasmonic antenna to over the side of the "E" shaped antenna as is evident in Figure S10. This effect is seen in the 10 of the experimental data, and to some degree in the modeled data as well, although it is not as evident in the specific condition (15 nm tip radius, 8 nm DCA) presented in the main text.

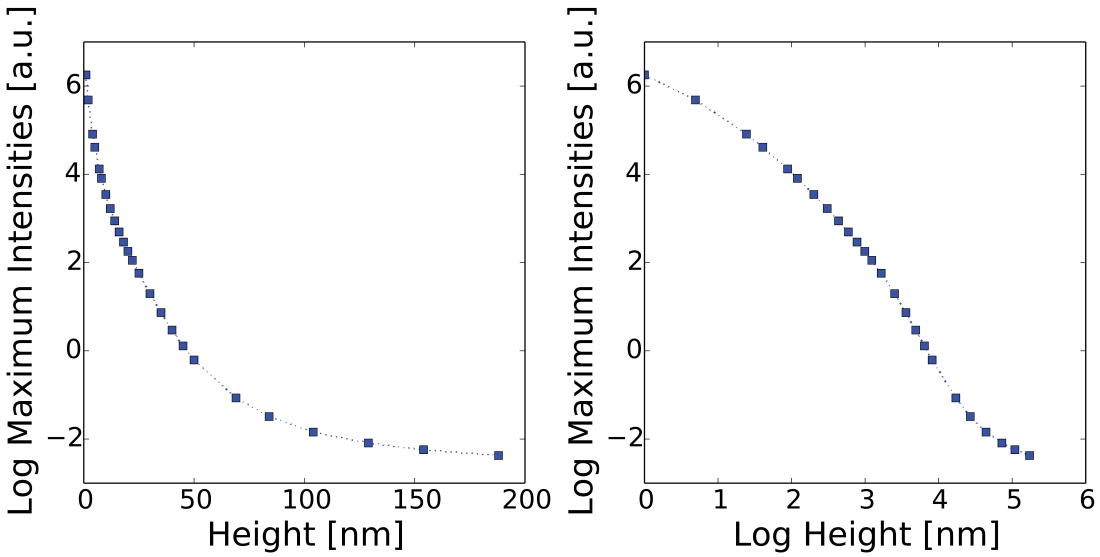

Figure B.12: **Maximum electric field intensities of the maps in Figure B.10 over the center region (over the notch that generates the main near-field spot).** The same sharp transition at ∼50 nm above the ABS is not as evident as in Figure B.11 (over the entire map shown); however, the decay trend still alters.

B.2 Bidirectional Characterization

This supplementary information contains schematics and full data sets for the two techniques discussed in the main text.

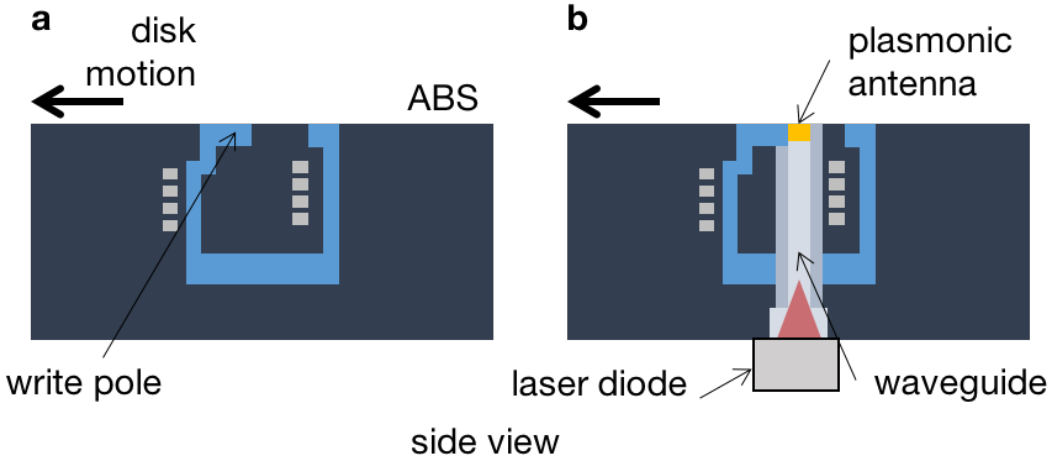

Figure B.13: **Schematics comparing hard disk drive write head profiles.** (a) for standard perpendicular magnetic recording and (b) for next-generation heat-assisted magnetic recording, which incorporates many additional elements including a waveguide-coupled plasmonic antenna.

B.2.1 SEM-CL

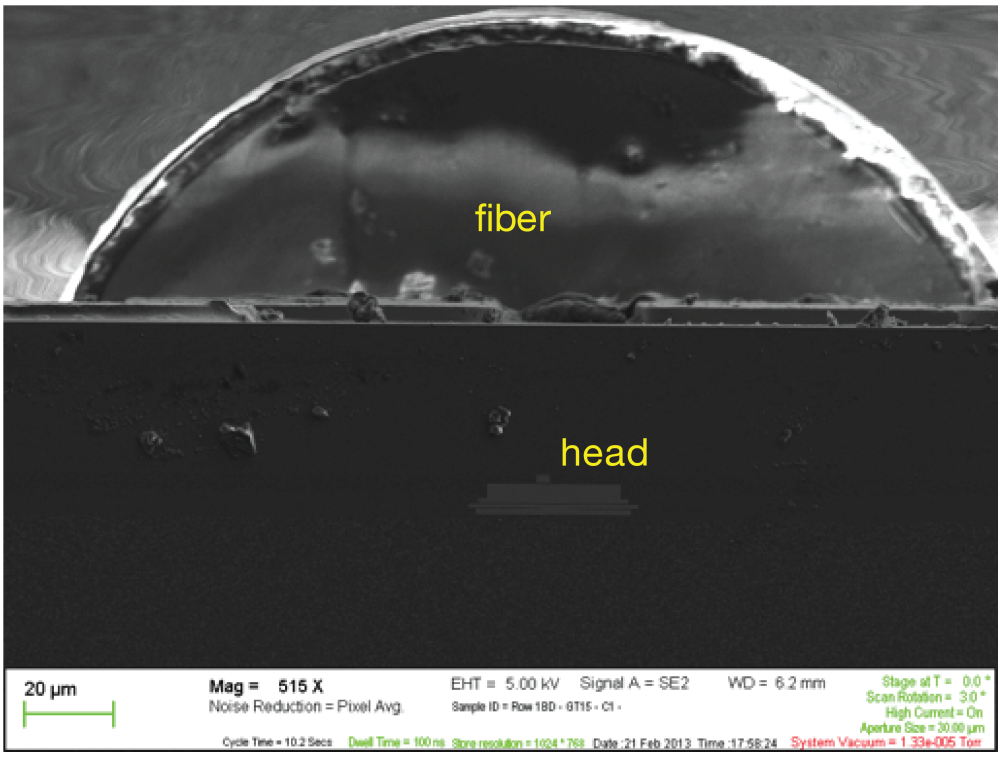

Figure B.14: **HAMR head on a fiber for SEM-CL.** Large-scale scanning electron microscopy (SEM) image of a heat-assisted magnetic recording (HAMR) head mounted on an optical fiber for cathodoluminescence (CL) imaging.

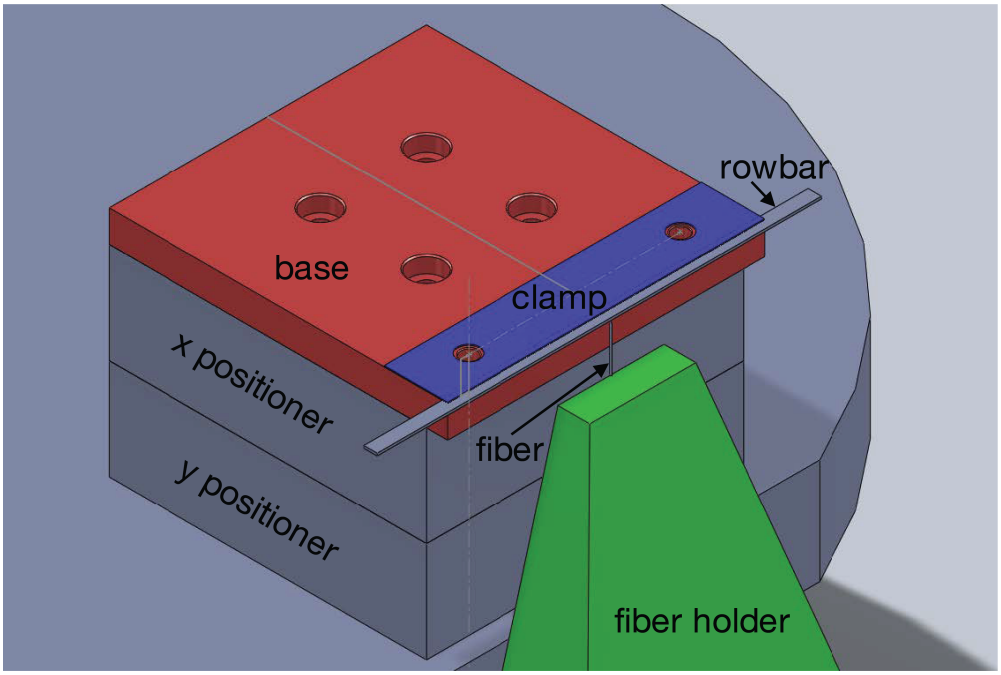

Figure B.15: **Mounting schematic for SEM-CL experiments.** An entire rowbar (a set of many of many HAMR heads not yet cut apart post fabrication) was mounted into the SEM holder.

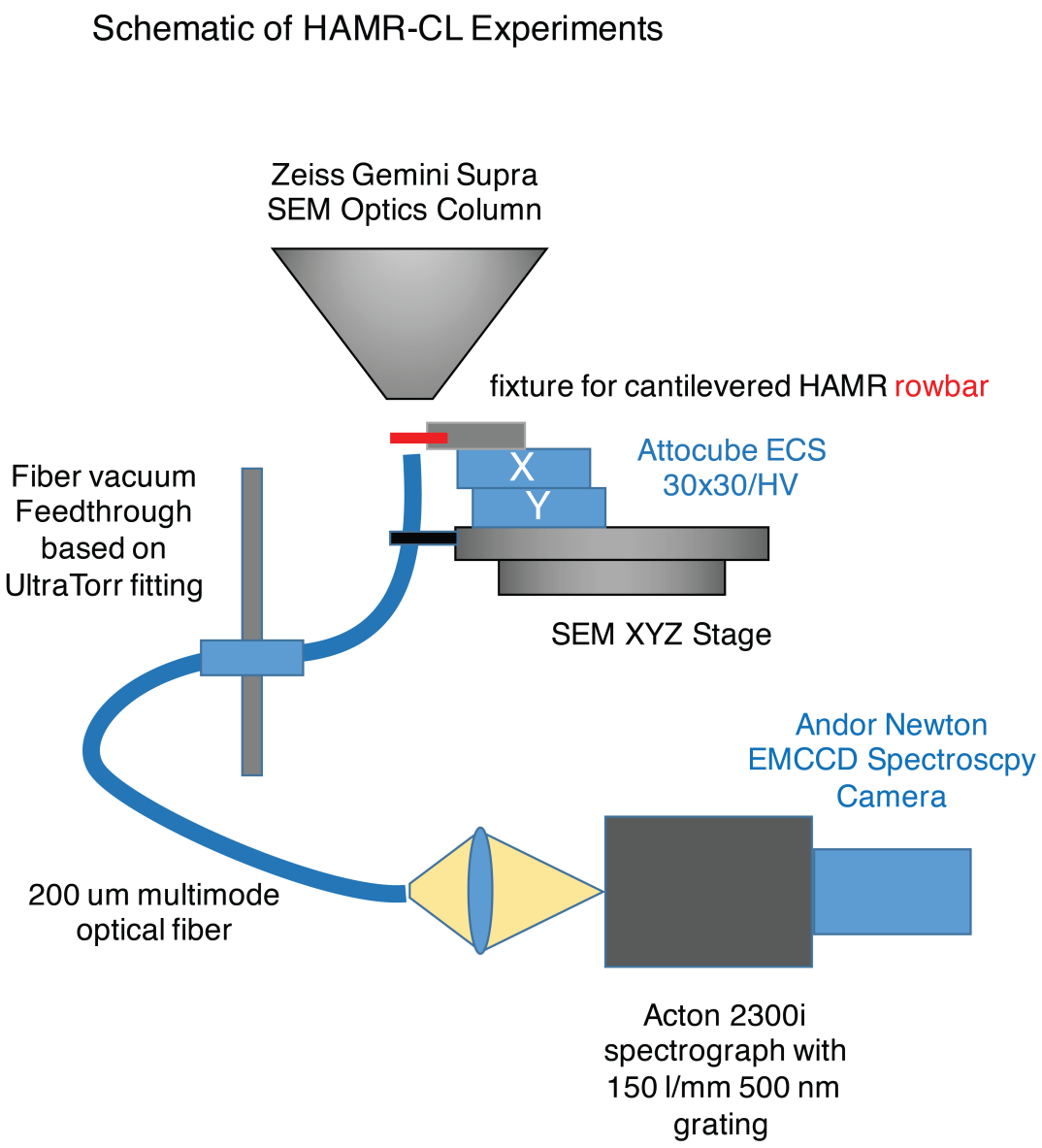

Figure B.16: **Detection schematic of the SEM-CL signal.**

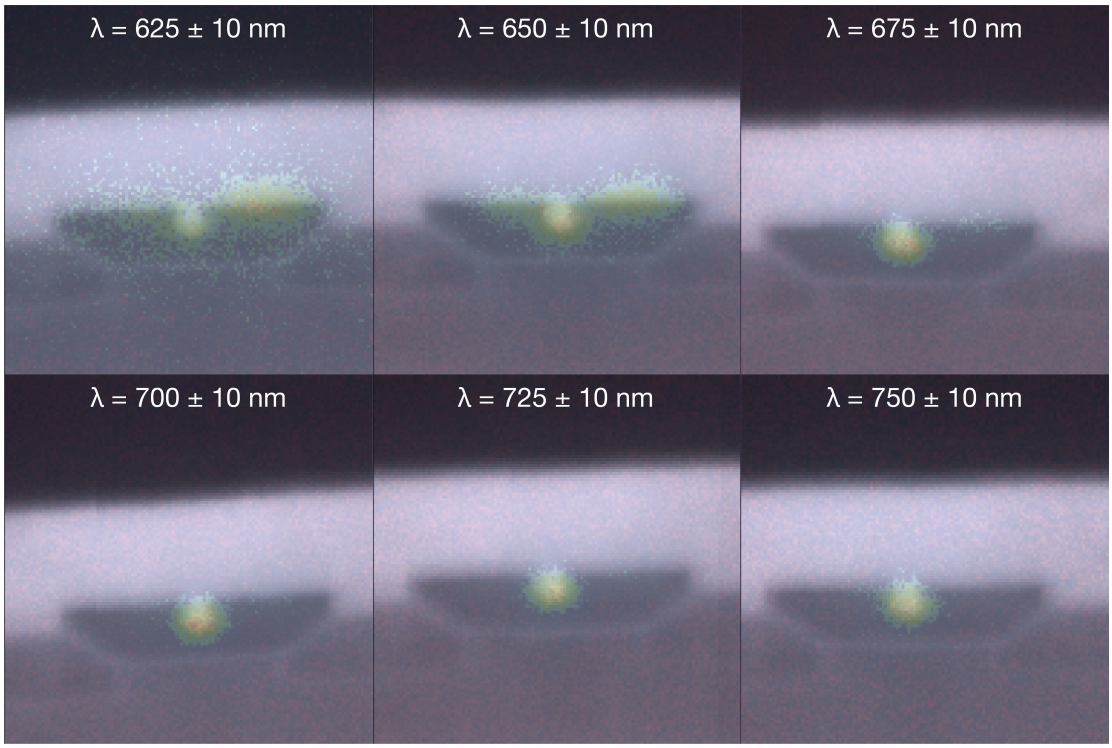

Figure B.17: **The complete set of recorded SEM-CL mappings over 20 nm wavelength windows as in Figure ??.** The evanescent near-field is confined to the notch region for wavelengths 665-760 nm.

B.2.2 sSNOM

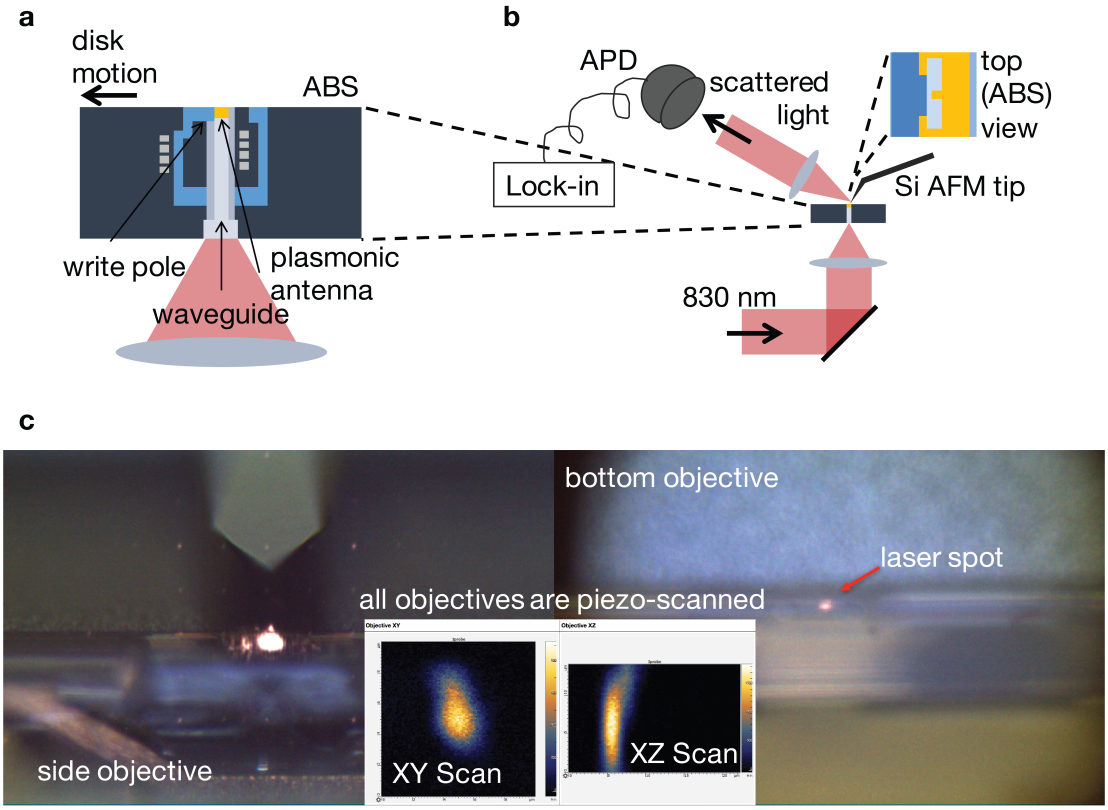

Figure B.18: **Schematic of the heat-assisted magnetic recording (HAMR) heads as imaged by the AIST-NT sSNOM system.** A side profile of (a) a HAMR head and (b) the sSNOM system, including the layout of the scanned surface of the HAMR head. (c) Camera views from the side (left) and bottom (right) objectives of the sSNOM system. When the AFM tip was positioned over the antenna, each objective would be piezo scanned to allow for precise alignment of the laser light through the waveguide and to the antenna. Images would be collected from the objective scans to determine the precise position necessary for optimal alignment. Adapted from CITE PAPER HERE.

830 nm Laser Excitation

Figure B.19: **Complete harmonics for 830 nm illumination.** The full set of sSNOM data taken with 830 nm laser light with harmonics $1\omega_0$ to $6\omega_0$ and polarizations from $-100°$ to $+100°$.

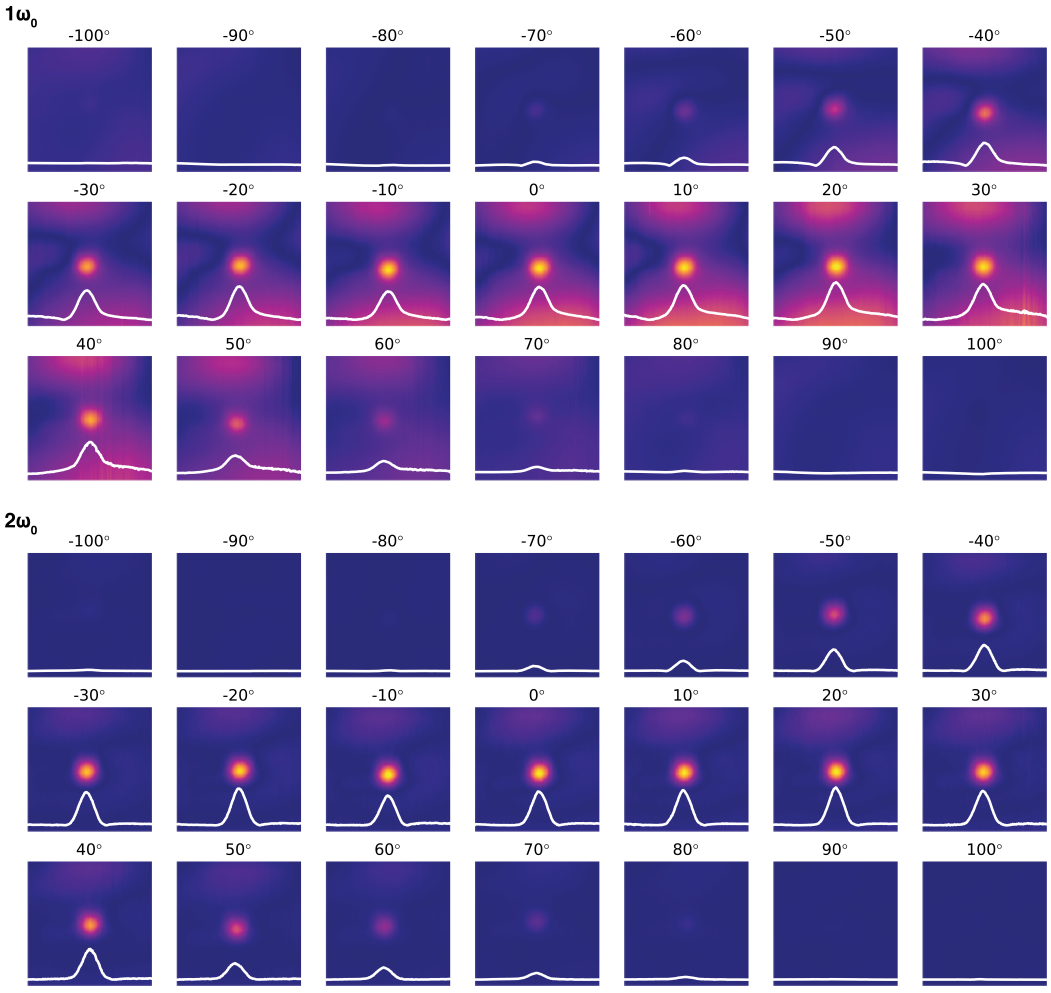
1ω0
-100°
-90°
-80°
-70°
-60°
-50°
-40°
-30°
-20°
-10°
0°
10°
20°
30°
40°
50°
60°
70°
80°
90°
100°
2ω0
-100°
-90°
-80°
-70°
-60°
-50°
-40°
-30°
-20°
-10°
0°
10°
20°
30°
40°
50°
60°
70°
80°
90°
100°

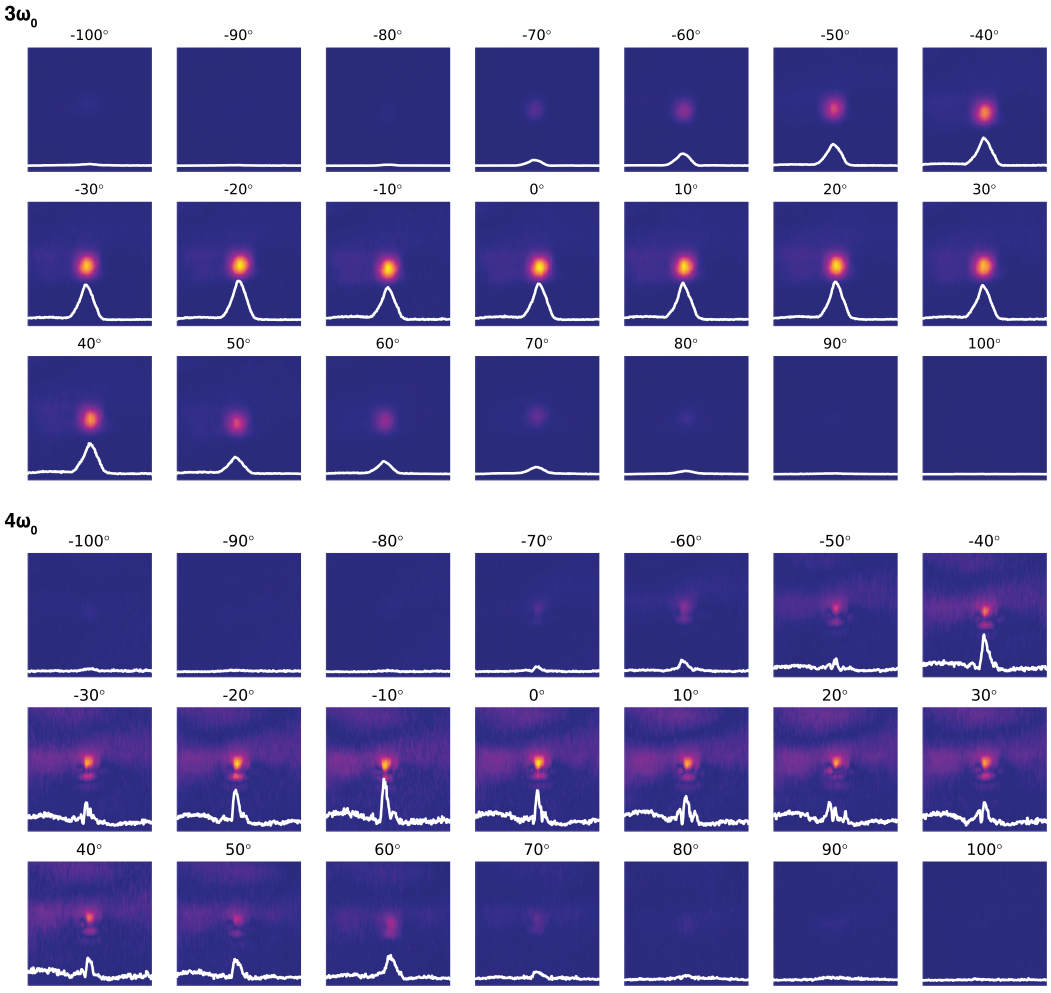
3ω0
-100°
-90°
-80°
-70°
-60°
-50°
-40°
-30°
-20°
-10°
0°
10°
20°
30°
40°
50°
60°
70°
80°
90°
100°
4ω0
-100°
-90°
-80°
-70°
-60°
-50°
-40°
-30°
-20°
-10°
0°
10°
20°
30°
40°
50°
60°
70°
80°
90°
100°

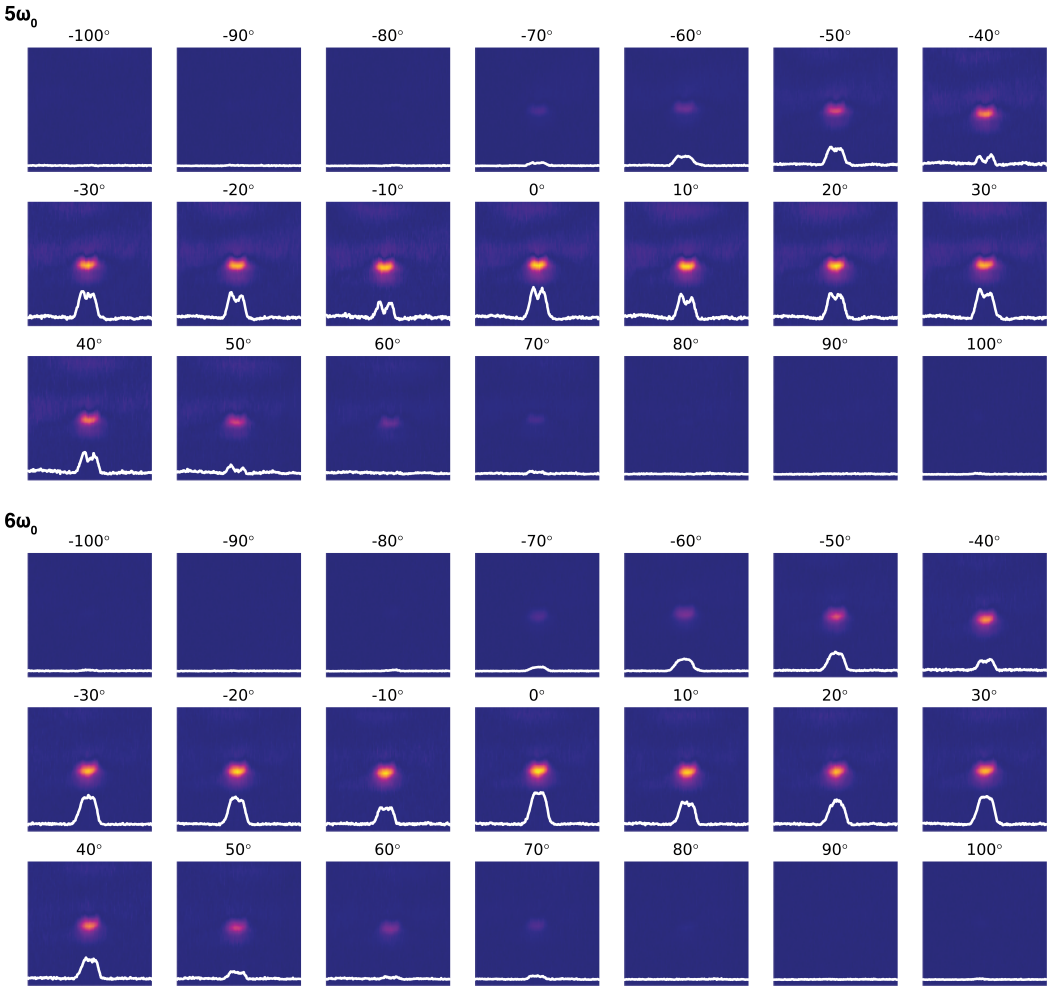
5ω0
-100°
-90°
-80°
-70°
-60°
-50°
-40°
-30°
-20°
-10°
0°
10°
20°
30°
40°
50°
60°
70°
80°
90°
100°
6ω0
-100°
-90°
-80°
-70°
-60°
-50°
-40°
-30°
-20°
-10°
0°
10°
20°
30°
40°
50°
60°
70°
80°
90°
100°

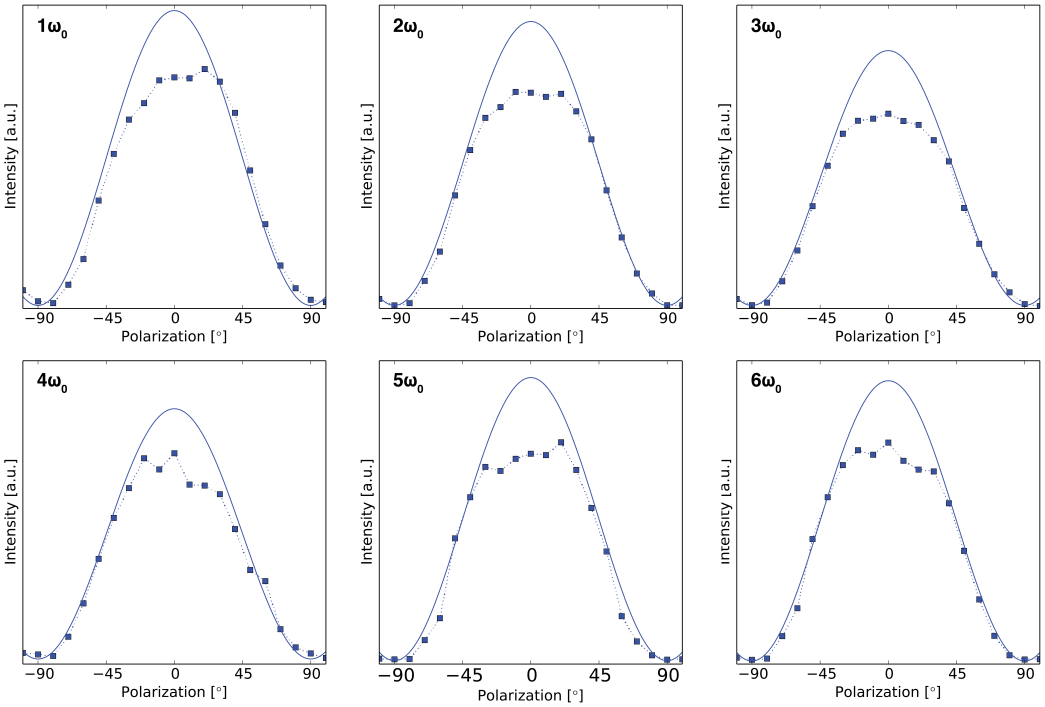

Figure B.20: **Maximum intensities of all 830 nm near-field maps in Figure B.19.** The data is plotted along with an expected intensity curve following a $cos^2(\theta)$ law.

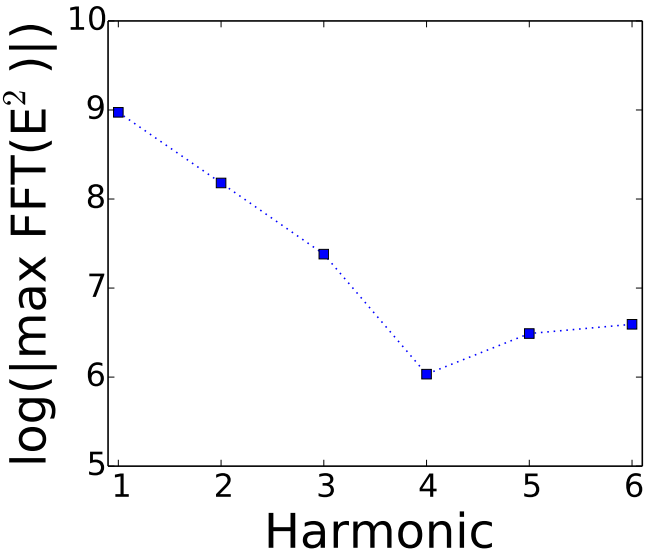

Figure B.21: **Maximum intensity vs. harmonic with 830 nm laser excitation.** At 0° polarization.

633 nm Laser Excitation

Figure B.22: **Complete harmonics for 633 nm illumination.** The full set of sSNOM data taken with 633 nm laser light with harmonics $1\omega_0$ to $6\omega_0$ and polarizations from $-100°$ to $+100°$.

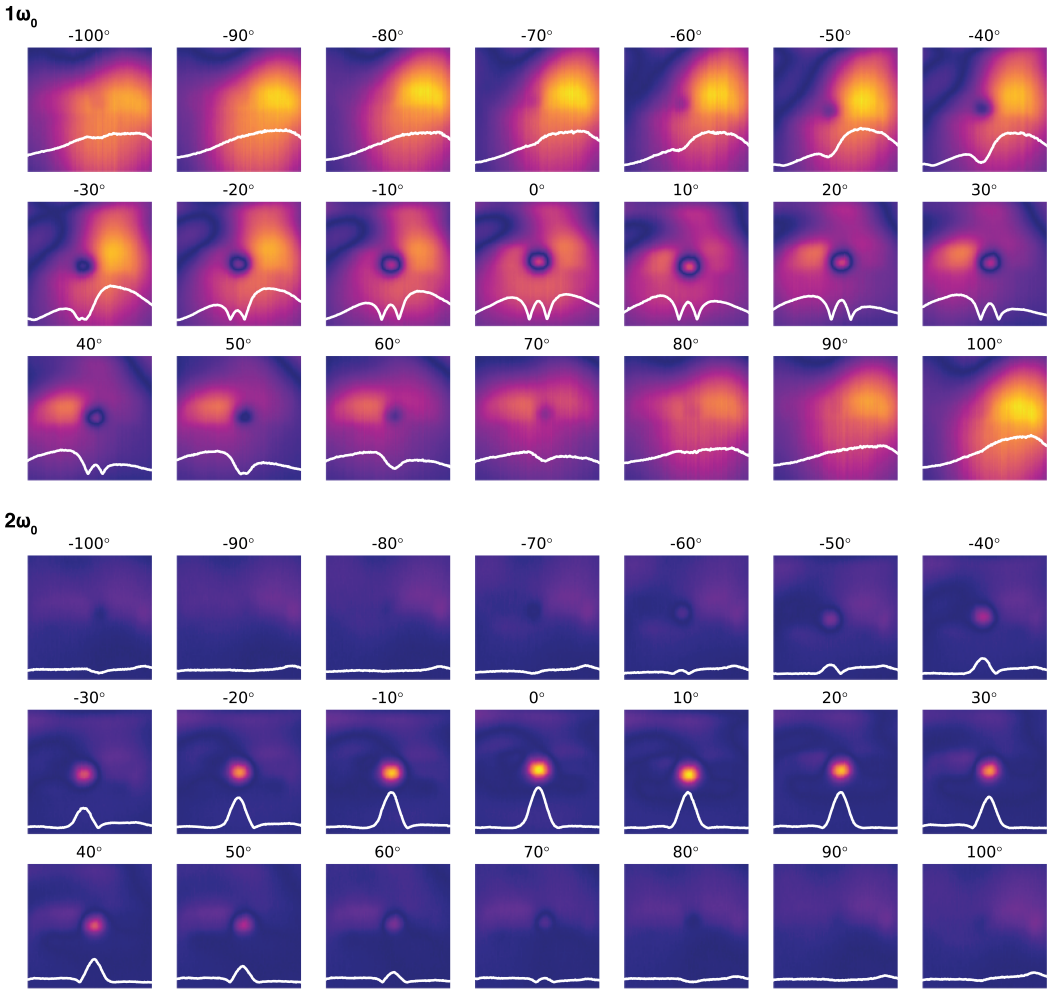
1ω0
-100°
-90°
-80°
-70°
-60°
-50°
-40°
-30°
-20°
-10°
0°
10°
20°
30°
40°
50°
60°
70°
80°
90°
100°
2ω0
-100°
-90°
-80°
-70°
-60°
-50°
-40°
-30°
-20°
-10°
0°
10°
20°
30°
40°
50°
60°
70°
80°
90°
100°

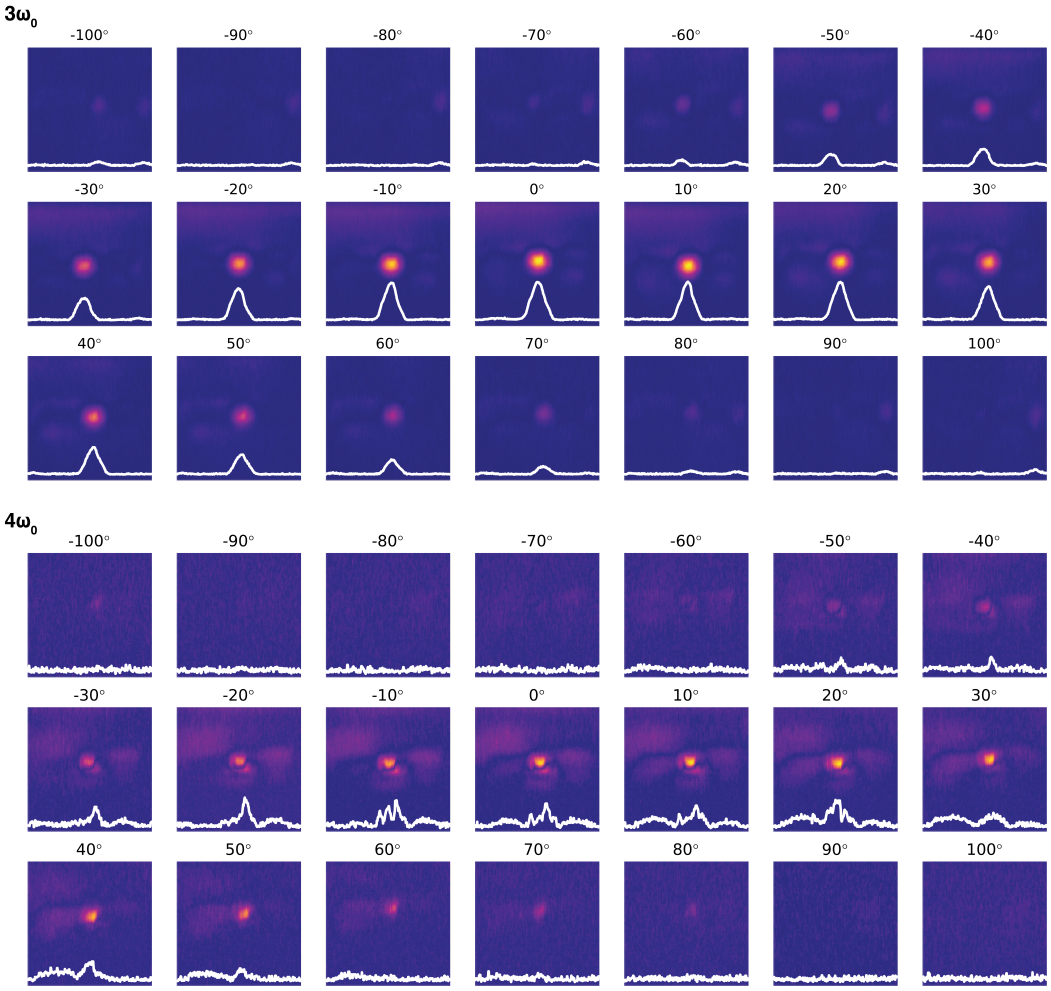
3ω0
-100°
-90°
-80°
-70°
-60°
-50°
-40°
-30°
-20°
-10°
0°
10°
20°
30°
40°
50°
60°
70°
80°
90°
100°
4ω0
-100°
-90°
-80°
-70°
-60°
-50°
-40°
-30°
-20°
-10°
0°
10°
20°
30°
40°
50°
60°
70°
80°
90°
100°

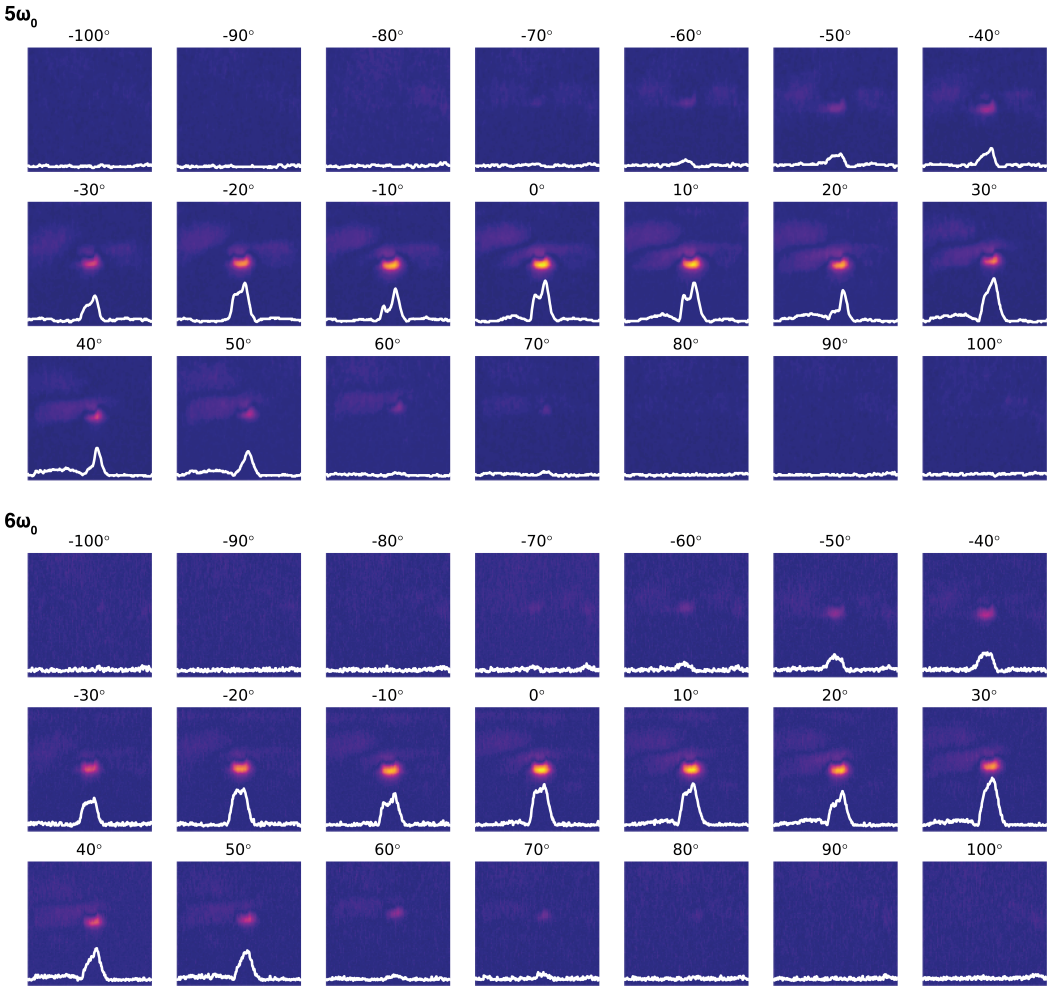
5ω0
-100°
-90°
-80°
-70°
-60°
-50°
-40°
-30°
-20°
-10°
0°
10°
20°
30°
40°
50°
60°
70°
80°
90°
100°
6ω0
-100°
-90°
-80°
-70°
-60°
-50°
-40°
-30°
-20°
-10°
0°
10°
20°
30°
40°
50°
60°
70°
80°
90°
100°

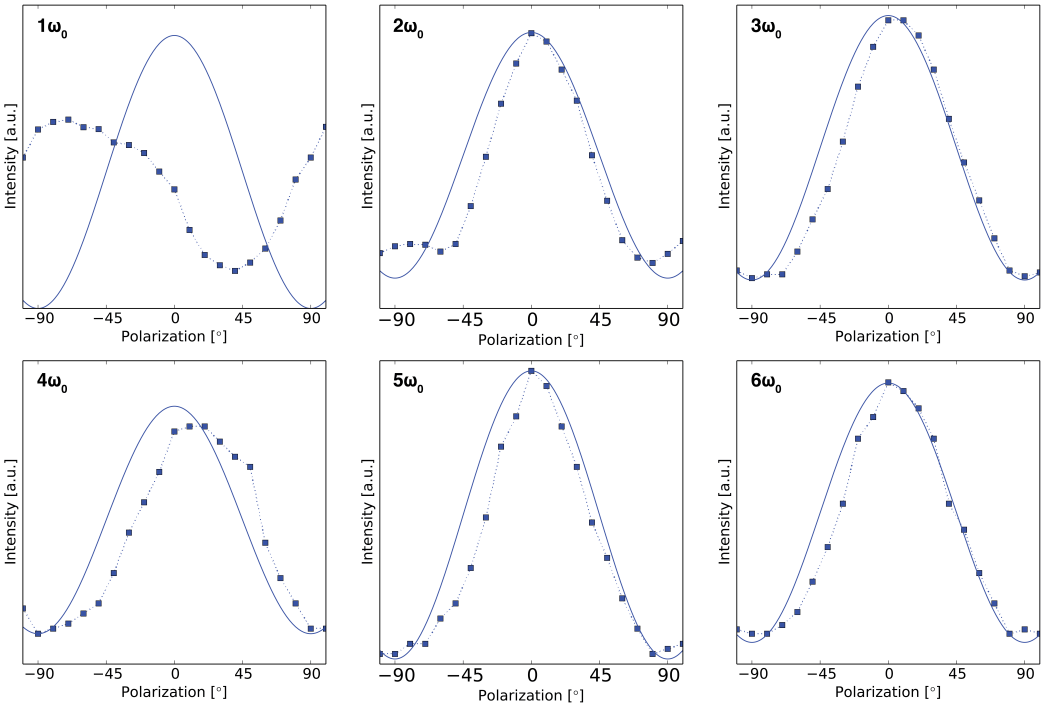

Figure B.23: **Maximum intensities of all 633 nm near-field maps in Figure B.22.** The data is plotted along with an expected intensity curve following a $cos^2(\theta)$ law.

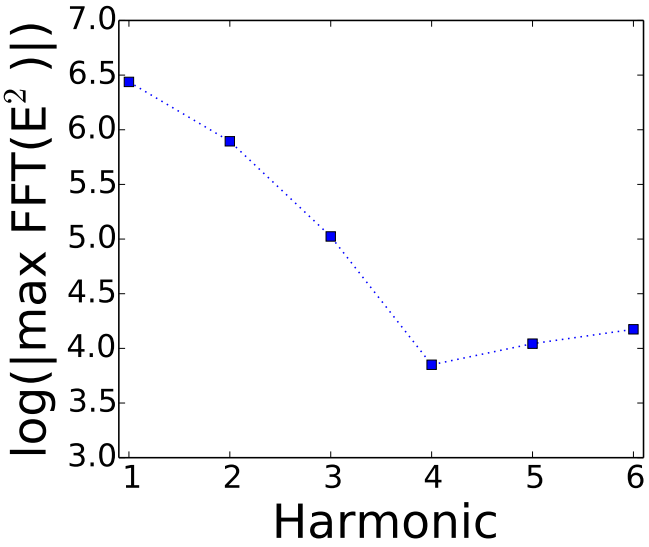

Figure B.24: **Maximum intensity vs. harmonic with 633 nm laser excitation.** At 0° polarization.

Appendix C

Common Acronyms

A table of common acronyms used in this dissertation and their meaning.

C.1 Acronyms

Table C.1: Acronyms

Acronym	Meaning
ABS	air-bearing surface
AES	Auger electron spectroscopy
AFM	atomic force microscopy
ALD	atomic layer deposition
CL	cathodoluminescence
CMOS	complement metal-oxide-semiconductor
DCA	distance of closest approach
FOM	figure of merit
FPP	four-point probe
HAMR	heat-assisted magnetic recording
HDD	hard disk drive
MSE	mean square error
PEALD	plasma-enhanced atomic layer deposition

Continued on next page

Table C.1 – continued from previous page

Acronym	Meaning
PS	polystyrene
SE	spectroscopic ellipsometry
SEM	scanning electron microscopy
SEM-CL	scanning electron microscopy cathodoluminescence
sSNOM	scattering scanning near-field optical microscopy
TDMAT	tetrakis(dimethylamino)titanium
TEM	transmission electron microscopy
VASE	variable angle spectroscopic ellipsometry